

Skoltech

Skolkovo Institute of Science and Technology

Proceedings of the Skoltech Energy PhD Seminar

2016/17

$S = -5k \cdot b$
 $5 = -k \cdot 5 \cdot b \Rightarrow S = -5k \cdot b$
 $1 = k \cdot 3 \cdot b \Rightarrow 1 = 3k \cdot b$

$ADLCB$
 $9y^2 - 54y - 161 = 0$
 $5 = -5k \cdot b$
 $\begin{cases} -5k + b = 5 \\ 3k + b = 1 \end{cases}$

$A(-5, 5)$
 $B(3, 1)$
 $D(2, 5)$
 $ADLCB$
 $1 = 3k \cdot b$

$\alpha(x + \frac{b}{2a})^2 - c - \frac{b^2}{4a}$
 $\bar{n} = \{-4, 11, -3\}$
 $d = \sqrt{(x_2 - x_1)^2 + (y_2 - y_1)^2}$
 $\alpha x^2 - \beta x + c = 0$
 $l > 1$ Ex. $c = 6$
 $a = 3$

$16x^2 - 9y^2 - 64x - 54y - 161 = 0$
 $\frac{4}{m-n} \left(\frac{1}{n} - \frac{1}{m} \right) \cdot \frac{(m-n)^2}{2mn}; \frac{2}{2} = 1$

$16(x-2)^2 - 9(y-3)^2 = 144$
 $\frac{(x-2)^2}{9} - \frac{(y-3)^2}{16} = 1$
 $b = x = 0$

Skoltech

Skolkovo Institute of Science and Technology



Skolkovo Institute of Science and Technology
 Skolkovo Innovation Center, Building 3
www.skoltech.ru/en

$\alpha(x + \frac{b}{2a})^2 - c - \frac{b^2}{4a}$
 $\bar{I} = (m, n, p)$
 $\frac{4}{1} \cdot \frac{1}{mn} = \frac{4}{mn}$
 $\frac{2(n-m)^2}{m^2 n^2}$
 $A(-5, 5) \Rightarrow 5 =$
 $B(3, 1) \Rightarrow 1 =$

$V_1 + V_2 + V_3 + V_5 = V_a - r_1 \bar{I}$
 $+ V_1 + E_1 + V_2 - r_2 \bar{I} +$
 $+ V_3 - E_2$
 $\bar{I}(r_1 + r_2) = V_a - V_5 + E_1$

$\bar{I} = \frac{V_a - V_5 + E_1 - E_2}{r_1 + r_2}$

V_1, V_2, V_3
 $I = \frac{V}{I}; r = \frac{V}{I}$
 $\bar{I}_1 = \frac{V_3 - V_1 + E}{r_1} = g_1 (V_3 - V_1 + E_1)$
 $\bar{I}_2 = g_2 (V_1 - V_3 + E_2); g_2 = \frac{1}{r_2}$
 $\bar{I}_3 = g_3 (V_1 - V_2 - E_3); g_3 = \frac{1}{r_3}$

$E = V_1 - V_2$
 $V_1 \gg V_2$
 $V_3 = V_2$
 $E = V_1 - V_2$
 $V_2 = V_1 + E$
 $V_3 = V_2$

$E = V_1 - V_2$
 $V_1 \gg V_2$
 $V_3 = V_2$

$\bar{I}_1 = \frac{V_3 - V_1 + E}{r_1}$
 $\bar{I}_2 = g_2 (V_1 - V_3 + E_2)$
 $\bar{I}_3 = g_3 (V_1 - V_2 - E_3)$

$21 \cdot i = \rho \cdot U$



Skolkovo Institute of Science and Technology

Skoltech PhD Energy Seminar Proceedings 2016/2017

The Proceedings is a collection of the original research papers written by the participants of the first Skoltech PhD Energy Seminar in the 2016–2017 academic year.

The Skoltech PhD Energy Seminar unites students enrolled on Skoltech PhD Programs associated with the Centers of Electrochemical Energy Storage, Energy Systems, Hydrocarbon Recovery, and Photonics & Quantum Materials.

The Seminar promotes the exchange of knowledge, methodologies, and research questions across the fundamentally different scientific areas in accordance with the Skoltech vision of multidisciplinary research and education oriented to innovation. The main goal of the Seminar is to create and maintain interdisciplinary links between students doing research related to energy resources, generation, storage and distribution, as well as methods, models, devices and materials for efficient energy use.

Besides its immediate research-oriented goal, the pragmatic aim of the Seminar is to engage PhD students in professional academic communication activities based on the principles of ethics and peer review. During the Seminar, students were required to present the results of their research, write an article for the Proceedings according to a template, and peer review two papers submitted by the Seminar participants.

In preparation for the Proceedings, each paper was anonymously reviewed by a peer working in the same field and the other one with a different background and interests. In addition, all articles were checked by a language instructor. The final versions had to incorporate comments from the referees and editors to be accepted for the Proceedings. They are presented here as submitted.

The first Skoltech PhD Energy Seminar was useful yet challenging for both the organizers and participants. In future, the timeframe and the number of participants of the Seminar may have to be optimized to increase the overall efficiency of the project.

We appreciate the efforts and devotion of all the Seminar attendees and the contributions of their supervisors. Our special thanks to Dr. Alexander Patrushev who assisted the Seminar in 2016.

We are also grateful to the production team, Mrs. Irina Velichko, Ms. Elena Barinova and Mr. Alexander Zolotarev for preparing this document for publication.

Prof. Alexei Buchachenko (Seminar instructor)

Dr. Anna Sharova

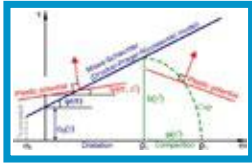
Prof. Elizaveta Tikhomirova

CONTENTS

RESEARCH ARTICLES:

A.I. Akhtyamova, Yu.P. Stefanov, A.V. Myasnikov

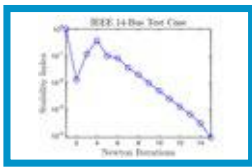
VALIDATION OF COMPOUND LIMITING SURFACE MODEL USING LOAD AND UNLOAD EXPERIMENTS 8



- Compound limiting surface model permits a description of semi and high-porous rocks behavior under the load
- Deformation may be accompanied by compaction or dilatancy in a geological environment depending on the pressure
- To determine the minimum set of parameters, two experiments on triaxial loading must be done at different confining pressures
- Compound limiting surface model takes into account the most important rock behavior characteristics as a result of loading and reloading stages

Mazhar Ali

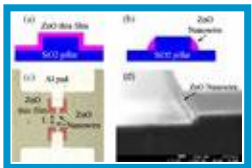
LOADABILITY LIMIT IN POWER SYSTEM WITH REACTIVE POWER FEASIBILITY CONSTRAINTS13



- The algorithm converges in small number of iterations
- The algorithm converges monotonically
- The computational overhead is small comparing to other approaches
- Opens the possibility of including more technical constraints

A.G. Askarova, K. Kalna

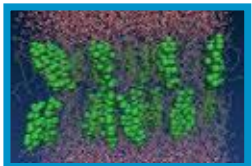
PHYSICAL MODELING OF ZNO NANOWIRE FIELD-EFFECT TRANSISTORS19



- The structure of ZnO nanowire FET that is grown on the top of a p-type Si substrate was reproduced using Silvaco software
- The obtained I_D-V_D and I_D-V_G characteristics of the semiconductor device were compared with experimental data. The results are satisfactory
- For 10- μm channel length, there is a presence of a large external contact resistance
- The threshold voltages for all channel lengths are obtained, that are close to the experimental V_T , despite the fact, that the surface charge is taken into account in the simulation

Lyudmila Khakimova, Pavel Buslaev, Ivan Gushchin, Artem Myasnikov

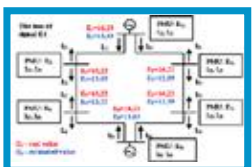
THE INFLUENCE OF EXTERNAL FACTORS ON THE DYNAMICS OF A LIPID MOLECULE IN THE COMPUTER MODELING27



- Homogeneous and heterogeneous bilayers were prepared
- A simulation of ~ 1000 ns was performed
- The method of analyzing the conformational dynamics of a lipid molecule was developed
- The method of determining the orientation of the lipid in relation to the normal to bilayer was developed
- The effect of temperature and cholesterol in the membrane on lipid dynamics was determined

Irina Lukicheva, Alexander Kulikov, Alexander Ustinov

INFLUENCE OF COMMUNICATION SIGNAL LOSS ON THE RESULTS OF POWER SYSTEM STATE ESTIMATOR34



- Communication channel breakdown may significantly spoil the results of State Estimation
- Bad Data Detection may not help to improve the results of State Estimation in case of signal loss
- Pre-use non-linear techniques may improve the results of State Estimator

Aliya Z. Mukhametdinova, Alexey N. Cheremisin

SURFACE MODIFICATION OF PROPPANT FOR ENHANCED OIL RECOVERY38



- Proppants used in hydraulic fracturing were coated with different surface modification agents
- Effect of hydrophobization and hydrophilization was successfully achieved, durability of coating was tested
- Coated proppants can be used for increasing the oil-relative or water-relative phase permeability in the multiphase flow
- Set of laboratory tests on proppant aging, wettability and permeability was conducted
- Future research directions include further coated proppant testing at lab and industrial scale

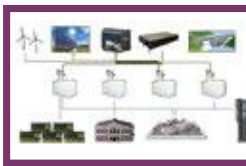
Aleksandra Sveshnikova, Gioele Di Marcoberardino, Alexander Ustinov, Aldo Bischì
INVESTIGATION OF FLOODING/DROUGHT PHENOMENA
IN 1KW PROTON EXCHANGE MEMBRANE FUEL CELL.....44



- PEM Fuel Cell system was improved by the development of air humidification system
- Humidification system works in such way that it achieves 100% RH at any operating temperature
- However, humidification temperature greatly influences absolute humidity and thus, overall FC performance
- This research is ongoing and better results and improvements of the system construction will be achieved soon

SMALL REVIEWS:

Vasily G. Chirkin
OVERVIEW OF MICROGRID CONTROL.....53



- Implementation of renewable energy sources causes difficulties for control of power systems
- The microgrid concept is intended to overcome these challenges
- An overview of microgrid control techniques is represented

A.V. Gabova, E.Y. Popov, E.M. Chekhonin, R.A. Romushkevich, Y.A. Popov
THERMAL CORE LOGGING TECHNIQUE FOR BAZHENOV FORMATION CHARACTERIZATION.....58



- New experimental technique was used for reservoir thermal property measurements
- Unique experimental data were obtained for a wide set of rock thermal properties for the Bazhenov formation
- Relationships between thermal and other physical properties of rocks were established
- High spatial resolution of thermal core profiling improves the quality of thermal properties

Evgenia P. Gilshteyn, Albert G. Nasibulin
NOVEL WEARABLE CARDIAC RHYTHM MANAGEMENT SYSTEMS64



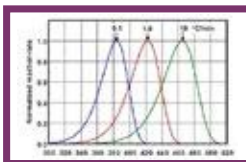
- Electrocardiography is the most promising application of wearable sensors
- Wearable sensors have diagnostic, as well as monitoring applications
- Wearable computing systems can be attached to cloth or a human body
- Still, it is a long way to scaling up of this technology

Anastasia Ivanova
REVIEW OF ALKALINE - SURFACTANT - POLYMER (ASP) FLOODING: PAST AND PRESENT70



- Typical scheme of alkaline/surfactant/polymer flooding
- Chemicals are used to recover additional oil
- Usually preflush is just water to recover oil, which is not trapped into porous media

Nikolai Mitiurev
REVIEW OF KEROGEN THERMAL DESTRUCTION KINETICS AND DECONVOLUTION TECHNIQUE
APPLICATION76



- Typical kerogen thermal destruction kinetic curves at constant heating rate
- With increasing of heating rate, curve moves to the right, in the higher temperature area
- All reaction rates are normalized to one to simplify calculations

A. Naumov

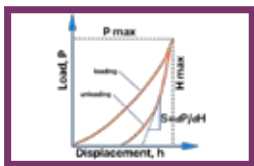
PREVENTION OF FOLDING PROCESSES IN CONJUGATED POLYMER CHAINS: TECHNIQUES AND STRUCTURES 82



- Five approaches to polymer chain folding prevention are considered
- Special structures and isolation surfactants designed to keep rod-like shape of a polymer backbone chain are reviewed

Evgeny Shilov

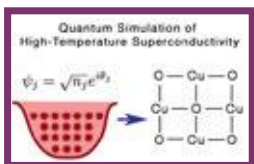
STATUS OF NANOINDENTATION TESTING IN SHALES 86



- Status of nanoindentation testing (NIT) technique in shales
- Existing results of nanoindentation experiments on core samples of shales
- Problems of nanoindentation technique
- Future plans of the research connected to NIT

Andrei E. Tarkhov

TOWARDS QUANTUM SIMULATION OF HIGH-TEMPERATURE SUPERCONDUCTIVITY WITH ULTRACOLD ATOMS IN OPTICAL LATTICES 92



- Ultracold atoms in optical lattices (UCA) is a promising quantum simulator
- High-temperature superconductivity (HTSC) is challenging for classical computing
- Quantum phase transitions were modeled with quantum simulators on UCA
- Fermionic transport was simulated with quantum simulators on UCA
- Practical recipes for searching new HTSC are yet to be proposed

FOCUS:

A. Churkin

ANALYSIS OF INTERDEPENDENCIES BETWEEN GAS AND ELECTRIC POWER SYSTEMS FOR OPTIMAL DISPATCHING AND RELIABILITY ASSESSMENT 100



- Global optimization should be performed for a real case in order to estimate social welfare increase
- Methodology of total benefits distribution should be suggested
- Application of global dispatching and optimization needs significant technical and regulatory development
- Contingency analysis can be also performed for the coupled systems

Maksim D. Glagolev

MODERN TRENDS IN EUROPEAN DISTRICT HEATING 105



- District Heating is the important part of energy systems
- 4th generation of District Heating will bring significant changes to existing systems
- DH will be the part of integrated energy infrastructures coupling power and gas sectors
- Smart District Heating systems will include renewables, thermal energy storages, smart meters, smart management.

$$d = \sqrt{(x_2 - x_1)^2 + (y_2 - y_1)^2}$$

$$l > 1$$

$$\text{Ex. } c = 6$$

$$a = 3$$

$$ax^2 + bx + c = 0$$

$$16x^2 - 9y^2 - 64x - 54y - 161 = 0$$

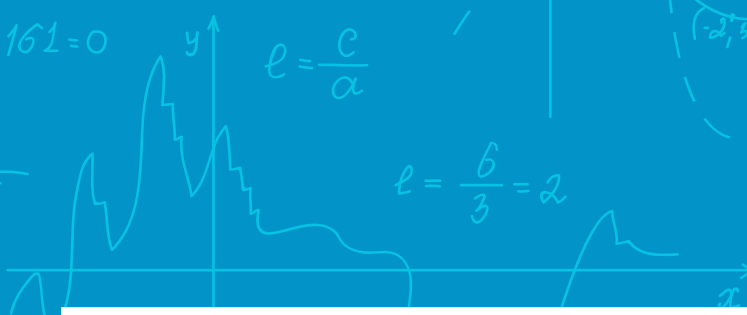
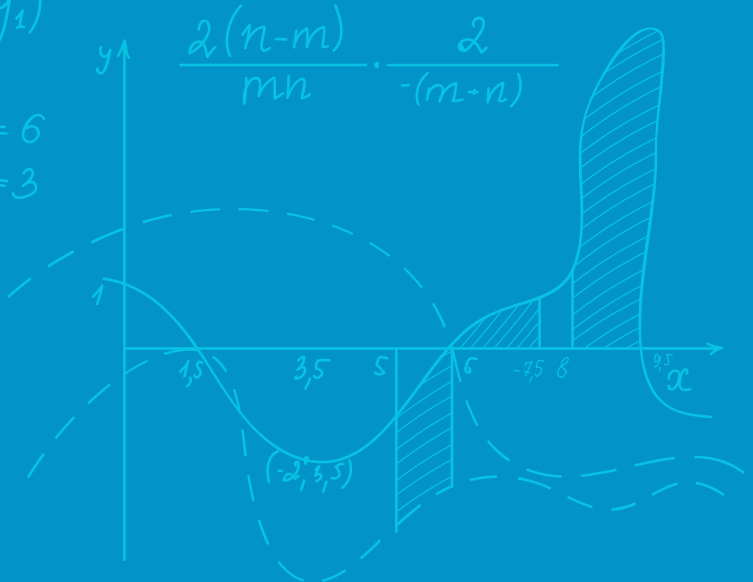
$$\frac{4}{1-n} \left(\frac{1}{n} - \frac{1}{m} \right) \cdot \frac{(m-n)^2}{2mn}; \quad \frac{2}{2} = 1$$

$$9y^2 - 54y - 161 = 0$$

$$e = \frac{c}{a}$$

$$e = \frac{6}{3} = 2$$

$$\frac{m^2 n^2}{m^2 n^2} = 1 \cdot 2(n^2 + m^2) = \frac{2(n^2 + m^2)}{m^2 n^2}$$



Research Articles

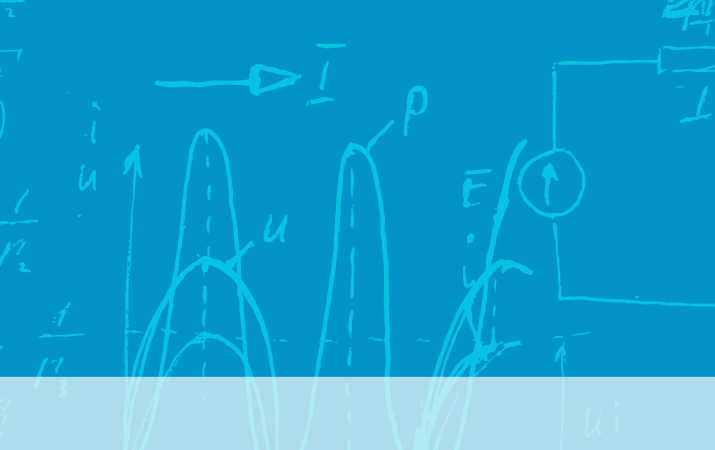


$$V_1 + V_2 + V_3 + V_4 + V_5 + V_6 + V_7 + V_8 + V_9 + V_{10} + V_{11} + V_{12} + V_{13} + V_{14} + V_{15} + V_{16} + V_{17} + V_{18} + V_{19} + V_{20} + V_{21} + V_{22} + V_{23} + V_{24} + V_{25} + V_{26} + V_{27} + V_{28} + V_{29} + V_{30} + V_{31} + V_{32} + V_{33} + V_{34} + V_{35} + V_{36} + V_{37} + V_{38} + V_{39} + V_{40} + V_{41} + V_{42} + V_{43} + V_{44} + V_{45} + V_{46} + V_{47} + V_{48} + V_{49} + V_{50} + V_{51} + V_{52} + V_{53} + V_{54} + V_{55} + V_{56} + V_{57} + V_{58} + V_{59} + V_{60} + V_{61} + V_{62} + V_{63} + V_{64} + V_{65} + V_{66} + V_{67} + V_{68} + V_{69} + V_{70} + V_{71} + V_{72} + V_{73} + V_{74} + V_{75} + V_{76} + V_{77} + V_{78} + V_{79} + V_{80} + V_{81} + V_{82} + V_{83} + V_{84} + V_{85} + V_{86} + V_{87} + V_{88} + V_{89} + V_{90} + V_{91} + V_{92} + V_{93} + V_{94} + V_{95} + V_{96} + V_{97} + V_{98} + V_{99} + V_{100}$$

$$I = \frac{V_a - V_b + E_1 - E_2}{r_1 + r_2}$$

$$I = g_1 (V_3 - V_1 + E_1)$$
$$I = g_2 (V_1 - V_3 + E_2)$$
$$I = g_3 (V_1 - V_2 - E_2)$$

$$I = g_4 (V_1 - V_2 - E_2)$$



Validation of Compound Limiting Surface Model Using Load and Unload Experiments

A.I. Akhtyamova*, Yu.P. Stefanov, A.V. Myasnikov

Abstract - Based on the experimental work [7] a number of numerical computations are provided. The calculation parameters are determined in accordance with the presented algorithm of elastic-plastic model [5] initialization and then compared with experimental results. Non-linear initial sections of the stress-strain diagram are considered, and the importance of these sections is taken into account in the multistage load modeling.

Index Terms - algorithm analysis, compaction, core elevation, dilatancy, geomechanics, hysteresis curve, multistage loading, nonlinear section, triaxial compression.

I. NOMENCLATURE

Application of compound limiting surface model required determination of the following parameters:

E	elastic modulus (Pa)
K	compression modulus (Pa)
G	shear modulus (Pa)
ν	Poisson ratio
α	angle of internal friction
Y	cohesion
	(α and Y_0 strength parameters, determining limiting surface when $\sigma > 0$)
h	hardening coefficient
γ^*	critical deformation, after which degradation of material is prevailing
γ^0	plastic deformation of total failure
Λ	coefficient of dilatancy, determining plastic potential and corresponding direction of incremental vector of plastic deformation
σ_t	tear strength by uniaxial tension (Pa).
ϵ_1	axial strain
σ_1	axial stress
P	hydrostatic pressure
ϵ_r	radial deformation
σ_c	confining pressure
τ	shear stresses intensity
θ	volumetric strain

II. INTRODUCTION

Numerical model development, stress-strain analysis and explaining the processes, which occur in rocks, require data on rock properties under formation conditions. Experimental data on rock properties obtained during core tests may differ from data in situ conditions. Core elevation to the surface can cause a state of irreversible strain by stress relaxation after in situ high-pressure conditions and resulting in inelastic deformation [1].

A. I. Akhtyamova is with the Center of Hydrocarbon Recovery, Skolkovo Institute of Science and Technology, Skolkovo Innovation Center, Building 3, Moscow 143026, Russia [e-mail: alina.akhtyamova@skoltech.ru].

Yu. P. Stefanov is with the Laboratory of Deep Seismic Studies and Regional Seismicity, Trofimuk Institute of Petroleum Geology and Geophysics SB RAS (IPGG SB RAS), Koptug ave. 3, Novosibirsk 630090, Russia [e-mail: yu_st@mail.ru].

A. V. Myasnikov is with the Center of Hydrocarbon Recovery, Skolkovo Institute of Science and Technology, Skolkovo Innovation Center, Building 3, Moscow 143026, Russia [e-mail: A.Myasnikov@skoltech.ru].

These effects are eliminated by core triaxial compression tests. Specimen resides in such compression conditions until linear dimensional stabilization and initial state restitution (healing of induced breaks) is reached [2]. To investigate the processes occurring inside the rock during its elevation and after triaxial loading, specimens undergo multistage and cyclic loading. Stress strain dependencies take on a loop form in such tests (Fig. 1). This loop is named a "hysteresis curve" (it is worth noting that hysteresis curves occur when stress comes up to the level wherein plastic deformations appears).

At the same time, experiments show nonlinear section existence (it may be caused by specifics of equipment or rock conditioning process) both at the outset of loading (stage I at the graph) and unloading (stage II at the graph).

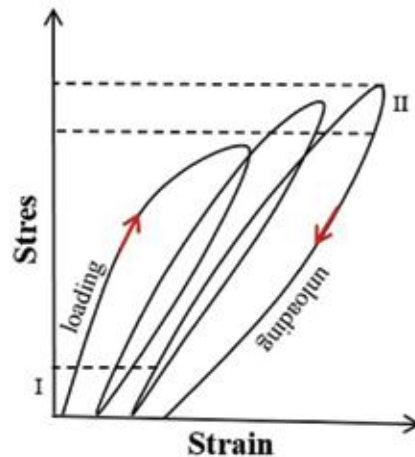


Fig. 1. Stress-strain dependencies multistage loading scheme

Existence of corresponding sections plays an important role in stress-strain state estimation in the processes of deformation localization and material destruction.

However, simulation results based on models, matching with specimen behavior under loading conditions, often are in bad agreement with experimental data after the reloading stage. Specifically, they exclude the nonlinear sections accounting. Therefore, it is necessary to construct an adequate model, which would consider all the key insights of multistage experiments.

III. MODEL PARAMETERS DETERMINATION AND MODEL INITIALIZATION

For the deformation processes, occurring inside the geological environment under loading conditions, description and its simulation it is necessary to define the problem correctly and choose the constitutive relations. In these ratios, it is necessary to consider the behavior patterns of definite structure in conditions under consideration.

To describe the deformation processes beyond the elastic limit, we used the relations of modified Drucker-Prager-Nikolaevsky model with the non-associated flow rule [3, 4].

Due to this model limiting surface describes by the following formula

$$f = \tau - \alpha\sigma - Y \quad (1)$$

and plastic potential by

$$g = \tau - \Lambda\sigma \quad (2)$$

The complexity of geomaterials behavior description beyond the elastic limit is that the surface limiting stress state, where development of plastic deformation begins, is not fixed; it changes during the deformation. Also, parameters describing behavior of the geological environment beyond the elastic limit, become functions of the cumulative strain and pressure [5].

The laws of variations of the limiting surface are formulated in [6].

Constructing limiting surface and analyzing rock behavior beyond the elastic limit in terms of using model, it is convenient to present obtained data in the invariant values. Stresses can be performed in terms of shear stresses intensity τ and pressure σ ; deformations in terms of intensity of shear deformation γ and volumetric deformation ϵ .

Model initialization algorithm (Fig. 2) starts from axial stress versus axial deformation $\sigma_1(\varepsilon_1)$ graph plotting according to experimental data. Further, Young's modulus is determined by the straight-line portion selection on this graph.

Stress and strain data is recalculated from the core experiments data to the $P(\varepsilon)$ and $\tau(\gamma)$ coordinates according to the next formulas:

$$\sigma = P = \frac{(\sigma_1 + 2\sigma_c)}{3} \quad (3)$$

$$\theta = \varepsilon = \varepsilon_1 + 2\varepsilon_r \quad (4)$$

$$\tau = \frac{|\sigma_1 - \sigma_c|}{\sqrt{3}} \quad (5)$$

$$\gamma = \frac{2|\varepsilon_1 - \varepsilon_r|}{\sqrt{3}} \quad (6)$$

After that, $P(\varepsilon)$ graph is constructed. Bulk modulus is also determined by a straight-line portion selection. Elastic strain interval is highlighted in order to calculate volumetric plastic deformation as follows:

$$\varepsilon^p = \varepsilon - \varepsilon^e \quad (7)$$

Critical strain γ^* is determined in the same figure at the point in which the curve is turned inversely (dilatancy of the material is observed). Elastic strain passes into plastic strain in the P^* point. Sample crushing transitional point is expressed as P^0 .

Dependency graph $\tau(\gamma)$ is processed likewise: shear modulus is determined by a straight-line portion selection; elastic strain interval is highlighted in order to calculate intensity of plastic shear deformation:

$$\gamma^p = \gamma - \gamma^e \quad (8)$$

Elastic strain passes into plastic strain in the τ^* . Sample crushing transitional point is expressed as τ^0 .

It is apparent from the equation of limiting surface, that to construct this surface it is necessary to have at least two points of measurements under two different confining pressures (preferable to have the last point of measurement corresponding to the uniaxial strain condition when $\sigma^* = \sigma_1/3$ that may be determined in correspondence with recommended guideline/ requirements/ certificate of rock strength design methods).

Cohesion and angle of internal friction is calculated by substituting elastic P^* and τ^* , and strength P^0 and τ^0 limits into the system of equations for the limiting surfaces.

Dilatancy coefficient is defined by the experimental data as a ratio of increment of shear plastic deformation $\Delta\varepsilon^p$ to the increment of volumetric plastic deformation $\Delta\gamma^p$ is:

$$\Lambda = \frac{\Delta\varepsilon^p}{\Delta\gamma^p} \quad (9)$$

Hardening coefficient is equal to

$$h = Y^* / Y^0 \quad (10)$$

Dependency graph $P(\tau)$ may be constructed using the known parameters with the obtained limiting surfaces and plastic potential [5].

IV. OBTAINED RESULTS AND EXPECTATIONS

On the basis of work [7], the numerical calculations on granite samples multistage loading were completed. The test was done under triaxial loading conditions where confining pressure value was equal to 50 and 200 MPa. The sample was gradually loaded, at each stage of loading the value of deformation was fixed. Granite unloading process proceeded in a similar manner. The calculation of the elastic moduli was carried out according to the above mentioned algorithm. Initial and finite limiting surfaces were constructed after the post-yield initial point and maximum stress values determination.

Then cohesion and internal friction coefficient was defined. Sample loading numerical calculations was performed using the obtained parameters, which was then compared with the experiment results (Fig. 3). The model parameters on loading stage were varied within certain limits to obtain the best approximation to the experimental data.

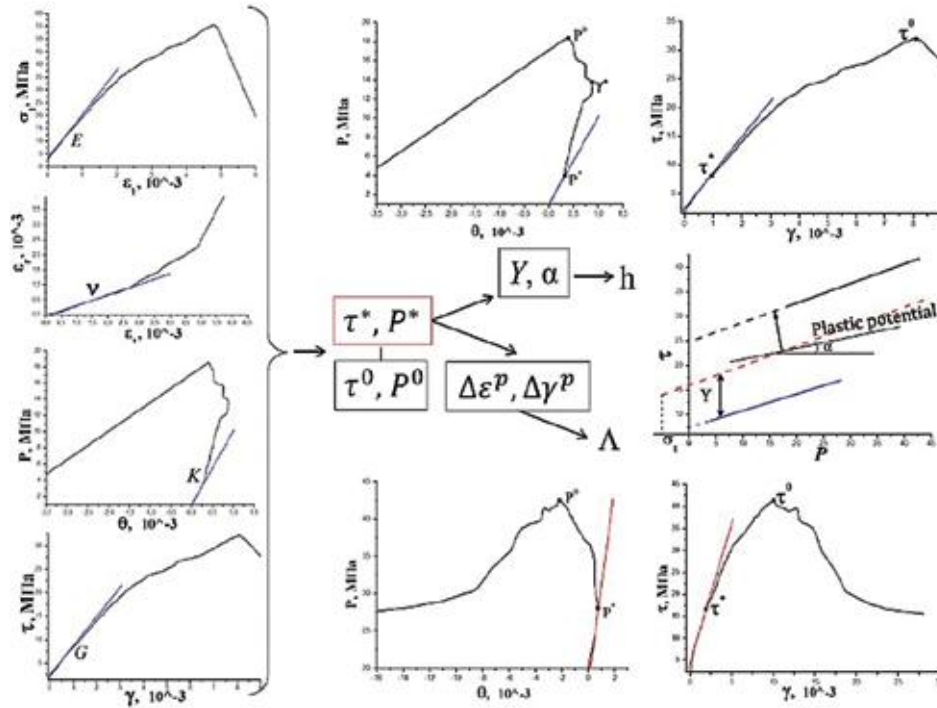


Fig. 2. Model initialization algorithm scheme. $E, K, G, \nu, P^*, \tau^*, P^0$ and τ^0 are data from the graphs. Other parameters are computational data

In obtaining good correspondence between the loading diagrams for one set of parameters, there was some discrepancy for other parameters.

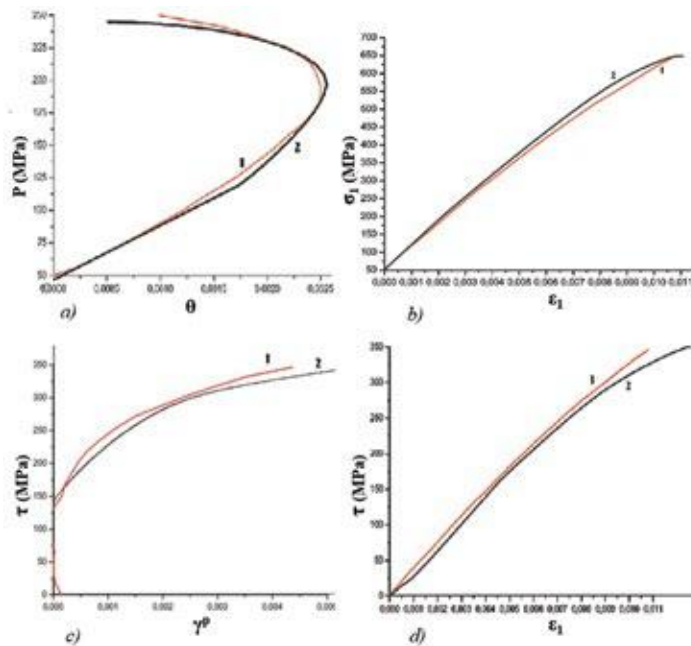


Fig. 3. Stress-strain dependency diagrams: a) hydrostatic pressure versus volumetric strain; b) axial stress versus axial strain; c) shear stress intensity versus plastic shear deformation; d) shear stress intensity versus axial strain. The «1» curves corresponds to experiment results, the «2» corresponds to simulated results

The discrepancy between the results of calculations and the experimental data is due to deformation conditions difference (loading paths of cylindrical samples in the experiment and under plane deformation conditions is differ) [8].

However, a set of parameters with positive similarities in loading curves behavior were obtained.

On the unloading stage, the sample retains macroscopic continuity. However, it is obvious that it has already undergone irreversible deformations, because of voids closure (branches of microcracks) formed during loading process after stresses relaxation. Such a phenomenon is possible within the framework of a quasilinear unloading section in the stress-strain diagram (Fig. 1). The compatibility of such section can aid the deformation processes localization and destruction development or deceleration. The quasilinear initial unloading section may be described using the maximum values of shear stress and volumetric strain.

V. CONCLUSIONS

It is necessary to take into account the difference in the research of model and real objects conditions as well as loading paths. Loading diagrams, resulting from two-dimensional modeling, have a behavior similar to the experimental one; differences occur due to the loading conditions.

Two-dimensional model verification requires the formulation of appropriate experiments. Setting of corresponding experiments is necessary for the two-dimensional model verification.

The nonlinearities observed at the initial sections of loading and unloading graphs can play an important role in the rock stress-strain state evaluation and it's geological structure study.

Expanded description of processes occurring in rock under multistage loading requires a proper model development and verification.

VI. REFERENCES

- [1] A. N. Stavrogin, B. G. Tarasov, "Experimental physics and rock mechanics," St. Petersburg, Russia, 2001.
- [2] Soils. Strength characteristics and deformability determinations laboratory methods, GOST 12248-2010.
- [3] Drucker D. C., W. Prager. Soil mechanics and plastic analysis for limit design. Quarterly of Applied Mathematics. 2 (1952) 157-165.
- [4] Nikolaevskii V.N. Constitutive equations for plastic deformation of granular media. Journal of Applied Mathematics and Mechanics. 6 (1971) 1070-1082.
- [5] Stefanov Yu.P., Numerical modeling of deformation and failure of sandstone specimens // Journal of Mining Science. 2008, 44(1), pp. 64-72.
- [6] Stefanov Yu.P., Chertov M.A., Aidagulov G.R., Myasnikov A.V. Dynamics of Inelastic Deformation of Porous Rocks and Formation of Localized Compaction Zones Studied by Numerical Modeling // Journal of the Mechanics and Physics of Solids. 2011, 59, pp. 2323-2340.
- [7] Zoback M.D., J.D. Byerlee. The effect of cyclic differential stress on dilatancy in Westerly granite under uniaxial and triaxial conditions // Journal of Geophysical Research. 1975, 80(11), pp. 1526-1530.
- [8] A. I. Akhtyamova, Yu.P. Stefanov, V. A. Zaitzev, "Experimental data analysis and granite sample elastoplastic deformation numerical modeling" in International Scientific School for Young Scientists, Moscow, IPMech RAS, 2015, pp. 31-33.

Loadability Limit in Power System with Reactive Power Feasibility Constraints

Mazhar Ali

Abstract - Stable and secure operation of power systems requires identification of solutions that are at the feasibility boundary with additional technical and loadability constraints. This paper considers Power Flow equations extended by a system of algebraic equations which describe the inequality constraints imposing reactive power capability limits on voltage controlled buses (PV). The methodology presented in this paper allows to find a feasible solution with proper accounting for the reactive power capability limits and identification of switches from the PV to load buses (PQ), once the limit is reached. The presented approach is based on enforcing the transversality condition (i.e. degeneracy of power flow Jacobian) as an additional equation in order to find a solution sitting at the boundary for faster computations in comparison to the continuation based algorithms. The algorithm is validated by the analysis of several IEEE test networks.

Index Terms - Newton-Raphson, Reactive power capability, Slack variables, Voltage stability.

I. INTRODUCTION

The gradual rise of the electric demand in the last couple of decades and rapid penetration of renewable generation made the power system operation highly vulnerable to all kinds of instabilities. Economic and environmental concerns, which have constrained the construction of additional system infrastructure, were also the contributing factors [1], [2]. The instability of power systems resulted in large scale voltage collapse and blackouts, as observed in the USA, Europe and Asia during the 1970's and 80's. [1], [3]. Voltage instability has been regarded as one of the most important areas of research in the power system community. A power system becomes more vulnerable to voltage collapse when it reaches the limit on reactive power generation [2] or other technological constraints, such as voltage magnitude constraint on load buses, current and power transfer limits, etc. When the system reaches the reactive power capability limit, the equations describing the system should undergo a sudden change from describing the generation buses to describing the load buses. In [2] the change of equations, when the reactive power limit is reached was defined by the constant excitation current equation instead of the constant voltage magnitude equation. Such quick change in the system model might cause a discontinuous change in the system stability [2], while there are some examples when the system remains stable even when the generation limit is encountered [4], [5]. The robust operation of the power system requires identification of the solution that sits at the feasibility boundary, as the system might behave undesirably near there [6]. Feasibility boundary consists of solutions that bound the operating point within the stability limit of loadability and technical operating constraints. Several numerical methods have been introduced that find the points on such boundary. Typically, the main objective is to find a feasible solution of the power system, when it is subjected to loadability and technological constraints such as the voltage magnitude constraints on load buses and reactive power capability limit on voltage controlled buses. The method discussed in our work is based on extension of the Transversality Enforced Newton Raphson (TENR) algorithm [7], that provides a means of fast computation of the boundary points as compared to the continuation Newton Raphson algorithm. TENR algorithm extends the system of equations (i.e. power flows and technological constraints) with an additional constraint that enforces the power flow Jacobian to degenerate on the feasibility boundary. At the same time, the technological inequality constraints are converted into equality equations with the help of a slack variable approach. The resulting system of equations remains regular even at the loadability limits and can be easily solved via regular Newton Raphson techniques. The key contribution of this work lies in the extension of the originally introduced TENR technique with additional equations that provide a means of modeling the real generator switching from PV to PQ buses. Section II describes the abstract notation for the system of equations to be solved, section III gives an overview of the TENR algorithm used to solve the system given by (1). Details about power flows and feasibility constraints are discussed in section IV, section V and VI covers the details of implementation and numerical experiments for different IEEE test cases. The conclusion is provided in section VII.

M. Ali is with the Center of Energy Systems, Skolkovo Institute of Science and Technology, and working with Prof. K. Turitsyn from MIT, Department of Mechanical Engineering. e-mail: mazhar.ali@skolkovotech.ru

II. MATHEMATICAL FORMULATION

The set of equations describing the power flows and feasibility constraints can be expressed in the following standard way:

$$f_i(x, \lambda) = 0, \quad i = 1 \dots n \quad (1)$$

Here $x \in \mathbb{R}^n$ Here is the vector consisting of system variables, $f_i : \mathbb{R}^n \times \mathbb{R} \rightarrow \mathbb{R}^n$ is the system of nonlinear equations representing both the power flows and the feasibility constraints as described in the subsequent section. Here λ is considered as load parameter for a problem of finding the critical load parameter λ_{\max} that describes the range of loading levels λ for which the solution of (1) exists if: $0 \leq \lambda \leq \lambda_{\max}$. Formally, the load level is defined as follows: $\lambda = 0$ corresponds to the base case solution, while $\lambda = \lambda_{\max}$ relates to critical load condition.

The solution corresponding to the boundary of feasible solutions (i.e. for $\lambda = \lambda_{\max}$) must satisfy (1) and an additional equation that defines the singularity of the power flow Jacobain [6].

$$\det(J_{ij}) = 0 \quad (2)$$

Here $J_{ij} = \partial f_i / \partial x_j$ is the gradient of (1) with respect to x . Standard Newton-Raphson iterations can be used to solve (1) and (2) simultaneously. The overview is presented in the next section.

III. AN OVERVIEW OF TENR ALGORITHM

As λ approaches to λ_{\max} the standard Newton iterations fail to converge as the Jacobain becomes singular. Here the system is extended to enforce the degeneracy of Jacobain along with (1). Such condition, is referred to as «Transversality» condition, standard Newton iteration can be used to solve such equations without convergence or numerical stability issues [8]. The Newton-Raphson algorithm is therefore referred to as Transversality Enforced Newton Raphson (TENR) algorithm here. The following compact notation describes the extended system of equations:

$$f_i(x, \lambda) = 0, \quad i = 1 \dots n \quad (3a)$$

$$g(x) = 0. \quad (3b)$$

Here $g(x)$ is referred as transversality condition, which describes the Jacobian degeneracy. The most natural and obvious choice for $g(x)$ is based on determinant, but such choice is sensitive to perturbation and not scalable for large test cases [8]. There are several possible choices for $g(x)$ other than determinant, which are either vector or scalar transversality choices as described in [6], [7], [8], [9]. Here a scalar condition is used based on QR decomposition. For QR decomposition $J = QR$ with matrix Q is an orthogonal matrix composed of n orthonormal vectors $Q = [q_1 \dots q_n]$. R is an uppertriangular matrix. The QR decomposition is simply a matrix representation of the Gram-Schmidt orthogonalization procedure. Whenever the Jacobian matrix $[\partial_x f]$ is close to being singular, the lower right element R_{nn} of the matrix R is close to zero. So the direction q_n is almost aligned with the normal to the solvability boundary. The transversality choice $g_{QR} = R_{nn}$ remains well conditioned and can be scalable for large test networks comparing to other choices, as discussed in [7]. Also the gradient can be easily be defined for g_{QR} .

IV. POWER FLOWS AND FEASIBILITY CONSTRAINTS

This section describes the system of equations used to define (1), i.e. nonlinear power flow model and equations for feasibility constraints.

A. Power flow equations: In the first implementation of the algorithm, the system of power flow equations is presented in a rectangular coordinates. This allows neglecting higher order terms in Taylor series as the equations appear in the quadratic form [10]. For the rectangular formulation, the voltage phasor at each bus i is represented using rectangular coordinates: $\hat{V}_i = V_i^r + jV_i^m$. The rectangular formulation of power flow equations is given below with a slight modification in order to include loadability parameter λ :

$$\sum_k \left\{ V_i^r (G_{ik} V_k^r - B_{ik} V_k^m) + V_i^m (G_{ik} V_k^m + B_{ik} V_k^r) \right\} - (P_{\text{gen},i} - P_{\text{load},i})(1 + \lambda) = 0 \quad (4)$$

$$\sum_k \left\{ V_i^m (G_{ik} V_k^r - B_{ik} V_k^m) - V_i^r (G_{ik} V_k^m + B_{ik} V_k^r) \right\} - (Q_{\text{gen},i} - Q_{\text{load},i})(1 + \lambda) = 0 \quad (5)$$

Here $\hat{Y}_{ij} = G_{ij} + jB_{ij}$ gives the complex admittance between buses i and j .

B. Feasibility Constraints: There are several technical constraints in the operation of the power system like voltage magnitude constraints on PQ (load) buses, current and power transfer limits through lines and reactive power capability limits on PV (generators) buses etc. Thus, finding a solution on the boundary corresponding to loadability and technical constraints is computationally challenging, as the stability of the algorithm can be compromised due to the topology of the solution space near the boundary. Here, we consider only two technical constraints as explained below.

A. Voltage magnitude constraints: Here we give an overview of technical constraints on the voltage magnitude for the PQ buses, such that the solution can be obtained easily with TENR algorithm [7]. The inequality is the following:

$$|\hat{V}_i|_{\min} \leq |V_i|_{\text{cal}} \leq |\hat{V}_i|_{\max} \quad (6)$$

Here $|V_i|_{\text{cal}} = \sqrt{(V_i^r)^2 + (V_i^m)^2}$ defines the voltage magnitude level at PQ buses. In order to have a solvable solution to (6), slack variables were introduced to convert the inequality into two different equality equations corresponding to $|\hat{V}_i|_{\max}$ and $|\hat{V}_i|_{\min}$.

$$(V_i^r)^2 + (V_i^m)^2 = |\hat{V}_i|_{\max}^2 - (\bar{s}_i)^2 \quad (7a)$$

$$(V_i^r)^2 + (V_i^m)^2 = |\hat{V}_i|_{\min}^2 + (\underline{s}_i)^2 \quad (7b)$$

$$(7c)$$

Here $|\hat{V}_i|_{\max}$ and $|\hat{V}_i|_{\min}$ presents the maximum and minimum voltage magnitude limits on the PQ buses, while \bar{s}_i and \underline{s}_i denote the slack variables corresponding to such limits. There exists a real solution for slack variables in (7) if the solution exists, and vice-versa, a solution does not exist if the limits are violated. The next section covers the details about introducing the feasibility constraints on reactive power generation.

B. Reactive power capability constraints: It's one of the important feasibility constraint, as the system becomes more vulnerable to collapse when the reactive power limit is reached requiring changes of system equations [2]. In order to have a solvable solution for the inequality constraints on reactive power limits of generators, this constraint is defined using the same slack variable technique as in the previous section with some additional equation and variables for switching the bus from PV to PQ, once the limit is violated. Let's first consider the reactive power generation level at a PV buses in a n bus system:

$$Q_{\text{gen},i} = \sum_k \left\{ V_i^m (G_{ik} V_k^r - B_{ik} V_k^m) - V_i^r (G_{ik} V_k^m + B_{ik} V_k^r) \right\} + Q_{\text{load},i} \quad (8)$$

$$Q_{\text{gen},i} = Q_{\text{cal},i} + Q_{\text{load},i} \quad (9)$$

The inequality can be presented as follows:

$$(Q_{\text{gen},i})_{\min} \leq Q_{\text{gen},i} \leq (Q_{\text{gen},i})_{\max} \quad (10)$$

Here $(Q_{\text{gen},i})_{\min}$ and $(Q_{\text{gen},i})_{\max}$ describe minimum and maximum limit of the reactive power generation respectively. The inequality in (10) can be converted into equality as presented below, by introducing the slack variables \bar{c}_i and \underline{c}_i , such that the slack variables remains real if the solution exist and vice-versa when the solution doesn't exist.

$$(Q_{\text{cal},i} + Q_{\text{load},i}) = (Q_{\text{gen},i})_{\max} - (\bar{c}_i)^2 \quad (11a)$$

$$(Q_{\text{cal},i} + Q_{\text{load},i}) = (Q_{\text{gen},i})_{\min} + (\underline{c}_i)^2 \quad (11b)$$

In order to address the switching of the bus from PV to PQ, once the (10) is violated, an additional slack variable t_i was introduced for the equation that describes the constant voltage magnitude of PV buses, in the following way:

$$(V_i^r)^2 + (V_i^m)^2 = |\hat{V}_{\text{ref}}|^2 + t_i \quad (12)$$

such that:

$$t_i \cdot \bar{c}_i \cdot \underline{c}_i = 0 \quad (13)$$

The following scenarios can be considered:

Case 1: If only $t_i = 0$ in (13) then it means reactive generation constraints (11) hold and \underline{c}_i and \bar{c}_i will have real solutions and the bus remains PV.

Case 2: If only $c_i = 0$ in (13) then it means $Q_{\text{gen},i}$ reaches $(Q_{\text{gen},i})_{\text{min}}$ and the system changes its state from PV to PQ.

Case 3: If only $\bar{c}_i = 0$ in (13) then it means $Q_{\text{gen},i}$ reaches $(Q_{\text{gen},i})_{\text{max}}$ and the system changes its state from PV to PQ.

Case 4: When $t_i = 0$ and also either \bar{c}_i or c_i will be equal to zero in (13), it means $Q_{\text{gen},i}$ might have reached the $(Q_{\text{gen},i})_{\text{max}}$ or $(Q_{\text{gen},i})_{\text{min}}$ but didn't violate this limits, thus the bus will remain PV. But, in order to consider the practical scenario the right hand side in (13) is considered to be equal to rather than equal to zero.

$$t_i \cdot \bar{c}_i \cdot c_i = \epsilon \quad (14)$$

Here ϵ is chosen to be 10^{-4} , the reason for that is to allow some flexibility for enforcing condition (13) from the real case. It is possible to use additional constraints like current or power transfer limits on the lines. In our numerical experiments, the analysis was restricted to only voltage magnitude constraints on PQ buses and reactive power capability limits on PV buses to keep the analysis and implementation simple.

Here (1) describes the system of equations consisting of (4), (5), (7) for every PQ bus and (4), (11), (12) and (14) for every PV bus in the system. The variables in x are as follows: V_i^r , V_i^m , \bar{s}_i and \underline{s}_i for every PQ bus and V_i^r , V_i^m , \bar{c}_i , \underline{c}_i and t_i for every PV bus in the system.

V. IMPLEMENTATION

For all the test cases, the method was initiated with a flat start. A Matlab script was developed for the TENR algorithm for computing solutions corresponding to feasibility boundary. There are many possible choices for the assessment of the stability of the system. Here a universal stability index was defined based on singular value decomposition (SVD), for $J = U\Sigma V^T$ with orthogonal matrices U and V and diagonal matrix Σ . Once the J becomes singular, the minimum singular value i.e. σ_{min} becomes equal to zero, it is a natural and more stable measure of stability. We define a relative measure of σ_{min} with the following expression:

$$\text{Stability Index} = \frac{\sigma_{\text{min}}(\tau)}{\sigma_{\text{min}}(0)} \quad (15)$$

Here τ defines the Newton iterations. The Index varies from 1 (i.e. $\lambda = 0$) to 0 (i.e. $\lambda = \lambda_{\text{max}}$).

VI. NUMERICAL EXPERIMENTS

In this section, IEEE 14 and 30-bus [11] test cases were considered for finding solutions corresponding to the feasibility boundary and solved with both feasibility constraints from section IV-B. These experiments were used for the assessment of performance, robustness and numerical instabilities encountered during the computations.

A. The 14-bus IEEE test case: Several loading scenarios were considered, one of the cases is the following: both active and reactive loads were increased at each bus in the system proportional to the base case and also the active generation was increased proportionally in order to compensate the growth in load. The system was also subjected to voltage magnitude constraints on PQ buses with $\pm 5\%$ to the nominal value and reactive power limits of generation as well. The solution was obtained with $\lambda_{\text{max}} = 0.06$. Figure.1 shows the trajectory of the stability index with respect to Newton iteration, the algorithm was stable and the solution was obtained with an adequate number of iterations. It was observed that the generators 2, 3 and 6 violated the reactive power limit to the maximum reactive

power generation, this is most likely because these generators were providing reactive power support for maintaining voltage magnitudes at PQ buses within $\pm 5\%$ bound. Due to violation to the maximum reactive limit, the state of these generators was changed from PV to PQ, and resulted in the higher voltage magnitude values. Only generator 8 remained in the limit of reactive power constraint.

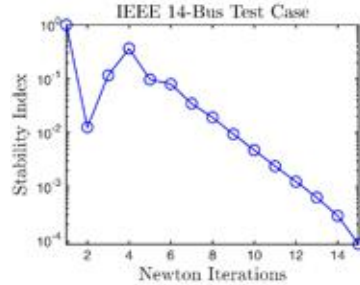


Fig. 1. Trajectory of stability index for IEEE 14-bus test case

Table I. Summary of results for IEEE 14-bus cases

Generator (p.u.)	$ \hat{V}_i $ (p.f.)	$ \hat{V}_z $ (p.u.)	t_i	\underline{c}_i	\bar{c}_i
2	1.0450	1.0480	0.0062	0.9487	0.0002
3	1.0100	1.0277	0.0257	0.6325	0.0001
6	1.0700	1.0736	0.0076	0.5477	0.0003
8	1.0900	1.0900	0.0000	0.5476	0.0109

Table I shows the details of the result for this 14-bus case, here $|\hat{V}_i|$ denotes voltage magnitude for generator buses with $\lambda = 0$ and $|\hat{V}_z|$ describes voltage magnitude for generator buses with $\lambda = \lambda_{\max}$, while t_i , \underline{c}_i and \bar{c}_i are the slack variables from reactive power limits constraints.

B. The 30-bus IEEE test case: The 30-bus test case, different loading scenarios were also considered. The first case both active and reactive loads and active generations were increased proportionally to the base case, and the feasibility constraints were kept the same as in the previous section. It was observed that the system reached the loadability limit with $\lambda_{\max} = 0.0578$. It was noticed that generators 2, 5 and 8 remained within the limits, that is why $t_2 = t_5 = t_8 = 0$ and thus the state was unchanged. The generator 11 converged to the minimum on reactive generation, thus the value of the voltage magnitude was dropped at bus 11 as the state of this generator was switched to PQ. While the state of generator 13 was also changed to PQ, as it converged to the maximum on reactive power generation and voltage was increased from the base value. The trajectory of the stability index with respect to Newton iteration is monotonic in Fig.2. Table II shows the result for this 30-bus case.

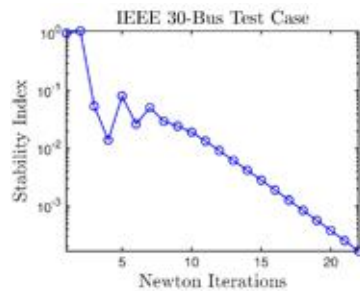


Fig. 2. Trajectory of stability index for IEEE 30-bus test case

Table II. Summary of results for IEEE 30-bus cases

Generator (p.u.)	$ \hat{V}_i $ (p.f.)	$ \hat{V}_i $ (p.u.)	t_i	\underline{c}_i	\bar{c}_i
2	1.0430	1.0430	0.0000	0.9485	0.0201
5	1.0100	1.0100	0.0000	0.8858	0.1239
8	1.0100	1.0100	0.0000	0.6480	0.2830
11	1.0820	1.0667	-0.0328	0.5477	-0.0001
13	1.0710	1.1018	0.0669	0.5477	0.0000

VII. CONCLUSION

The algorithm provides a stable, fast and reliable way to compute solutions corresponding to the boundary of feasibility with to additional constraints. The implementation and initialization is rather easy and straightforward comparing to some other algorithms. The introduction of reactive power capability constraints presented here allows to find a solution and also to simulate all possible scenarios when the system remains within certain limits or when the limits are violated. Future plans include introducing additional technical constraints and developing an algorithm for exploring the boundary of feasibility.

ACKNOWLEDGMENT

The author would like to thank Prof. Anatoly Dymarsky (from Skoltech) and Prof. Konstantin Turitsyn (from MIT) for supervising this work.

REFERENCES

- [1] P. Löf, T. Smed, G. Andersson, and D. Hill, "Fast calculation of a voltage stability index," *Power Systems, IEEE Transactions on*, vol. 7, no. 1, pp. 54–64, 1992.
- [2] I. Dobson and L. Lu, "Voltage collapse precipitated by the immediate change in stability when generator reactive power limits are encountered," *IEEE Transactions on Circuits and Systems I: Fundamental Theory and Applications*, vol. 39, no. 9, pp. 762–766, 1992.
- [3] Y.-H. Moon, H.-S. Ryu, J.-G. Lee, and B. Kim, "Uniqueness of static voltage stability analysis in power systems," in *Power Engineering Society Summer Meeting, 2001*, vol. 3. IEEE, 2001, pp. 1536–1541.
- [4] T. Van Cutsem, "A method to compute reactive power margins with respect to voltage collapse," *IEEE Transactions on Power Systems*, vol. 6, no. 1, pp. 145–156, 1991.
- [5] M. Begovic and A. Phadke, "Analysis of voltage collapse by simulation," in *Circuits and Systems, 1989.*, IEEE International Symposium on. IEEE, 1989, pp. 1855–1858.
- [6] I. A. Hiskens and R. J. Davy, "Exploring the power flow solution space boundary," *Power Systems, IEEE Transactions on*, vol. 16, no. 3, pp. 389–395, 2001.
- [7] M. Ali, D. A. Holzer, and T. K, "Transversality enforced newton raphson algorithm for fast calculation of maximum loadability," *IEEE Transactions on Power Systems*, vol. 2nd round of revision, 2016.
- [8] J. P. Abbott, "An efficient algorithm for the determination of certain bifurcation points," *Journal of Computational and Applied Mathematics*, vol. 4, no. 1, pp. 19–27, 1978.
- [9] A. Griewank and G. W. Reddien, "Characterization and computation of generalized turning points," *SIAM journal on numerical analysis*, vol. 21, no. 1, pp. 176–185, 1984.
- [10] J. E. Tate and T. J. Overbye, "A comparison of the optimal multiplier in polar and rectangular coordinates," *Power Systems, IEEE Transactions on*, vol. 20, no. 4, pp. 1667–1674, 2005.
- [11] R. Christie, "Power system test archive," University of Washington, 1999.

Physical modeling of ZnO Nanowire Field-Effect Transistors

A.G. Askarova*, K. Kalna,

Abstract - Zinc oxide (ZnO), a metal-oxide semiconductor-like compound, is studied in this work starting with an introductory survey of its properties, main growth methods with a focus on nanowires, and the definition of the term ZnO based field-effect transistors. The top-down manufacturing approach, which uses the remote plasma atomic layer deposition on SiO₂ step defining layers, is considered. This top-down manufacturing approach is able to produce strongly reproducible high-quality ZnO nanowire field-effect transistors. The nanowires investigated in this work have channel lengths of 1.3 and 10 μm . The physical modeling is carried out within Silvaco 3D ATLAS toolbox in order to i) accurately reproduce real device geometry and to ii) obtain their I_D - V_G and I_D - V_D characteristics. A back gate approach is used to control device channel and access VT (a threshold voltage) in these devices revealing close match when no interface charge is included. Finally, the simulated I_D - V_G characteristics at low drain biases of 0.1 V and 1 V with the results measured in experiments are compared. It was found, that ZnO nanowire field-effect transistors suffer from relatively large external source/drain resistance because the simulated drain current has to be lowered by two orders of magnitude to agree with the experimentally measured current.

Index Terms - Field-effect transistor, nanowire, threshold voltage

I. NOMENCLATURE

ZnO	Zinc Oxide
FET	Field-effect transistor
ALD	Atomic Layer Deposition
VT	Threshold voltage
LED	Light Emitting Diode
OIPT	Oxford Instruments Plasma Technology
RF	Radio Frequency
I_D	Drain current
V_D	Drain voltage
V_G	Gate voltage

II. INTRODUCTION

Zinc Oxide (ZnO) is a metal-oxide semiconductor compound which inherits material properties making it very perspective for future applications in power electronics, display technology, and consumer electronics for digital logic elements. It has a substantial advantage against other alternative metal-oxide semiconductors because of its low cost and wide availability [1]. ZnO has been used for more than a century, originally as a pigment in paints, as well as for rubber, glass, porcelain, enamels, and pharmaceuticals. Due to lack of control over its electrical conductivity, the use of ZnO as a semiconductor in electronic devices has been hampered [2]. Recently, ZnO is increasingly researched for various microelectronic applications, such as photodetectors,

This work was a part of the MSc thesis of Aysylu Askarova at Swansea University

A. G. Askarova is with the Center of Hydrocarbon Recovery, Skolkovo Institute of Science and Technology, Skolkovo Innovation Center, Building 3, Moscow 143026, Russia [e-mail: aysylu.askarova@skoltech.ru].

K.Kalna is with Swansea University, Swansea, Wales, UK [e-mail: k.kalna@swansea.ac.uk]

solar cells, and light emitting diodes (LEDs) [3]. ZnO has three key advantages. Firstly, it is a semiconductor with a direct wide band gap of 3.37 eV and a large excitation binding energy (60 meV) [1]. ZnO is a functional oxide that exhibits near-ultraviolet emission and has transparent conductivity. Secondly, because of its non-central symmetry of the crystal, ZnO has strong piezoelectric properties, which is a key to building electromechanically coupled sensors and transducers [2]. Finally, ZnO is bio-safe and biocompatible and has potential for use in biomedical applications without coating. These three characteristics make ZnO unique, such that this material can be one of the most important semiconductor nanomaterial in future research and applications.

Nanowires with a high aspect ratio and a diameter less than 100 nm have demonstrated many remarkable characteristics. These structures are well suited for constructing nanoscale devices (electronic, piezo-electronic, optoelectronic and magneto-electronic), which leads to high-density circuit integration. Naturally, high-density circuit integration is capable of delivering a great performance required for future electronic applications.

Field effect transistor (FET) is an electronic device based on a semiconductor channel, which is capable of operating as a switch or an amplifier. It uses an electric field to control the shape and hence the conductivity of its channel [4]. It is possible to extract important FET parameters from the measured current-voltage characteristics. These parameters are transconductance, field-effect mobility, subthreshold swing, on/off current ratio, threshold voltage, and hysteresis.

Another important point is the development of reproducible synthesis methods that produce high-quality samples with a purpose to utilize ZnO nanowires for nanoelectronic devices. The material's crystal structure and their physical properties are driven by the methods of nanowire synthesis [5]. The conventional atomic layer deposition (ALD) used within this research has advantages such as lower growth temperature and good control of thickness, composition, and uniformity; this method has shown excellent electrical characteristics [6]. It is important to make use all of the unique advantages of ZnO nanowire FET's such as high electron mobility, high thermal conductivity, wide and direct band gap, and large exciton binding energy of ZnO; the ability to grow heterostructures and achieve vertical alignment of high quality crystals of FET nanowires; low growth temperature, and good control of thickness of remote plasma ALD. The aim of this research is to conduct the physical modelling of the ZnO FET while combining all three advantages described above and to compare simulation results with experimental data, and evaluate the reproducibility of the I_D - V_D and I_D - V_G characteristics.

III. MATERIALS AND METHODS

In this work, the paper of S. M. Sultan, K. Sun, et al. dedicated to the electrical characteristics of top-down ZnO nanowire transistors and experimental data from H. M. H. Chong (Southampton University) were used [6]. Both sources provide explanation of how the whole ZnO nanowire FET was grown on the top of a p-type Si substrate. The p-type Si substrate also acted as the transistor back gate. Figure 1 (a) shows that this back gate is first isolated by thermally growing a layer of SiO₂ with a thickness of 200 nm. To achieve effective gate operation, the dielectric needs to be as thin as possible. The SiO₂ layer was etched (anisotropically reactive ion etching) to form 100 nm pillars with step sides as shown in Figure 1 (b). After this, a 35-nm layer of ZnO was deposited at 1500 °C using remote plasma ALD in an Oxford Instruments Plasma Technology (OIPT) FlexAl. The following parameters were applied: diethyl zinc was used as the precursor, radio frequency (RF) power of 100 W, pressure of 57.5 mTorr, and O₂ flow of 60 sccm. In comparison with water-based oxidation, this method reduces OH impurities, and respectively increases the film resistivity [7]. In order to form ZnO nanowires on the sides of the SiO₂ pillars, an anisotropic reactive ion CHF₃ etch in an OIPT 80+ system was used. The nanowire width is 40 nm and height 80 nm which is determined by the height of the SiO₂ pillar and the amount of over-etch of ZnO layer. Figure 1 (c) shows an optical image of the completed ZnO nanowire FET [8].

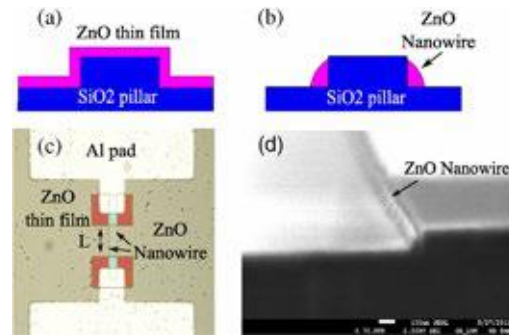


Fig. 1. a) Schematic illustration of ZnO deposition over a SiO₂ pillar; b) Schematic illustration of ZnO nanowires after etch; c) Optical image of fabricated ZnO nanowire FET; d) SEM cross section of ZnO nanowire formed at the side of a SiO₂ pillar [6].

As seen from SEM image in Figure 1 (d), ZnO layer is approximately 20% thicker on the pillar sidewall than on the planar surfaces, which accounts for this discrepancy [6]. It is essential that the electrical contacts themselves do not perturb the measurement. Hence, the metal-semiconductor contact must be Ohmic, i.e., the current drawn is linearly proportional to the applied voltage. Aluminum source and drain electrodes were deposited by means of e-beam evaporation and patterned by lift-off. In order to improve the Ohmic contact, the Al contacts were annealed at 350 °C for 2 min [6]. Next step is to reproduce the structure of the described device and obtain I_D - V_G and I_D - V_D characteristics, which can reproduce the experimental data.

IV. SIMULATION

In this work, Silvaco's commercial software tool ATLAS was employed [9]. It is one of the most common simulation software tools used in the semiconductor industry. ATLAS is a physically based simulation tool which is designed to provide simulation and modeling of the carrier transport in semiconductor devices for electronics and optoelectronics. The ATLAS simulation tool itself contains many different physical models, which can be selected to perform the practical simulations connected with the unified mesh generation and overall syntax.

Initially, the behavior of this device without Si substrate was considered. Naturally, without acting gate, I_D - V_G characteristic looked like a straight line and we were able to access channel resistance. In order to control the characteristics, the Si substrate was added to the structure and the thickness of SiO₂ was significantly reduced. The thickness of the source and the drain was increased and heavily doped. ZnO nanowire FET with thick Si substrate of 200 nm behaves like a resistor and with thin Si substrate gate starts to control the channel transport. Thus, the good I_D - V_D characteristics were obtained with behavior similar to experimental data. By changing the thickness of Si substrate, doping, and other material parameters, the desired characteristics could be derived. With the aim to obtain characteristics close to experimental data, the Si substrate with a thickness of 5.5 μm is considered [6]. Once the mesh, geometry and doping profiles are defined, characteristics of the electron transport model can be modified, the default material parameters can be changed, and physical models, which will be used in device simulations, can be defined.

From the conduction and valence band profiles it is possible to obtain the band gap energies of materials used in this device, so for ZnO, $E_G=3.4$ eV; for SiO₂, $E_G=9.1$ eV; and for Si $E_G=1.1$ eV, which corresponds to the theory. The results show that the potential is affected by the high gate voltage; the channel is wider and allows more current to flow. At $V_G=0V$, the electron concentration in Si substrate is higher near to the SiO₂ (insulator). At $V_G=5V$, the hole concentration in Si substrate is higher near to the SiO₂. ZnO nanowire FET simulation was applied to find the characteristic of the 1.3 μm and 10 μm channel lengths.

During the simulations, the main problem was convergence. Almost all convergence problems in ATLAS are caused by poor initial guess for the solution. During a bias ramp, the initial guess for any bias point was provided by a projection of the two previous results. Problems tend to appear near the beginning of the ramp where two previous results are not available. It is found that for the first and second non-zero bias solutions it

is difficult to obtain a good convergence. Once these two solutions are obtained, the projection algorithm for the initial guess is available, and solutions should all have a good initial guess.

With an aim to avoid convergence problem, step sizes in an applied bias (V_G or V_D) need to be very small, but it does not always help. It was decided to use newton method only, because the simulation could not run with a combination of gummel and newton methods [9].

It is an interesting fact that the order is very important in a solution of specification group. Original attempt was made to simulate from -40 to +40 V as a single run because experimental data were given in this order. However, simulation could run only with two separate runs from 0 to +40 and from 0 to -40. The same simulations were run with 10 μm channel length, but because of the massive structure, a vast amount of mesh points and, correspondingly, a great number of equations simulations were taking a long time. To prevent this, only half of the structure of ZnO FET with channel length 10 μm was considered. To receive correct data, the results should be multiplied by 2, because a pair of ZnO nanowires (having mirrored geometries) is measured in the experiment.

V. THE RESULTS AND DISCUSSION

The results can be formally divided into 3 groups: 1) I_D - V_G characteristics for 2 different thicknesses (1.3 μm and 10 μm) with different mobility ($\mu=10$; 1;0,1 cm^2/Vs) and with different V_D (1;5;20 V), 2) I_D - V_D family curves (experiment and simulations) for 2 different channel lengths (1.3 μm and 10 μm) and comparison between experimental and simulation data for $V_G=10\text{V}$; 3) dependence of I_D - V_D from the structure thickness.

A. I_D - V_G characteristics

Initial comparison of the experimental and simulation data for a 1.3 μm channel length ZnO nanowire FET did not demonstrate a good match. By decreasing the value of the mobility, the curves become closer to the experimental result. All these curves are obtained at a drain bias of $V_D=1\text{V}$. The main point is to achieve a close match of the threshold voltage measured in the experiment. There is a number of important effects that must be considered in evaluating the threshold voltage. First, the charges both within the oxide and at the oxide-semiconductor interface. Second, some mobile ions within the SiO_2 , which can be reduced by annealing the device. Third, a significant number of fixed positive charges in the oxide region close to the interface. Last, but not least, a voltage difference, even in the absence of an applied voltage [11].

The obtained threshold voltage for simulation data with $\mu = 10 \text{ cm}^2/\text{Vs}$ V_T is 0 V, for $\mu = 1 \text{ cm}^2/\text{Vs}$ V_T is 0 V, for $\mu = 0.1 \text{ cm}^2/\text{Vs}$ V_T is 4 V and for experimental data $V_T = 0 \text{ V}$ approximately [6]. From this, it can be seen that curves for simulation data with a mobility of 0.1 cm^2/Vs and 1 cm^2/Vs are closer to experimental data, so the mobility of the channel lies between these 2 values. The curve for the $\mu = 0.1 \text{ cm}^2/\text{Vs}$ is closer to the experiment, but the value of V_{ir} for curve with $\mu = 1 \text{ cm}^2/\text{Vs}$ and experimental data is matched. It can be concluded, that the value of the mobility of the charge carriers in the semiconductor can be taken as 1 cm^2/Vs . Figure 2 shows the comparison of simulation and experiments [6] at $V_D=0.1 \text{ V}$ channel length 10 μm .

For simulation data I_D is multiplied by 2, since only half of the structure was considered during the simulation, and also the simulation curve (pink curve) is shifted down by multiplying I_D by 10^{-2} (red curve). It caused by the presence of large external contact resistance in these newly developed ZnO nanowires. In order to obtain good FET characteristics, it is important to minimize the influence of the source and drain contact resistance on the overall device resistance. The aluminum is used for drain and source electrodes. For example, the doping of the argon - plasma treatment can reduce the contact resistance between Al and ZnO and improve the electrical performance of the FETs [11]. Since the contact material has finite resistivity, the electrostatic potential is not always uniform along the metal-semiconductor surface. In order to avoid this problem, a distributed contact resistance can be associated with any electrode.

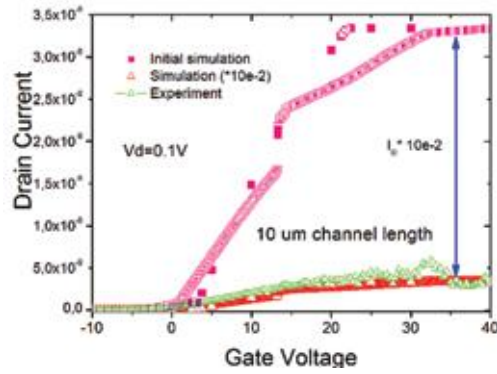


Fig. 2. I_D - V_G characteristics at a drain voltage of 0.1 V of the ZnO Nanowire FET with a 10 μm channel length comparing simulations assuming electron mobility of 10 cm^2/Vs with experimental data [6].

In addition, simulations with one carrier for the 1.3 μm channel length were made for different electron mobilities 0.1 cm^2/Vs , 1 cm^2/Vs and 10 cm^2/Vs . As can be seen from Figure 3, threshold voltage for a simulation with $\mu = 10 \text{ cm}^2/\text{Vs}$ V_T is -0.5 V, for $\mu = 1 \text{ cm}^2/\text{Vs}$ V_T is 0.4 V, and for experimental data [6], $V_T = 1.0 \text{ V}$, approximately.

Note that for two carriers the drain current is larger, and V_T is higher as well. Due to convergence problem I_D - V_G characteristics of the ZnO nanowire with different drain biases ($V_D=1 \text{ V}$, 5 V, and 20 V) were obtained only for 1.3 μm channel simulations assuming electron mobility of 10 cm^2/Vs . Figure 4 demonstrates the I_D - V_D characteristics for different electron mobilities at drain voltage of 1.0 V of the ZnO Nanowire FET with a 1.3 μm channel length.

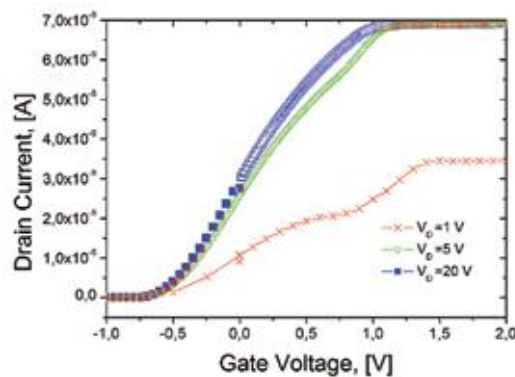


Fig. 3. I_D - V_G characteristics of the ZnO Nanowire FET with a 1.3 μm channel length comparing simulations assuming electron mobility of 10 cm^2/Vs at different drain voltages ($V_D=1$; 5; 20 V) [6].

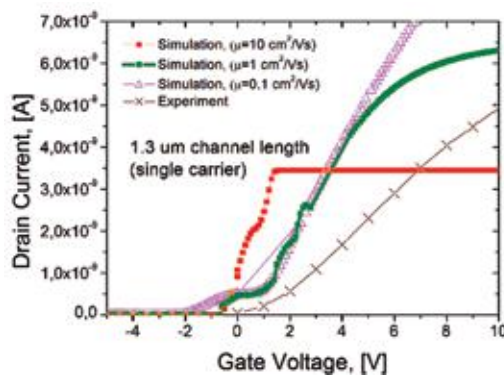


Fig. 4. I_D - V_G characteristics at a drain voltage of 1.0 V of the ZnO Nanowire FET with a 1.3 μm channel length for one carrier comparing simulations assuming electron mobility of 0.1 cm^2/Vs , 1 cm^2/Vs , 10 cm^2/Vs with experimental data [6].

Figure 3 demonstrate that with the higher drain bias, curves saturate faster at lower gate voltages. With increasing V_D the convergence, problems become negligible as it seen in I_D - V_G characteristics at $V_D=5$ V and $V_D=20$ V. Figure 4, shows, that threshold voltage for a simulation with $\mu = 10$ cm²/Vs V_T is -0.5 V, for $\mu = 1$ cm²/Vs V_T is 0.4 V, and for experimental data [6], $V_T = 1.0$ V, approximately.

B. I_D - V_D family curves

In order to compare with experimental data, I_D - V_D characteristics for two different channel lengths (1.3 μ m and 10 μ m) assuming electron mobility of 10 cm²/Vs also were obtained. Figure 5 and 6 shows simulation of I_D - V_D characteristics of the ZnO Nanowire FET with a 1.3 μ m and 10 μ m channel length respectively at different gate bias ($V_G= 0$ V, 1 V, 2 V, 4V, 10 V). Figure 7 represents the comparison between simulation data and experiments [6]. As an example, gate bias of 10 V was used and mobility is assumed to be 10 cm²/Vs. There is some problem with saturation that can be solved by reducing the value of the mobility from 10 to 1 cm²/Vs. Then, the drain current obtained from the simulations of 10 μ m channel length ZnO was multiplied by 0.01 to account for large external resistances present in the source and drain of the ZnO nanowire FETs. The results show that experimental and simulation data are not matching very well, but the shape of I-V characteristics is similar, indicating that the lower current in the experiment is due to a large impact of external contact resistance.

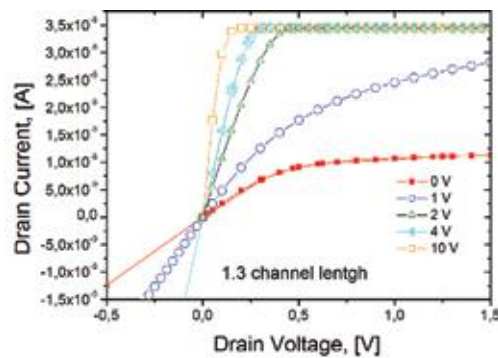


Fig. 5. Simulation I_D - V_D characteristics of the ZnO Nanowire FET at indicated gate voltages with a 1.3 μ m channel length assuming an electron mobility of 10 cm²/Vs.

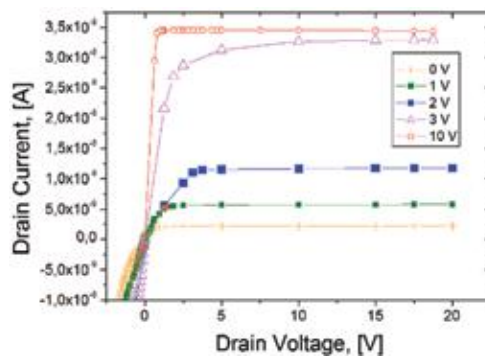


Fig. 6. Simulation I_D - V_D characteristics of the ZnO Nanowire FET at indicated gate voltages with a 10 μ m channel length assuming an electron mobility of 10 cm²/Vs.

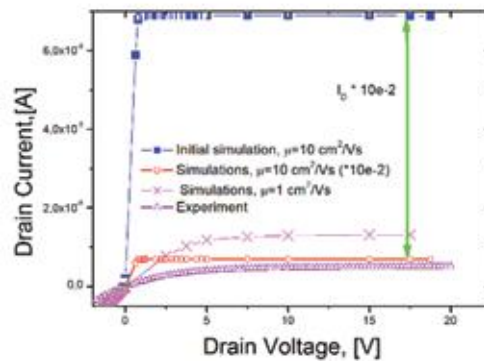


Fig. 7. I_D - V_G characteristics of the ZnO Nanowire FET with a 10 μm channel length comparing simulations assuming electron mobility of 10 cm^2/Vs and 1 cm^2/Vs , with experimental data at gate bias $V_G=10\text{V}$ [6].

By reducing the value of the mobility from 10 cm^2/Vs to 1 cm^2/Vs , the drain current is decreased with a closer agreement with experimental data. There is a better saturation regime for mobility 1 cm^2/Vs .

C. Dependence of I_D - V_D from the structure thickness

We have investigated how the thickness of the Si substrate is affecting the I_D - V_G characteristics of the ZnO Nanowire FET. We have discovered that the ON-current remains the same with the change of the Si substrate thickness. However, it can be seen from the log scale that OFF current, that the current which leaks through the device in the sub-threshold region, decreases when the thickness of a Si substrate reduces to 100 nm and increases with an increase of substrate thickness. It means that structure with the 100 nm thick Si substrate has a better gate control resulting in a significantly less leakage current in the region of -10 to 0 V.

VI. CONCLUSIONS

The modeling of ZnO nanowire FETs in this work has been performed in order to reproduce the I-V characteristics of semiconductor devices by the using the Silvaco ATLAS software. The simulations launched with the creation of the structure of a ZnO nanowire FET, and then by using and changing input file, the desired I_D - V_G and I_D - V_D characteristics were obtained. The simulations were run for two different channel lengths selected from available experimental data (1.3 μm , 10 μm). The comparison between simulations and experimental data illustrated in the plots of the I-V characteristics and the results were satisfactory. Preliminary results are presented her do not address two important effects in simulations of the ZnO nanowire FETs. I_D - V_G and I_D - V_D characteristics have similar behavior as experimental data. When the mobility is decreased to 1.0 cm^2/Vs , the I_D - V_G characteristics become closer to experiments. In experiments [6] reported value of the mobility was 1.0 cm^2/Vs . The threshold voltages close to the experimental V_T for all channel lengths were obtained. Note that surface charge [11] was not taken into account in the simulations. Furthermore, we have found from the simulations of I_D - V_G characteristics, that the change of ON-current is negligible for different thickness (100 nm, 500 nm, 1500 nm, 4500 nm, 5500 nm) of the Si substrate (which serves as a back gate of the nanowire transistor). However, the OFF current reduces significantly from 10^{-16} A to 10^{-41} A when the thickness of the Si substrate is reduced from 5500 nm to 100 nm. This can be seen in Figure 7, which visualizes the OFF current on a logarithmic scale.

It was found that for the 10- μm channel length, there is a presence of a large external contact resistance. As was mentioned the I_D - V_G graphs for simulation data with a channel length of 10 μm at drain bias $V_D=0.1$ V and I_D - V_D (a channel length of 10 μm), characteristics were shifted by two orders of magnitude with the aim to match with experimental data. We assume that, at low drain biases, these problems may also occur. When using the

experimentally measured value of the mobility ($1.0 \text{ cm}^2/\text{Vs}$) in simulations and comparing with measured characteristics, we see that the external contact resistance is still relatively large, in orders of $\text{M}\Omega/\text{cm}^2$.

Threshold voltages for different channel length at different drain voltages, agree well with experimental measurements when the correct thickness of the substrate and the correct value of the mobility $1.0 \text{ cm}^2/\text{Vs}$ are considered. Note that this close agreement has been achieved despite the fact that we have not included surface charge (observed experimentally [10]) into simulations.

VII. REFERENCES

- [1] Nandy, S. , Chakraborty, S. (2007), Structural and optical properties of ZnO films grown on silicon and their application in MOS devices in conjunction with ZrO_2 as a gate, *Bulletin of Material Science* 30 (3), pp 247-291.
- [2] Janotti, A., Van de Walle, C. G. (2009). Fundamentals of zinc oxide as a semiconductor. *Reports on progress in Physics*. 72 (1), 29.
- [3] Omar, K. (2009). Dielectric constant of Zinc Oxide. *Modern Applied Science* 3 (2), 1-2.
- [4] Millman, J., Halkias, C.C. (1985). Field effect transistor. In: *International Student Edition Electronic devices and circuits*. Tokyo: McGraw Hill, pp. 384-385.
- [5] Chang, P. C., Lu, J.G. (2008). ZnO nanowire field-effect transistors. *IEEE Transactions on Electron Devices* 55 (11), 2977-2984.
- [6] Sultan, S.M., Sun, K., Clark, O.D., Masaud, T.B., Fang, Q., Gunn, R., Partridge, J., Allen, M.W., Ashburn, P., Chong H.M.H., Member IEEE (2012). Electrical characteristics of Top-Down ZnO Nanowire transistors using remote plasma ALD. *IEEE Electron Device Letters* 33 (2), 203-205.
- [7] Kwon, S., Bang, S., Lee, S., Jeon, S., Kim, H., Gong, S.C., Chang, H.J., Park, H.-H., Jeon, H. . (2009). Characteristics of the ZnO thin film transistor by atomic layer deposition at various temperatures. *Semiconductor science technology*. 24 (3), 035015.
- [8] Sultan, S. M., Clark, O.D., Masaud, T.B., Fang, Q., Gunn, R., Hakim, M.M.A., Sun, K., Ashburn, P., Cnong, H.M.H. (2012). Remote plasma enhanced atomic layer deposition of ZnO for thin film. *Microelectronic Engineering* 97 (1), 162-165.
- [9] Cambridge Nanotech. Ltd. (2013). Atomic Layer Deposition. Available: <http://www.cambridgenanotechald.com/atomic-layer-deposition.html>. Last accessed 23th Aug 2013.
- [10] Hong, W.-K., Jo, G., Kwon, S.-S., Song, S., Lee, T.. (2008). Electrical properties of Surface - Tailored ZnO Nanowire Field-Effect transistors. *IEEE Transactions on electron devices*. 55 (11), 3021.
- [11] Park, D.J., Lee, J.Y., Kim, D.C., Mohanta, S.K., Cho, H.K. (2007). Defects in interface layers and their role in the growth of ZnO nanorods by metalorganic chemical vapor deposition. *Applied physics letters*. 91 (14), 143-115-1- 143-115-3.

The Influence of External Factors on the Dynamics of a Lipid Molecule in the Computer Modeling

Lyudmila Khakimova*, Pavel Buslaev, Ivan Gushchin, Artem Myasnikov

Abstract - Modeling of biological membranes by the method of Molecular Dynamics is a convenient approach for determining both the properties of membranes themselves and the macroscopic characteristics of biological systems (their structure, thermodynamics, and kinetics). For greater reliability of simulation results, it is necessary that the statistical and dynamic parameters of the system correspond to the experimentally obtained data. But such a correspondence does not guarantee accuracy in evaluating the properties of individual lipid molecules in the membrane, so these parameters are averaged throughout the system. In this work, it is shown how the method of Principal Component Analysis allowed providing a robust analysis of the conformational dynamics of the lipid molecule, selecting the most significant movements of lipids and ranking them according to the contribution to the conformational changes. With the help of the before mentioned method, it was possible to study the conformational dynamics of an individual lipid in a bilayer under different external factors of the system. For this purpose, several homogeneous and heterogeneous membrane complexes were collected and parametrized in the CHARMM family force fields. The effect of temperature and composition was determined.

Index Terms - Molecular Dynamics, Principle Component Analysis, lipid bilayer, dynamics of lipid molecule.

I. INTRODUCTION

The cell membrane consists of various types of lipids forming a bilayer, as well as membrane proteins. The functioning of membrane proteins and complexes directly affect the state of the entire organism. The lipid environment was shown to influence the operation of membrane proteins and complexes [1]. Therefore, the study of the behavior of lipids in cell membranes is of interest.

Existing experimental methods of studying membranes do not allow one to observe the behavior of an individual lipid, which participates in the formation of a lipid environment for a membrane protein. Moreover, Molecular Dynamic (MD) [2] simulations only do not guarantee accuracy in evaluating the properties of an individual molecule either, since these parameters are average throughout the system. However, further analysis of simulation results based on the method of Principal Component Analysis (PCA) [3] allows us to select the most significant lipid movements and rank them according to the contribution to conformational changes and to analyze the dynamic properties of a single molecule [4].

L. Khakimova is with the Center of Hydrocarbon Recovery, Skolkovo Institute of Science and Technology, Skolkovo Innovation Center, Building 3, Moscow 143026, Russia (e-mail: Lyudmila.Khakimova@skoltech.ru).

Gushchin is with Institute of Complex Systems (ICS), ICS-6: Structural Biochemistry, Research Centre Juelich, 52425, Juelich.

P. Buslaev is with Moscow Institute of Physics and Technology, Moscow, Russia

Myasnikov is with the Center of Hydrocarbon Recovery, Skolkovo Institute of Science and Technology, Skolkovo Innovation Center, Building 3, Moscow 143026, Russia.

The purpose of this work is to improve the method of analyzing the conformational dynamics of a lipid molecule, as well as apply this method to real systems of lipid bilayers (determining the relationship between lipid conformation and macroscopic parameters of the system). To achieve this goal, we provided the following steps:

- 1) Homogeneous and heterogeneous bilayers were prepared;
- 2) A simulation of ~ 1000 ns was performed;
- 3) A method of determining the orientation of the lipid in relation to the normal to bilayer was developed;
- 4) The effect of temperature and cholesterol in the membrane on lipid dynamics was studied.

II. METHODS

A. Lipids

The fundamental elements forming the biological membrane are amphiphilic phospholipids. Due to the combination of the polar and non-polar regions, the lipid acts as amphiphilic one, which is the reason for its self-organization into ordered structures in the aquatic environment. For the study of lipid bilayers, Dioleoylphosphatidylcholine (DOPC) is often used as a model lipid (Figure 1).

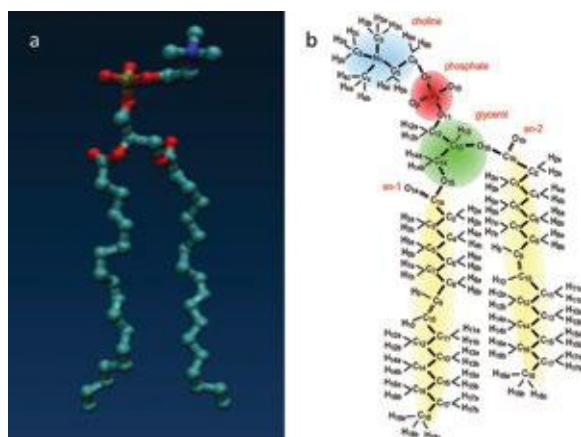


Fig. 1. (a) A screenshot of lipid molecule from the simulation; (b) Structure of DOPC molecule.

Alongside phospholipids, there are sterols in the biological membrane that play a significant role in the functioning of membranes. An essential sterol being contained in the membranes of mammals is cholesterol. The molecule of cholesterol provokes the alignment and ordering of the nearby molecules of phospholipids, thereby causing condensation of the membrane, increasing its thickness and decreasing the area [5].

In this paper, we used homogeneous and heterogeneous membrane systems. Homogeneous bilayers contained only one type of lipid - DOPC, and heterogeneous ones were bilayers of DOPC with different concentrations of cholesterol.

Homogeneous bilayer consisted of 72 molecules of DOPC under CHARMM27 force field [6] (Figure 2). This system was initially balanced since it represented the last frames of the 100-ns trajectory obtained by Sue's group [7].

For studying the effect of cholesterol in the membrane on the dynamics of DOPC molecules, three membrane systems with 0, 20 and 40% concentration of cholesterol were collected (Figure 2). Each of these systems was compiled with the help of the Charmm-gui constructor and contained 128 lipids.

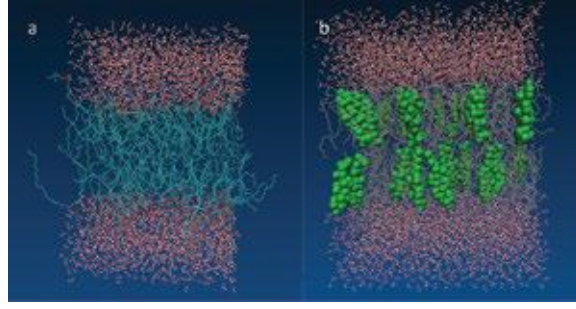


Fig. 2. (a) A screenshot from simulations of the homogeneous DOPC lipid bilayer; (b) a screenshot from simulations of the heterogeneous DOPC lipid bilayer with cholesterol.

B. Computer simulation of lipids

The main method used to model lipid systems is the method of Molecular Dynamics (MD), where equations from Newtonian mechanics are used to describe the time evolution (trajectory) of interacting particles. Using the basic concepts of statistical mechanics from the obtained trajectory, it is possible to reveal various time-dependent structural, dynamic, and thermodynamic properties of the system.

One of the critical requirements for MD simulation is an appropriate determination of potential energy function of the system $U(\mathbf{r}_1, \mathbf{r}_2, \dots, \mathbf{r}_N)$. On the one hand, this function should describe the interactions between the atoms of the system in the best way. On the other hand, it should be simple enough for computer calculations, and therefore, combine various sets of approximations. The final form of this function together with all parameters is called the force field. The general form of the potential energy in different force fields is almost the same, however, they can differ significantly in the calculation of individual contributions. In general, the potential energy of the system is written as:

$$U(\mathbf{r}_1, \mathbf{r}_2, \dots, \mathbf{r}_N) = U_{bond} + U_{nb}, \quad (1)$$

where N - number of interacting atoms, \mathbf{r}_i - position vector of atom i , U_{bond} - potential of the valence interactions, U_{nb} - potential of the non-valence interactions, which contains potential of the valence bonds, potential of the valence angles, potential of the dihedral angles, potential of the Van der Waals interactions and potential of the electrostatic interactions.

C. Analysis of simulation results

When it comes to analyzing the results of modeling lipid bilayers, we usually mean the determination of the following parameters: the cross area of lipid, the orientation of the polar lipid heads, order parameter, membrane thickness, electron density, diffusion of water and lipid molecules, electrostatic potential, and some others.

Despite the fact that the modeling of biological membranes by MD is a convenient approach for determining both the properties of the membranes themselves and aspects of the interaction of membranes with small molecules or proteins, all parameters estimated as a result of modeling have a macroscopic character and do not provide information on the state of an individual lipid in a membrane.

A typical lipid molecule consists of about 50 heavy carbon atoms. And since each atom has three coordinates, it is worthwhile to understand that the state of one lipid after modeling is described by a point in the ~ 150 -dimensional space. This view is hard to interpret.

One of the methods of decrease the dimension of space is PCA. We have adapted PCA to the analysis of the movement of a single lipid. In [4], an adaptation of PCA to the analysis of the movements of an individual lipid was carried out and it was shown how this method allows selecting the most significant motions and arranging them in agreement with the contribution to conformational changes. In other words, this approach includes statistical analysis of trajectories and the calculation, and further consideration of such aspects of motion as autocorrelations, probability density distributions, analysis of eigenvectors, and the study of conformational manifolds.

D. Simulation parameters

In this work, we used three force fields depending on the composition of the systems: CHARMM27 to simulate the DOPC bilayers, CHARMM36 and CHARMM36c to model bilayers, which contained different cholesterol concentrations, and TIP3P water model, suitable for the force fields of the CHARMM family.

All calculations were conducted using the software packages GROMACS [9], [10]. The primary cell was infinitely multiplied in all directions, that is, infinite boundary conditions for calculations were applied. Also the Berendsen thermostat was used, with thermostating of lipids and solvent taking place separately with a characteristic binding constant of 0.1ps^{-1} [10]. The centers of mass of the monolayers and the solvent were rigidly bound to the initial position to prevent the relative motion of the monolayers to each other in the simulation. The LINCS limitations [11] and SETTLE [12] were imposed on the bonds in the system. Integration was carried out with the help of a standard leap-frog integrator [61] with a step of 2 fs. To calculate the electrostatic forces, the method of fast accumulation PME with an interval of 0.12 nm was used.

Systems consisting of only DOPC were simulated at a constant temperature (300 K, 310 K, 323 K) and pressure. The Berendsen thermostat was used with a characteristic relaxation time of 1 ps. The systems, in which the cholesterol was contained, were also simulated at constant temperature and pressure. The characteristic relaxation time for thermal regulation was also 1 ps.

For all systems, calculated data was recorded every 10 ps. To minimize energy during the calculations, we applied the method of steepest descent. The simulation time for all systems ranged from 200 ns to 500 ns.

III. RESULTS AND DISCUSSION

A. Influence of the temperature

In this part of the work, we simulated a bilayer consisting of 72 DOPC molecules in the CHARMM27 force field at different temperatures: 300K, 310K, 323K. The length of the trajectories varied from 250ns to 500 ns.

The main stage of the analysis is the study of projections of trajectories on the main modes. Distributions of probability densities to principal components for all systems were calculated. Graphs of distributions for these systems at different temperatures are shown in Figure 3.

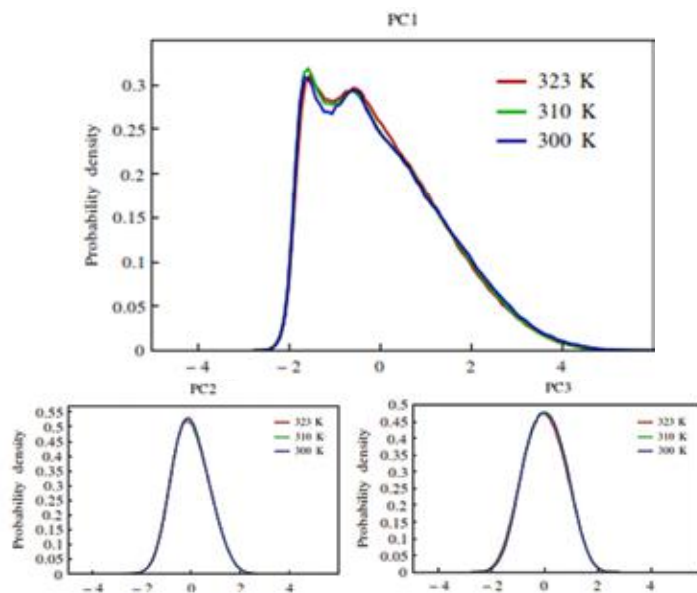


Fig. 3. Probability densities distributions for projections to the first three principal components for systems at different temperatures.

Here we can see that the distribution of the projections on the first principal component differs from the distributions of the projections on the other principal components, which are close to the normal ones. That is so because the first significant movement is the movement of the carbon tails of the lipid molecule in the same

plane. In our analysis of the effect of system temperature (and other following factors), we compared the projections to the first principal components of the systems. In this case, the projections to the first principal components at different temperatures do not differ from each other. Therefore we can suggest that the temperature of the lipid bilayer does not affect the conformation of the lipid molecule.

Figure 4 shows dependency graphs of the characteristic times of the Kolmogorov-Smirnov measure function at different temperatures. To reveal differences in relaxation times for various systems, we calculated the ratios of these times for systems at $T = 300\text{K}$ and $T = 310\text{K}$ and at $T = 310\text{K}$ and $T = 323\text{K}$, and depicted them on the same graph (Figure 5). Hence it can be concluded that the relaxation time is longer at a lower temperature.

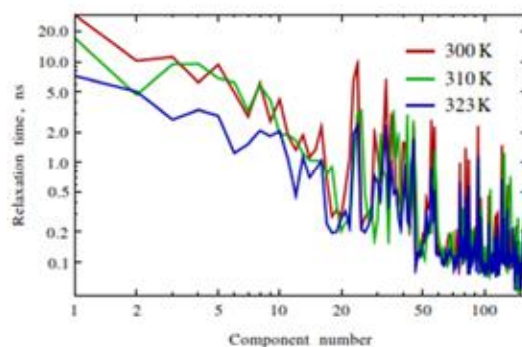


Fig. 4. Dependency graphs of the characteristic times of the Kolmogorov-Smirnov measure function at different temperatures.

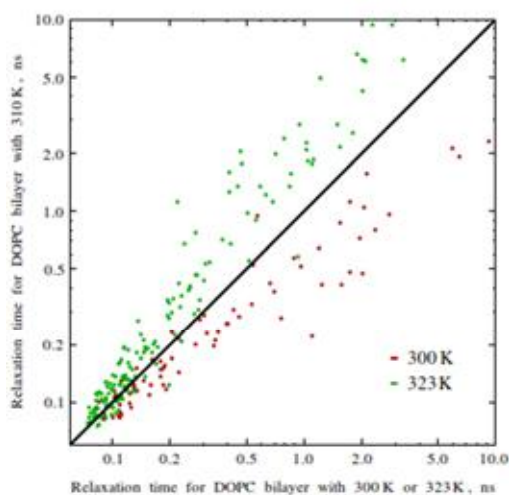


Fig. 5. Relaxation times ratio for systems with different temperatures.

B. Influence of different concentrations of cholesterol

The modeling of three systems of lipid DOPC bilayers with different concentrations of Cholesterol was carried out: 0%, 20%, and 40%.

The calculation of the projections of the trajectories on the principal components provided the following results. Figure 6 shows the probability density distribution of the projections of the trajectories of each of the three systems to the first principal component.

From the graphs, we can see the difference in the projections on the first principal component: with the increase in the concentration of cholesterol, the average projection value decreases. As discussed previously, the magnitude of the projection on the first principal component reflects the distance between the carbon tails of the lipid. Consequently, it can be concluded that the presence of cholesterol affects the conformation of the lipid molecule, specifically, reduces the distance between the hydrophobic tails.

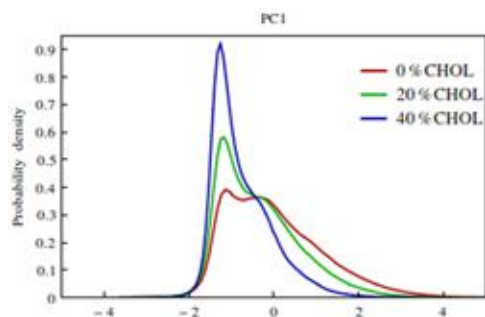


Fig. 6. Probability densities distributions for projections to the first principal component for systems at different concentrations of cholesterol.

The graph of the distribution of the angles between the hydrophobic tails of the DOPC lipid is shown in Figure 7. It is also evident that the angle between carbon tails is the less, the more the concentration of cholesterol in the bilayer.

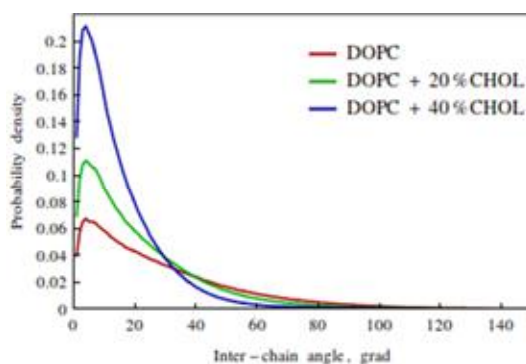


Fig. 7. Probability densities distributions for the magnitude of the angle between hydrophobic tails of the lipid for systems at different temperatures.

An analysis of the orientation of the DOPC molecule to the normal of the bilayer as a function of the cholesterol concentration gave the results. The inclination angle of the lipid to the normal of the bilayer correlates with the concentration of cholesterol in it (Figure 8).

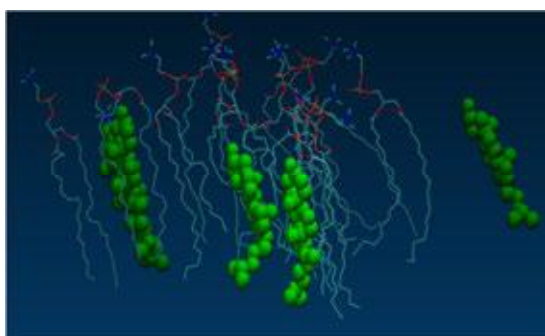


Fig. 8. A screenshot from simulations of the DOPC lipid bilayer with 40% cholesterol concentration, where the ordered deviation of DOPC molecules from the normal to bilayer is represented.

IV. CONCLUSIONS

This paper presents further development of the method of analyzing the conformational dynamics of lipids, based on the method of Principal Component Analysis, and apply it to real systems.

Thus, the influence of several macro parameters, which are usually used in the modeling of lipid bilayers, and the concentration of cholesterol on the conformational dynamics of an individual lipid molecule was studied. The following results were obtained:

- temperature affects lipid dynamics and does not affect its conformation;
- the presence of cholesterol increases the slope angle of the DOPC molecules to the normal of the bilayer and reduces the distance between the hydrophobic tails of the lipid.

V. REFERENCES

- [1] J. Singer and G. L. Nicolson, "The fluid mosaic model of the structure of cell membranes," *Science*, vol. 175, no. 4023, pp. 720–731, Feb. 1972.
- [2] K.M.Jr. Merz, "Molecular dynamics simulations of lipid bilayers", *Current Opinion in Structural Biology*, 1997, v.7, p.511-517..
- [3] I. Jolliffe, "Principal Component Analysis", Springer, 2002.
- [4] P. Buslaev et.al, "Statistical analysis of lipid molecules dynamics in the membrane" ("Статистический анализ динамики липидов в мембране"), 56 – MIPT conference, 2013.
- [5] H. Ohvo-Rekilä, B. Ramstedt, P. Leppimäki, and J. Peter Slotte, "Cholesterol interactions with phospholipids in membranes", *Prog. Lipid Res.*, vol. 41, no. 1, pp. 66–97, Jan. 2002.
- [6] S. Meloni, M. Rosati, and L. Colombo, "Efficient particle labeling in atomistic simulations," *J. Chem. Phys.*, vol. 126, no. 12, p. 121102, Mar. 2007.
- [7] S. W. I. Siu, R. Vácha, P. Jungwirth, and R. A. Böckmann, "Biomolecular simulations of membranes: Physical properties from different force fields," *J. Chem. Phys.*, vol. 128, no. 12, p. 125103, Mar. 2008.
- [8] B. Hess, C. Kutzner, D. van der Spoel, and E. Lindahl, "GROMACS 4: Algorithms for Highly Efficient, Load-Balanced, and Scalable Molecular Simulation," *J. Chem. Theory Comput.*, vol. 4, no. 3, pp. 435–447, Mar. 2008.
- [9] S. Pronk, S. Páll, R. Schulz, P. Larsson, P. Bjelkmar, R. Apostolov, M. R. Shirts, J. C. Smith, P. M. Kasson, D. van der Spoel, B. Hess, and E. Lindahl, "GROMACS 4.5: a high-throughput and highly parallel open source molecular simulation toolkit," *Bioinformatics*, p. btt055, Feb. 2013.
- [10] H. J. C. Berendsen, J. P. M. Postma, W. F. van Gunsteren, A. DiNola, and J. R. Haak, "Molecular dynamics with coupling to an external bath," *J. Chem. Phys.*, vol. 81, no. 8, pp. 3684–3690, Oct. 1984.
- [11] B. Hess, "P-LINCS: A Parallel Linear Constraint Solver for Molecular Simulation," *J. Chem. Theory Comput.*, vol. 4, no. 1, pp. 116–122, Jan. 2008.
- [12] J. B. Lim, B. Rogaski, and J. B. Klauda, "Update of the Cholesterol Force Field Parameters in CHARMM," *J. Phys. Chem. B*, vol. 116, no. 1, pp. 203–210, Jan. 2012.

Influence of Communication Signal Loss on the Results of Power System State Estimator

Irina Lukicheva*, Alexander Kulikov, Alexander Ustinov

Abstract - Reliability of power system operation strongly depends on correct estimation of electricity grid regime parameters and relevant control actions. Observability of the network is ensured by measuring its parameters. To improve measurement accuracy, state estimator is used. Although state estimator is considered to be a reliable tool, gross errors like signal losses can significantly distort the results of the procedure. In this article, the influence of signal loss on the state estimator results has been investigated. Modeling of the electric grid section was performed in software package PSCAD; situations with the loss of current and voltage signals were considered; and a state estimation by weighted least squares method with bad data detection was performed. The results of the research showed that in cases of communication channel breakdowns, state estimator may work incorrectly. Therefore, the preliminary techniques should be used to increase the accuracy of the measurements.

Index Terms - bad data detection; power system; state estimation.

I. INTRODUCTION

Nowadays, energy systems are becoming more complex and are moving towards intellectualization. Under these conditions, the requirements for the precise determination of the regime parameters are increasing. One of the tools for improving the accuracy of measurements is state estimator. Results of state estimation are used as a source data for such applications as security monitoring, contingency analysis, economic dispatch, optimal power flow and so on. However, the presence of gross errors or bad data can significantly distort its results and lead to inappropriate control actions. This misoperation may cause some faults in power system work or even blackout. The purpose of this article is to investigate the effect of measurement errors caused by the loss of the communication signal on the effectiveness of the state estimator.

II. POWER SYSTEM STATE ESTIMATOR

State estimator is a widely used tool in the centers of power systems control for improving the quality of telemetry data. It enables direct monitoring of the grid regime. The purpose of state estimator is not only the suppression of measurement additive noise, but also a detection and removal of bad data, since bad data can severely damage the results.

Irina Lukicheva is with the Center of Energy Systems, Skolkovo Institute of Science and Technology, Skolkovo Innovation Center, Building 3, Moscow 143026, Russia (e-mail: Irina.lukicheva@skolkovotech.ru).

Alexander Kulikov is with Department of Electrical Power Engineering, Electrical Engineering and Power Electronics, Nizhny Novgorod State Technical University, Minin st, 24, Nizhny Novgorod, 603950, Russia (e-mail: inventor61@mail.ru).

Alexander Ustinov is with the Center of Energy Systems, Skolkovo Institute of Science and Technology, Skolkovo Innovation Center, Building 3, Moscow 143026, Russia (e-mail: a.ustinov@skolkovotech.ru).

State estimator performs the all following 4 functions consistently [1]:

1. Topology analysis.
2. Network observability analysis.
3. State estimation (SE).
4. Bad data detection (BDD).

In this article, the last two stages are considered, because they influence on calculation of power system state.

A. State Estimation

The basis of SE is measurement redundancy. The system is described by nonlinear equations:

$$z_i = h_i(\mathbf{x}) + e_i, \quad (1)$$

where z_i - i^{th} measurement;

\mathbf{x} - vector of the real state;

$h_i(\mathbf{x})$ - function connecting the measurement and state;

e_i - measurement error distributed according to the normal distribution law, having zero mean value and variance.

The optimal state is calculated using weighted least squares method (WLS), which is described by the following objective function [2]:

$$\min_x J(x) = \sum_{j=1}^N \frac{(z_j - h_j(x))^2}{\sigma_j^2}, \quad (2)$$

where N - the number of independent measurements;

$J(x)$ - objective function;

σ_j^2 - known deviation of i^{th} measurement error

It should be noted that the method of weighted least squares is very sensitive to large errors, the presence of which can significantly "spoil" the results of the state estimation.

B. Bad Data Detection

To date, various methods for BDD have been proposed. The most widely used methods are Chi-Square Distribution Test and Largest Normalized Residual Test [1], which are used both consistently.

Firstly, Chi-Square Distribution Test is carried out in accordance with the inequality:

$$J(x) > \chi_{k,p}^2, \quad (3)$$

where $\chi_{k,p}^2$ is a value from the Chi-square distribution table, with the probability of p and freedom degrees of K :

$$K = N_m - N_s, \quad (4)$$

where N_m - the number of measurements;

$N_s = (2n-1)$ - the number of states;

n - the number of buses in electrical grid.

If the inequality (3) is true, then bad data are present in the measurements; if the inequality is false, then there are no bad data in measurement array.

When it is determined that there are bad data in the measurement array, it is necessary to determine particular measurement with a large error and exclude it from the measurement array [2]. To determine the incorrect measurement, secondly, Largest Normalized Residual Test is used: after obtaining the results of the state estimation, the measurement residual is calculated, and then the normalized measurement residual is determined; measurements having the largest residual are designated as suspicious and are deleted. After that, a new power system state is defined; then bad data detection is performed again. If no bad data are found, the defined state is accepted. Otherwise, the cycle will be carried out until all measurements with large errors are eliminated.

III. MODELING

A model of electrical grid has been developed in software package PSCAD [3] for analysis of bad data influence on state estimation accuracy (Fig. 1).

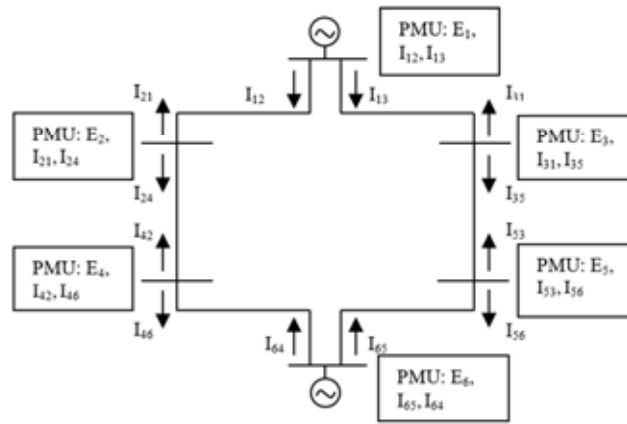


Fig. 1. Grid model used for power system state estimation

The situation of communication channel breakdown was simulated: at time $t=0,46s$ signal of E1 is equal zero and at time $t=0,48s$ the signal of I12 is equal zero. Currents in all lines and voltages of all buses were measured by phasor measurement units (PMU). It was assumed that measurements possess errors defined by characteristics of current and voltage transformers. It was presumed that the corresponding errors are normally distributed and include errors caused by phasor measurement units. After measuring, SE was performed using WLS and BDD. Results of SE without BDD are shown in Figure 2 for voltage magnitude E2 as an example.

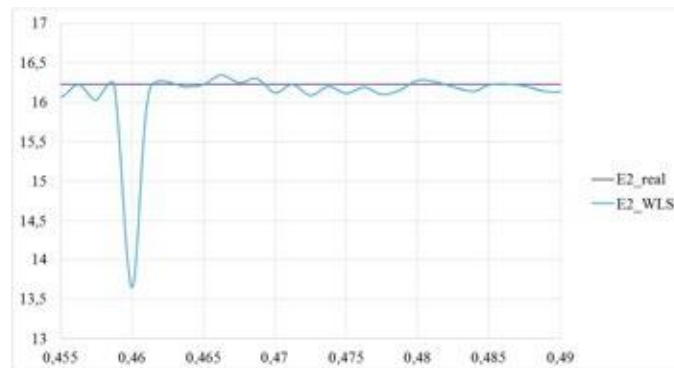


Fig. 2. Results of magnitude estimation in bus 2 E2 by WLS in case of communication channel breakdowns.

In Figure 2, the curve with index “real” (E2_real) refers to real values of voltage without any errors. The curve with index “WLS” refers to voltage values calculated by WLS.

Figure 2 illustrates that WLS produces large errors during voltage signal lose - up to 20%.

BDD led to system unobservability at the time $t=0,46s$, which means that correct power system state can not be calculated. In case of loss of current measurements, bad data were not found, because of relatively small value of the current and its slight influence on the results of the state estimation. Thus, BDD did not improve measurements accuracy and thus results of state estimator remain the same as presented in Figure.2.

IV. CONCLUSION

The simulation of WLS has shown that in the presence of local gross errors WLS is not effective enough, since it produces mistakes up to 20%. It is proposed to pre-use non-linear techniques to avoid influence of impulse noise on SE results and to improve measurements accuracy.

V. REFERENCES

- [1] Tao Yang, "Design of a two-level power system linear state estimator," Ph.D. dissertation, School of Electrical Engineering and Computer Science, Washington State Univ., Washington, 2011.
- [2] M.Tarafdar Hagh, S. M. Mahaei, K. Zare Improving. (2011, December.). Improving Bad Data Detection in State Estimation of Power Systems. International Journal of Electrical and Computer Engineering (IJECE). [Online]. 1(2), pp. 85-92 Available: <http://iaesjournal.com/online/index.php/IJECE/article/view/133>
- [3] PSCAD version 4.6, Manitoba HVDC Research Centre, 2015.

Surface Modification of Proppant for Enhanced Oil Recovery

Aliya Z. Mukhametdinova*, Alexei N. Cheremisin

Abstract - Proppant selection is critical to the success of fracturing treatments in oil production. Studies show that the performance of a regular proppant system is often improved by modifying the proppant's surface properties. These enhanced properties improve proppant conductivity within the fracture and impact on chemical protection of the proppant. Improving proppant's wettability effect enhances the proppant relative permeability and productivity of the well. This research examines different types of surface modification for a proppant system to improve the proppant quality and obtain higher functionality. According to the proposed methodology, coating the proppant with hydrophobic and hydrophilic agent may improve the quality and functionality of the regular proppant system. In this work, optimal system components are selected; proppant coating is examined; system properties to evaluate the feasibility of the chosen parameters are tested.

Index Terms - proppant; proppant pack permeability; surface modification.

I. NOMENCLATURE

dP	pressure drop (atm)
H	height of water intake column (cm)
K	permeability (D)
P	pressure (MPa)
T	temperature (0C)
θ_0	wettability contact angle (0)
m	porosity (%)
V_{pore}	porous volume of the sample (cm ³)

II. INTRODUCTION

A proppant is a granular material added to a fracturing fluid in hydraulic fracturing to enhance effective oil production. Proppant pack plays an important role in success of fracturing treatments for achieving high rate of oil and gas recovery. This study presents results on proppant coating methodology based on a series of experiments to improve the proppant quality. After defining the system components, feasibility check of the chosen parameters is performed and conclusions are made on technology advisability and possible industrial application.

Studies show that the performance of a regular proppant system is often improved by modifying the proppant's surface properties [1]-[5]. The enhanced surface properties increase proppant pack permeability, proppant pack functionality and the conductivity of the fracture, intensifying the productivity of the well. The previous studies lack research on modified proppants and offer coating the proppant grain with expensive hydrophobic agents during the proppant synthesis. Current study fills the gap in proppants coating research and focuses on both hydrophilic and hydrophobic types of surface by modifying the proppant with simple and cheap agents.

Aliya Z. Mukhametdinova is with the Center for Hydrocarbon Recovery, Skolkovo Institute of Science and Technology, Skolkovo Innovation Center, Building 3, Moscow 143026, Russia (e-mail: aliya.mukhametdinova@skolkovotech.ru).

Alexei N. Cheremisin is with the Center for Hydrocarbon Recovery, Skolkovo Institute of Science and Technology, Skolkovo Innovation Center, Building 3, Moscow 143026, Russia (e-mail: a.cheremisin@skoltech.ru).

According to the methodology proposed, coating the proppant with a surfactant and polymer may improve the quality and functionality of the regular proppant system after proppant is delivered to site. By conducting the experimental part of the project, we define the optimal system configuration and select the system components. A set of experimental testing techniques (coating topography, proppant permeability and wettability) provides data on feasibility of the chosen parameters such as the types of components, proppant and coating. This research focuses on possible improvements of the proppants systems with a variety of coatings after proppants production stage.

III. EXPERIMENTAL STUDIES

In this study, proppants manufactured by Carbo Ceramics Inc. were coated with hydrophilic and hydrophobic agents and underwent laboratory tests on coating and proppant permeability and surface quality. Based on the analyses of hydrophobic agents used or mentioned in the articles and patents, a set of proposed coatings is identified [6]-[8]. Carbo Ceramics, one of leading proppant manufacturers, was chosen as a proppant brand; proppant grain of 20/40 and 16/20 US mesh size was selected as the most commonly used frac proppants.

The following agents were used:

- IVV (hydrophobic agent) mentioned in patents review as a reliable surfactant with strong surface modification;
- CHAS (hydrophobic agent) mentioned in the literature as one of commonly used liquid additives to the fracking fluid;
- PolyQuart (PQ, hydrophilic agent) was selected for a range of experiments on both hydrophobic and hydrophilic surfaces.

Methodology of coating procedure was designed after the literature review and existing technologies. [6]-[10] Coating aqueous solution was prepared at the concentration in the range of 1.5 to 3%. The coating was applied to proppant samples (four sets of samples - 50 g, 100g, 200g, 250g) using ceramic ware and ceramic agitators with constant stirring speed for 30 minutes. The number of layers (each coating dose stands for 5-10% of proppant sample weight) was estimated visually, if necessary, additional amount was added to the wetting proppant surface for uniform application. Drying was performed at $T=25^{\circ}\text{C}$, 70°C , and 105°C .

On-fly coating is another method of coating that can be used for contact angle measurement. On-fly coating is directly applied to the proppant grain surface 3-5 minutes before the test. Then the proppant is separated from solvent, and the measurement is conducted.

Research on the proppants coating includes a set of physical and chemical methods: assessment of capillary impregnation, permeability measurement, atomic force microscopy, and measurement of the wettability contact angle. Such laboratory-testing complex enables us to evaluate the phenomenon of proppants surface modification, its effect of the coating, and estimate the industrial application of the proposed technology.

A. Capillary Intake

The method of capillary impregnation is traditionally used to determine the spontaneous absorption of water to study the capillary phenomena. Same method can be successfully applied for the study of rock hydrophilic or hydrophobic surface, and, in current case, for proppant grain samples. The wettability of proppant samples coated with IVV, CHAS and PQ water solutions changes depending on the chemical composition of a sample surface and the initial surface condition of hydrophilic-lipophilic balance. For characterization of surface wettability, a capillary intake experiment was chosen to illustrate the effect of surface modification. Changing wettability of solid surfaces from hydrophobic to hydrophilic affects spontaneous wetting ability and enhances capillary absorption [11]-[13].

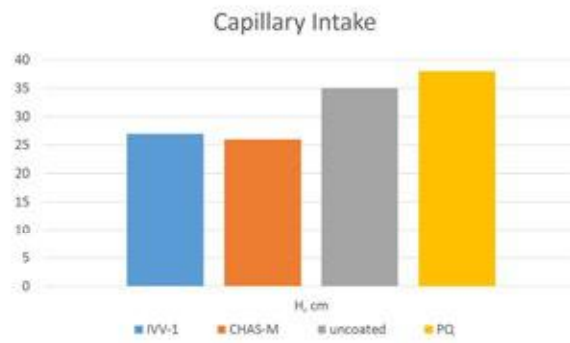


Fig. 1. Capillary impregnation test results

Figure 1 illustrates results on capillary intake test where four glass tubes filled with proppants underwent water imbibition. The experimental data on water column height suggests that the effect of the surface modification was achieved. In coating compositions with IVV and CHAS we observe a further decrease in the level of water absorbed due to the weakening of the capillary effect. As expected, the hydrophilic coating PQ increases the amount of absorbed water. However, the overall effect of the applied coating is more prominent for hydrophobic agents.

B. Permeability test

Permeability measurement and aging test were completed by using High Pressure Core Flood System (HP-CFS) which enables to carry out filtration experiments on bulk models of the porous medium and core samples at temperatures up to 150 °C, and pore pressure up to 20 MPa. If necessary, the system can use backpressure with maximum pressure of 7 MPa for bulk models and 50 MPa for core samples. Proppant aging was conducted using the same methodology as for measuring the permeability using HP-CFS. Sample aging took 48 hours at reservoir temperatures of 110 °C in the mixture of water and kerosene (15 ml kerosene and 15 ml water). Bulk pattern filled with proppant sample and emulsion (kerosene and water) was installed inside the core flood system.

Table I. Permeability Measurement at HP-CFS

n	Coating type	K, Darcy	V _{pore} , cm ³	m, %
1	IVV	42	33	30
2	PQ	21	36	33
3	CHAS	65	32	29

Table I illustrates results on permeability testing using HP-CFS. Permeability values for three types of coating (IVV, PQ, CHAS) are presented. To check the permeability change for uncoated and coated proppants the Darcy experiment was reproduced for independent study of filtration phenomena. Such test was conducted in order to observe the change of the permeability because of hydrophobization and hydrophilization.

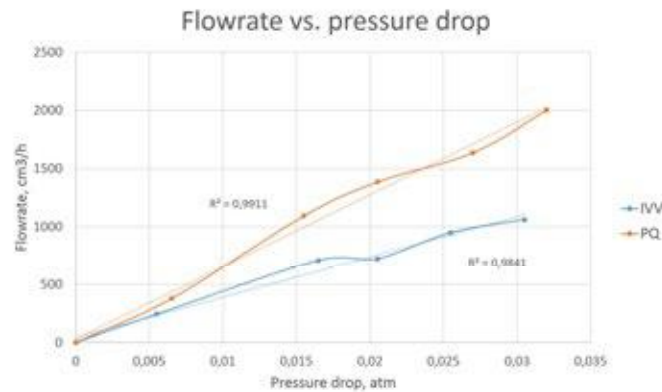


Fig. 2. Permeability test results

We observe the trend in permeability change depending on the coating type. Fast increasing flowrate (Figure 2, orange line) within a range of pressure drop reflects higher permeability of the pack of proppant covered with PQ coating agent. It proves the process of hydrophilization, which leads to increase in water-relative permeability. However, IVV hydrophobic agent curve results in slow changing of the flowrate caused by low water-relative permeability and high oil-relative permeability. Porous volume and porosity also illustrate the influence of coating on filtration and permeability change.

C. Proppant surface visualization

For the detailed study of surface quality, we examined the proppant surface for a range of samples (coated and uncoated) using an optical microscope manufactured by ThorLabs Company (Figure 3). The CarboProp 16/20 proppant as the coated sample, and 20/40 US mesh size as the aged one were selected. For topography study at atomic force microscopy (AFM) (Figure 4), 11 samples of proppants (20/40 and 16/20) were prepared. All samples included from three to five particles glued with epoxy to glass plates. Gwyddion software, a modular program for SPM (scanning probe microscopy) was used for data visualization and analysis [14].

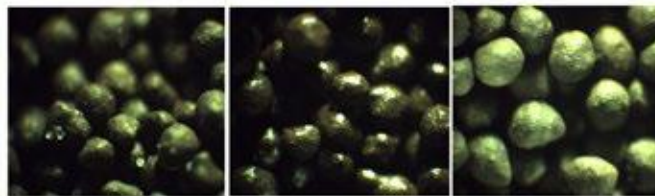


Fig. 3. Optical microscopy results for uncoated, IVV coated and aged proppant

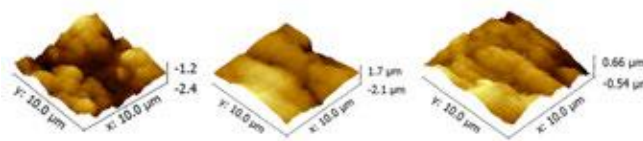


Fig. 4. AFM results for uncoated, IVV coated and aged proppant

Figure 3 demonstrates that for IVV coated proppants it is possible to notice a brilliant film coating, applied uniformly with a visual roughness decreased. Same result was obtained from AFM results for IVV coated samples examination, which also proves the roughness change for coated grain and slight decrease for aged one. Among three types of coating, hydrophilic agent PQ represents the less noticeable coating, and it becomes almost invisible after the aging procedure. It could be explained by coating structure and chemical structure of the coating polymer.

Proppant surface study enables us to determine the quality of coating and its stability. Optical microscopy is a convenient tool for visual inspection of the coating quality for a proppant pack. AFM data includes roughness values for coating stability after the aging procedure.

D. Wettability measurement

Indirect contact angle measurement is one of the alternative ways of measuring wettability, usually applied when traditional ways are not available for surface or experimental conditions [15]-[16]. Optical microscopy and high-resolution camera was used to measure the contact angle in proppant-water system. (Figure 5)

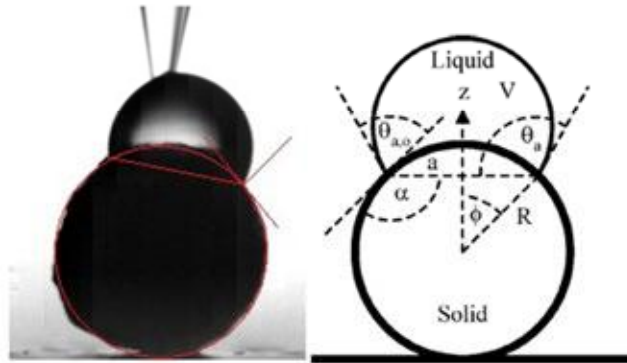


Fig. 5. Indirect contact angle measurement

Water was used as the wetting liquid in the experiments. Spheres and flats were immobilized using double-sided adhesive tape and epoxy glue. Small liquid drops were gently extruded from a one-milliliter glass syringe using a drop pump. Controlled by the FastCam camera, a small drop was placed on the proppant. Camera captured 2.7 seconds for each experiment, and that was enough to cut the moments of first and secondary contacts of drop with the proppant. By analyzing data from pictures received (Figure 5, right), values A, R and θ_a were determined and the contact angle $\theta_{a,0}$ was calculated.

Table II. Contact Angle Test Results

Parameter	uncoated	IVV	PQ	PQ Onfly	IVV onfly	IVV aged	PQ aged
θ_a , degree	73	106	68	78	87	103	86
A, pixel	98	93	102	120	88	78	81
R, pixel	78	70	70	58	69	49	52
$\theta_{a,0}$	72	105	67	77	86	102	85

Data on contact angle test shows the effect of coating that depends on the type of agent used. Table II illustrates how efficiency of the coating effect (wettability contact angle) varies for regular, on-fly and aged coatings. The methods of capillary impregnation and wettability contact angle measurement confirmed the phenomenon of surface modification of proppants. Atomic force microscopy and optical microscopy were applied to assess the quality of coating before and after aging by visual evaluation of coated proppants. Permeability measurement was the key experiment in this work that defined the possible use of proppants surface modification to control permeability depending on the coating type for different applications in oil recovery.

IV. CONCLUSION

Technology of proppants coating with hydrophobic and hydrophilic agents was studied by measuring wettability and surface quality. The data on wettability of proppant pack depending on the type of surface was obtained.

The influence of surface modification on permeability of the proppant and the porosity of proppant pack was studied. It was found that the use of the IVV and CHAS hydrophobic agents leads to a significant increase of oil phase permeability, while the hydrophilic PQ agent reduces the proppant pack permeability.

Data on proppant pack permeability and contact angle measurement illustrated the durability of coating after aging in a hydrocarbon medium and revealed the most effective coating compound. AFM and optical microscopy images were applied to evaluate the surface specifics before and after aging. Additional data on surface roughness by AFM partially proved the surface alteration after permanent coating. Laboratory testing showed that coating the proppant increases the proppant pack permeability up to 15 to 25% and leads to long-term increase in recovery. Furthermore, results of permeability measurements defined the possible use of proppants surface modification depending on the coating type for different applications in oil recovery.

V. ACKNOWLEDGMENT

Author would like to express gratitude to Lyubov Magadova, Vladimir Gubanov and Alexei Viktorov and entire staff of Oilfield Chemistry Department at Gubkin University for their support during the experiments in the laboratory.

VI. REFERENCES

- [1] G.C. Howard and C.R. Fast, "Hydraulic fracturing: core issues and trends," in Proc. SPE AIME New York, 1970
- [2] F. Liang and M. Sayed and G.Al-Muntasheri and F. Chang, "Overview of existing proppant technologies and challenges," in Proc. SPE Manama, 2015
- [3] P.D. Nguyen and J.D. Weaver, "Chemical hooks keep proppant" in Oil and Gas Journal, vol. 95, 1997
- [4] Z. Jingchen, "Theoretical conductivity analysis of surface modification agent treated proppant" in Fuel, vol. 134, pp 166-170, 2013
- [5] D. Maley, J. Boyer, B. O'Neil, K. Zhang, "Surface modification of proppant to improve transport and placements," Trican Well Service LTD, Tech. Rep., 2014
- [6] V. Mozzerin, "Proppant (BKO)," RF Patent 2180397, 2002.
- [7] J. Russell, "Composition and method for making a proppant," U.S. Patent 7491444, 2011
- [8] S. Pliner, "Procedure for preparing propping agent with coating and propping agent," RF Patent 65238157, 2013.
- [9] M. Vincent, "Coating and/or treating hydraulic fracturing proppants to improve wettability, proppant lubrication, and/or to reduce damage by fracturing fluids and reservoir fluids," U.S. Patent 20050244641, 2005
- [10] S. Pliner, "Method of making a proppant with coating," RF Patent 243582, 2009.
- [11] J. N. Israelachvili, "Intermolecular and surface forces," 1st ed., . London: Academic Press, 1985.
- [12] L. K. Koopal, "Surfactant adsorption and surface solubilization," ACS Series 615l, vol. 78, pp. 78, 1995.
- [13] K. Li and R.N. Horne, "Characterization of spontaneous water imbibition into gas-saturated rock," in Proc. SPE Stanford, 2000
- [14] M. Raposo, "A guide for atomic force microscopy analysis of solid condensed matter", Modern research and educational topics in microscopy, 2007
- [15] C.W. Extrand, S.I. Moon, "Indirect methods to measure wetting and contact angles on spherical convex and concave surfaces" in Langmuir, ACS. vol. 28 (20), pp 7775-7779, 2012
- [16] C.W. Extrand, S.I. Moon, "Contact angles on spherical surfaces" in Langmuir ACS, vol. 24 (17) , pp 9470-9473, 2008

Investigation of Flooding/Drought Phenomena in 1kW Proton Exchange Membrane Fuel Cell

Aleksandra Sveshnikova*, Gioele Di Marcoberardino, Alexander Ustinov, Aldo Bischi

Abstract - Many scientific works related to fuel cell technology are dedicated to the problem of flooding in proton exchange membrane fuel cells (PEMFC). This problem depends on many different factors such as the improvement of catalysts systems, membrane-electrode assembly (MEA) and design of fuel cell channels. At the same time, flooding phenomena at a system level has not received enough attention. In this research, an external humidification system for the PEMFC was designed and tested. Polarization curve of 1 kW PEMFC in the range of 0-120 A was built according to experimental results carried out at the Laboratory of Micro-Cogeneration at Politecnico di Milano. The influence of inlet air absolute humidity on fuel cell performance was investigated at different current densities. It was observed, that at low current densities fuel cell stack, particularly the last cell is more sensitive to flooding. With growing current density and airflow rate, flooding is eliminated and turned into the problem of drought. In order to keep the performance of fuel cell at high level, absolute humidity of incoming air should be increased with respect to the current density.

Index Terms - Absolute humidity; Degradation; Flooding; Operating conditions; PEM fuel cell; Polarization curve; Relative Humidity; Water management.

I. NOMENCLATURE

Parameters

E_{eq}	[V]	Equilibrium potential
E_{act}	[V]	Activation losses
E_{con}	[V]	Concentration losses
E_{ohm}	[V]	Ohmic losses
Q	[ml/cell/A/min]	Reactant flow
P	[bar]	Pressure
T	[C]	Temperature
RH	[%]	Relative humidity
u	[l/min]	Volumetric flow rate
I	[A]	Current
i	[mA/cm ²]	Current density

A. Sveshnikova is a PhD student at the Center of Energy Systems, Skolkovo Institute of Science and Technology, Skolkovo Innovation Center, Building 3, Moscow 143026, Russia [e-mail: Aleksandra.sveshnikova@skolkovotech.ru]

G. Marcoberardino is a Postdoc at the Laboratory of Micro-CHP plants, Politecnico di Milano, Via Lambruschini 4c building 26/a, Milano, 20156, Italy

A.Ustinov is a professor at the Center of Energy Systems, Skolkovo Institute of Science and Technology, Skolkovo Innovation Center, Building 3, Moscow 143026, Russia

A.Bischi is a professor at the Center of Energy Systems, Skolkovo Institute of Science and Technology, Skolkovo Innovation Center, Building 3, Moscow 143026, Russia

Experimental data of this paper were obtained in Politecnico di Milano at the laboratory of Micro-CHP plants led by prof. Stefano Campanari. This work was also supported by CRDF Global foundation, which provided the grant to present the project on a scientific conference "Energy Storage - 2017. Next Generation" on 13-15 February 2017 in San Francisco, USA.

F	[C/mol/K]	Faraday number
$J_{H_2O,drag}$	[mol/s*cm ²]	Water transferred by electroosmotic drag
$J_{H_2O,diff}$	[mol/s*cm ²]	Water transferred by diffusion
ρ_m	[g/cm ³]	Density of dry membrane
M_m	[-]	Equivalent weight of membrane material
t_m	[mm]	Thickness of the membrane
λ_m	[-]	Membrane water content
n_{drag}	[-]	Drag coefficient
D_w	[-]	Water diffusivity
n	[-]	Number of electrons in the reaction
C	[-]	Concentration in mole fraction
λ	[-]	Stoichiometric coefficient

Subscripts

PEM	Proton Exchange Membrane
FC	Fuel Cell
RH	Relative Humidity
HE	Heat Exchanger
MEA	Membrane-electrode assembly

II. INTRODUCTION

PEM fuel cell technology has been actively developing especially for stationary power supply applications. Such countries as the USA, Canada, Japan, Germany, Italy and South Korea have already found industrial implementation for the PEM fuel cells and have developed commercially available products [1].

Russia occupies the 9th place among countries with venture capital investment in the fuel cell technology with \$21 million in the last 15 years [2]. Skolkovo Institute of Science and Technology is working on design of autonomous energy system based on PEMFC, which could be used in isolated residential areas as a back-up power supply [3], [4]. This project is focused on fuel cell characteristics specific for conditions of Far North regions of Russia. The most critical problem is humidity control of inlet air which is especially dry at subzero temperatures and needs to be well humidified before entering the system.

Polarization curve is the key characteristic of a fuel cell, and it shows the dependency of generated voltage on current density applied through the electric load (see Fig.1). Theoretical maximum for the PEM fuel cell is 1.23 V based on Nernst equation calculation but in reality, it is not possible to achieve this value due to multiple types of irreversible voltage losses occurring in the process [5].

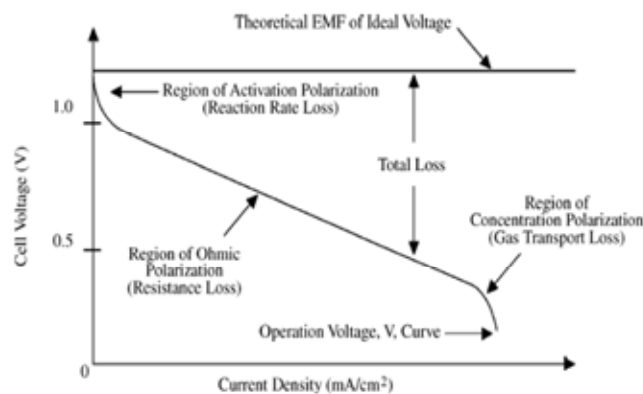


Fig. 1. Typical FC polarization curve [2]

Voltage generated by a single cell can be calculated with the following equation [6]:

$$E_{cell} = E_{eq} - E_{act} - E_{con} - E_{ohm} \quad (1)$$

E_{eq} - Equilibrium potential of electrochemical cell, V;

E_{act} - Activation losses, caused by slow reaction kinetics, especially pronounced at low current densities, V;

E_{con} - Concentration losses, caused by mass transport limitations, especially pronounced at high current densities, V;

E_{ohm} - Ohmic losses, caused by charge transport limitations and thus, proportional to current density, V.

Usually, activation losses do not change with operational conditions and can be eliminated through the catalyst modification. Therefore, such type of losses will not be considered in this research. Concentration losses can be clearly seen when fuel cell is exposed to drought, and the airflow is so strong that there is not enough time for full humidification and electrochemical reaction. This type of voltage losses is important for this research and will be investigated at high current densities. Ohmic losses are the most sensitive to operational conditions of the fuel cell especially to the temperature in the humidifier. This temperature determines absolute humidity of inlet air, and the influence of this temperature will be discussed in this paper.

Polymeric membrane used as an electrolyte material in the PEM fuel cells is very sensitive to humidity rate of inlet air. Its proton conductivity depends on the amount of water vapor coming with the air. In case of insufficient humidity rate, FC will experience charge transport limitations which will increase Ohmic losses. At the same time, excess water coming with the air might condensate inside the cell and block active catalyst centers causing rapid voltage drop. Therefore, correct operational conditions are very important to avoid drought/flooding phenomena.

Two different transport phenomena are taken into account in the PEMFC stack model. The electro-osmotic drag, due to the dragging of water molecules with protons from the anode towards the cathode, and the back-diffusion (from the cathode towards anode), due to the high water concentration gradients across the membrane [7]:

$$J_{H_2O} = J_{H_2O,diff} - J_{H_2O,drag} \quad (2)$$

Water transport caused by diffusion depends on membrane characteristics and temperature. Thus, at certain temperature it can be considered as a constant. When this factor dominates, water is accumulated on anode side:

$$J_{H_2O,diff} = \frac{\rho_m \lambda_m}{M_m t_m} D_w \quad (3)$$

ρ_m - Density of dry membrane, g/cm³;

M_m - Equivalent weight of membrane material;

t_m - Thickness of the membrane, mm;

λ_m - Membrane water content;

D_w - Water diffusivity;

Water transport caused by osmotic drag depends on current density, thus, at higher currents $J_{H_2O, drag}$ dominates and water accumulates on cathode side:

$$J_{H_2O,drag} = 2n_{drag} \frac{i}{nF} \quad (4)$$

n_{drag} - Drag coefficient;

n - Number of electrons;

F - Faraday's number, 96485 C/mol/K;

i - Current density, mA/cm²;

It is important to keep the balance between these two factors, so anode stays humidified and cathode avoids flooding.

The test performed at this research was held at the range of 0-600 mA/cm². As it can be observed from the Fig.2 at this range, diffusion is the dominated water transport phenomena. Thus, it is expected that most of water will be accumulated on cathode side, however it will be interesting to see if proportion of water accumulated on anode side increases with current density.

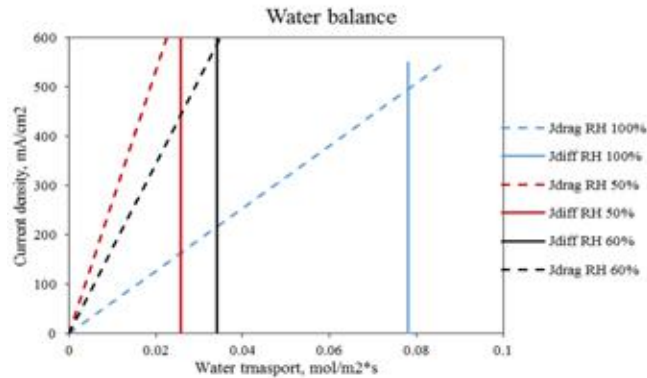


Fig. 2. Change of water transport with current density

Usually the last cell in the stack is the most sensitive to flooding. Water produced in all previous cells is pushed out to the outlet and in case of low flow rates, this water can flood the last cell (Fig.3). This problem can be eliminated by increased air access (air stoichiometry).

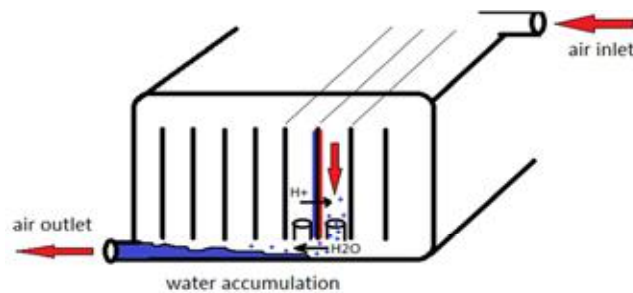


Fig. 3. Schematic representation of accumulated water on the outlet of FC

III. EXPERIMENTAL PART

On the Fig.4 one can observe a typical behavior of the last cell. Step by step the load is increased and at some point (19:26; 30A), voltage rapidly goes down due to the flooding. Such problem can occur at any load if humid starts to condensate inside the stack before leaving it.



Fig. 4. Typical behavior of the last cell in case of flooding

A. Experimental Set Up

Technological scheme of experimental set-up can be seen on Fig.5. In this experiment 1kW fuel cell stack (© Power Cell) with water cooling loop was used for testing. It consists of 10 cells of 200 cm² active surface area each. FC stack is connected to DC load, which can be supplied with both current and voltage input. The device has 3 inlets and 3 outlets for hydrogen, air and cooling media. Each circuit is discussed in more details below.

1) Water coolant circuit:

Electric efficiency of fuel cell is approximately 50%. It means that among 1kW of electric power additional 1kW of heat is produced during operation. Operational temperature of the system is 60-80°C. Constantly produced heat can increase the temperature of the stack above operational limit due to the exothermic reaction. Thus, cooling circuit is required. The FC is designed for liquid coolant, thus we can use water as a cooling media.

In order to control inlet water temperature, a water bath with 30°C minimum temperature is used. For a shut-down procedure to cool down the system faster, water circuit is connected to the lab hydraulic system via heat exchanger (HE). It is important to mention, that water for cooling purposes has to be deionized to avoid salvation of the system. The maximum limit for water conductivity is 20 µS/cm. Water used in the test has conductivity of 3-6 µS/cm.

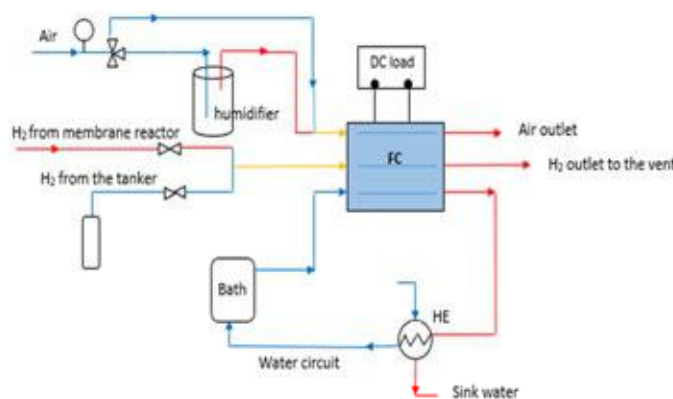


Fig. 5. PEM fuel cell system developed in the lab

2) Air circuit:

Air coming to the FC has to be humidified in order to reach good proton conductivity of the membrane. Thus, air channel is connected to a water tank, which is constantly heated and insulated. Airflow is humidified and heated due to bubbling through the hot water. After the humidifier, air passes heating line where temperature is 2-3 degrees higher than inside humidifier. This is necessary to avoid any water condensation before entering the FC. Moreover, during the start-up procedure when PEMFC temperature is below operational, air should be dry in order to avoid water condensation inside FC. Thus, a triple valve is used to switch from dry air line to humidified air line before supplying the load.

3) Hydrogen circuit:

Hydrogen used in this test comes from high-pressure vessel and its concentration is close to 100%. During the start-up and shut down procedures nitrogen gas is used to remove any contaminations from reaction zone. When the system is ready to be connected to the load, nitrogen is switched to hydrogen. After the FC stack, unreacted hydrogen and water are purged to the ventilation system.

B. Operating conditions and assumptions

Fuel cell operation was characterized at the range of 0-120A load with 10A steps. Experiment was performed at 70 °C and 1.25 bar. These parameters were kept constant at all load levels. Temperature of the humidifying system was set according to the load starting from 50 °C at 10A and ending with 70°C at 120A.

Air coming to the system has to be in excess to the hydrogen. Using FC manual recommendations, reactant flow rates for all load steps were calculated (Fig. 6).

At low current between 0-10A, air excess should be higher to avoid water condensation. Starting from 10A, reactants' flow rates increase with current.

Though electric load has enough capability to work at higher currents, there is a limit for mass flow controller on hydrogen line. Thus, characterization of PEMFC was performed in the range of 0-120A as it can be seen from the Fig. 6.

Reactant flow rates:

Using FC manual, reactant flow rates can be calculated with the following formula:

$$v = \frac{Q * n * \lambda * I}{C * 1000} \quad [5]$$

Q - Reactant flow, ml/cell/A/min;

λ - Stoichiometric flow rate;

I - Current, A;

C - Concentration in mole fraction.

Data used for the experiment:

$\lambda_{H_2} = 1.5$ $\lambda_{air} = 2.5$

$Q_{H_2} = 7.0$ standard* Nml/cell/A/min

$Q_{air} = 16.6$ standard* Nml/cell/A/min

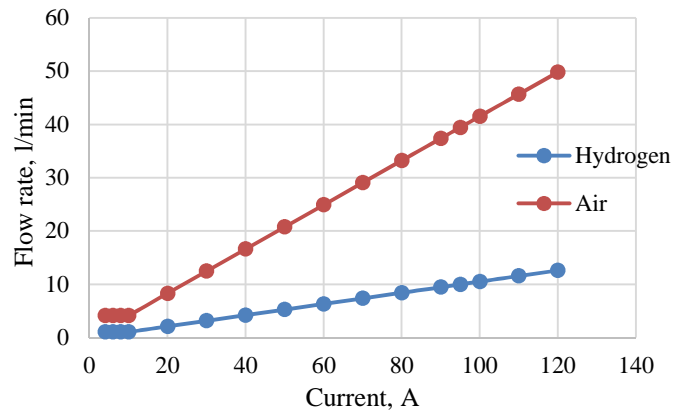


Fig. 6. Reactants' flow rates used in the experiment

During the experiment, the following assumptions were made:

- Ambient T=20 °C;
- Air that comes from external hydraulic circuit of the lab is completely dry and contaminates 21% of oxygen;
- Air after bubbling through the heated water tank is fully humidified and reaches 100% RH at all load levels;
- Pressure inside humidifier is equal to the inlet air pressure (1.25 bar);
- Temperature of the water inside humidifier is equal to temperature of vessel material, which is measured by thermometer in real time.

C. Results

After several experiments, polarization curve at 70 °C and 1.25 bar operational conditions was obtained. One can observe all three zones of voltage losses: activation losses are pronounced at the current below 20A, ohmic losses with linear behavior can be observed between 20 and 100A and concentration losses at the current above 100A (Fig.7).

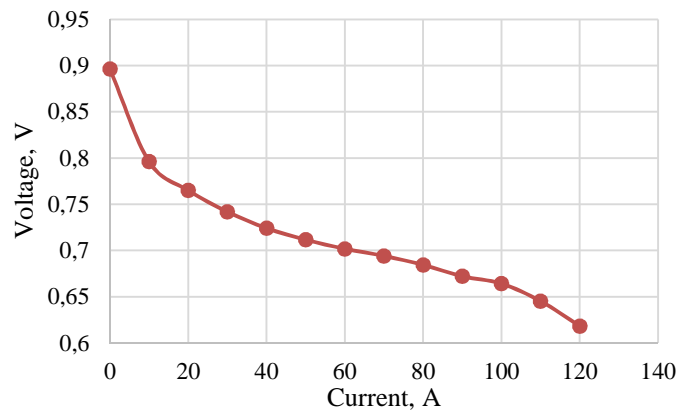


Fig. 7. Polarization curve of PEMFC at 70°C and 1.2 bar

This curve represents average value of 8 cells, which are less sensitive to humidity rate (Cells 2-9). First and last cells were excluded from there, as their behavior was deviated from others. Maximum power achieved at 120A was 742 W.

Temperature of humidifier determines absolute humidity of inlet air. It became clear from the experiment that FC performance at 120A is very sensitive to temperature of the water in the humidifier and thus, to the absolute humidity of inlet air. On the Fig.8, one can observe how cell voltage changes at the temperatures between 53 and 63 °C at the 120A load.

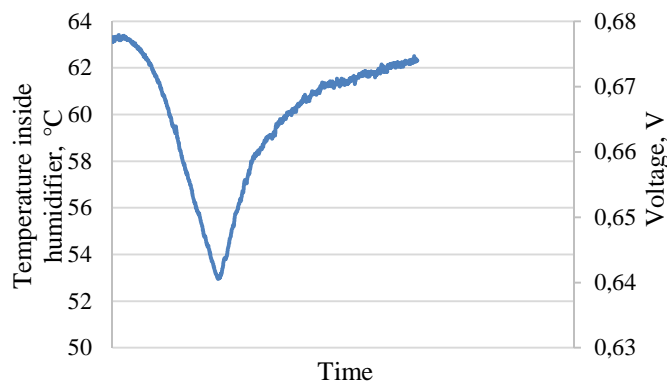


Fig. 8. Cell voltage dependency on temperature in humidifier

The same tendency was discovered at different loads (20, 40, 60, 80, 100A). With increasing absolute humidity of inlet air, the average cell voltage is growing.

Last cell is the most sensitive to any changes in humidity rate. Thus, voltage of the last cell can be considered as a detector of flooding/drought phenomena. Flooding phenomena causes sharp voltage drop of the last cell, which is hard to recover, while drought phenomena slowly decreases the cell voltage and does not have such crucial consequences.

With load, amount of water produced in fuel cell is growing thus increasing the risk of flooding. However, airflow is growing too, purging accumulated water out of the stack. It turned out that at the current range of 0-30 A the risk of flooding is much higher because airflow is not strong enough to purge accumulated water, no matter how low is the inlet air absolute humidity. Experimental results showed that to keep good performance temperature in humidifier should grow together with the load. At every load there is humidification temperature at which cell voltage reaches its maximum. These temperatures were obtained experimentally and can be seen in Table I.

Table I. Proposed humidification temperatures for different loads

FC load, A	Temperature in humidifier, °C
10	52
20	54
40	58
60	62
80	66
100	70
120	74

IV. CONCLUSIONS

In this paper, the influence of absolute humidity of inlet air on flooding/drought phenomena on PEM fuel cell was investigated. It was estimated by means of temperature in the air humidifier, assuming 100% relative humidity of air after humidification. It turned out that PEM fuel cell is very sensitive to the temperature of the humidifier and this sensitivity is growing with current density. At maximum allowed load, (120A) change of T from 53 to 63 °C increased the average cell performance from 0.640V to 0.675V. Similar tendency was observed at lower currents, though the influence of temperature is eliminated. For each load, a certain humidification temperature was proposed considering best cell performance. The most sensitive cell for flooding is the last cell, and its behavior can be considered as the detector. All operational conditions should be tuned based on last cell performance.

V. ACKNOWLEDGMENT

The authors gratefully acknowledge the contributions of C. Pirrone and S. Foresti and their technical support during experiments.

VI. REFERENCES

- [1] Elmer T., Worall M., Wu S., Riffat S.B. Fuel cell technology for domestic built environment applications: State of-the-art review. *J. Renew. Sustain. Energy Rev.* 2015; 42: 913–931.
- [2] Curtin S., Gandi J. Fuel Cell Technologies Market Report 2015. U.S. Department of Energy, 2015
- [3] Ustinov A., Sveshnikova A., Abrosimov K., Khayrullina A. 12 (2016, July) Effect Of Inlet Air Temperature And Relative Humidity On Performance Of PEM Fuel Cell (Presented on 12th International Scientific Conference HEFAT 2016)
- [4] Ustinov A., Khayrullina A., Borzenko V., Khmelik M., Sveshnikova A. Development method of Hybrid Energy Storage System, including PEM fuel cell and a battery. *Journal of Physics: Conference Series*, 2016, Volume 745, Technical sessions
- [5] O'Hayre R., Cha S-W. *Fuel Cell Fundamentals*. Wiley, 2016, pp. 235-238
- [6] Zhang, J. *PEM Fuel Cell Electrocatalysts and Catalyst Layers*. Springer, 2011
- [7] *PEM Fuel Cell Dynamic Modeling*. Lecture materials by prof. Stefano Campanari, 2015
- [8] Berdin V., UNO Initiative "Sustainable Energy for everyone" [in Russian]
- [9] Pilatowsky, F.I. *Cogeneration fuel cell-sorption air conditioning systems*. London: Springer, 2011, p.2

Overview of Microgrid Control

Vasily G. Chirkin

Abstract - Implementation of renewable energy sources cause difficulties for control of power systems. The microgrid concept is intended to overcome these challenges. This paper represents an overview of microgrid control techniques in order to highlight their advantages and disadvantages. Hierarchical control consisting of primary, secondary and tertiary control is represented. The main control architectures and principles, such as droop control, multi-agent systems, are indicated.

Index Terms - Control, microgrid, smart grid

I. NOMENCLATURE

f	frequency (Hz)
P	real power (W)
Q	reactive power (VAr)
R	resistance (Ohm)
V	voltage (V)
X	reactance (Ohm)

DER	Distributed Energy Resources
DG	Distributed Generation
ESS	Energy Storage System
MAS	Multi-Agent System
PCC	Point of Common Coupling
RES	Renewable Energy Sources

II. INTRODUCTION

A need for greener and sustainable power generation technologies led to a growing penetration of Renewable Energy Resources (RES) based on hydro, solar, wind and hydrogen energy. Apart from environmental and economic benefits, integration of Distributed Energy Resources (DER) in distribution grid reduces its stability and brings additional issues in its control.

The most relevant technical challenges of renewable DERs integration to be overcome in order to retain reliability level and completely utilize their benefits are [1]:

- Proper dispatch and unit commitment under supply and demand uncertainty.
- Economically effective and reliable operation of volatile power generation.
- Development of Demand Side Management schemes.
- Upgrade of protection schemes to account bidirectional power flows.
- Development of new voltage and frequency control methods of inverter-based microgrids.
- Development of market models and control mechanisms that will allow using intermittent energy sources as a reliable-supply bulk power system.

Vasily G. Chirkin is with the Center for Energy Systems, Skolkovo Institute of Science and Technology, Skolkovo Innovation Center, Building 3, Moscow 143026, Russia (e-mail: vasily.chirkin@skolkovotech.ru).

The concept of microgrid is aimed to overcome these challenges. Although the exact microgrid definition is still under discussion, there are a few features that characterize it. The U.S. Department of Energy defines microgrid as “a group of interconnected loads and distributed energy resources with clearly defined electrical boundaries that acts as a single controllable entity with respect to the grid and can connect and disconnect from the grid to enable it to operate in both grid-connected or island modes” [2]. Therefore, these features are: clearly defined electrical boundaries, a controller to control and operate DER and loads as unity, and capability of operating in grid-connected or island mode and switch between them.

III. CONTROL OF MICROGRIDS

Integration of DER introduces a number of challenges to be resolved in the design of control and protection schemes. Some of them originate from assumptions done for conventional distribution systems. The others take place at conventional transmission system level and lead to stability issues. The named issues mostly are:

- DG installed at low voltage level results in bidirectional power flow and complication of protection coordination and voltage control.
- The droop gains of each microgrid interface need to be designed carefully. Strong interaction between DG units or low damping magnitude of DGs could lead to small-signal frequency instabilities [3].
- In conventional power system models predominance of three-phase balanced conditions, inductive transmission lines, and constant-power loads are often assumed, which is not always valid for microgrids [4].
- Inverter-based microgrids are characterized by low inertia, which may result in large frequency deviations in island mode [5].

Coordination of different DER under uncertainties such as load profile and weather forecast becomes more challenging due to less number of loads and energy resources.

The microgrid's control system must overcome the mentioned challenges to ensure safe and economical operation.

Availability of measurements, communication, and high-performance computational equipment are required for the microgrid control. Utilization of a hierarchical control appears to be winning solution due to separation of fast-dynamic output control and slower-dynamic economic dispatch. The hierarchical structure usually consists of three following levels. Primary control stabilizes frequency and voltage using droop controllers, secondary control counterbalance the deviations in voltage and frequency, and tertiary control determines power flows for the optimal operation [6].

The microgrid behavior can be affected mainly by means of such parameters as voltage, frequency, and active and reactive power. The frequency and the voltage at point of common coupling (PCC) are dominated by the main grid. In this case, the microgrid control purpose is to adapt the active and reactive power of DER to the load demand. Reactive power injection can be used for power factor correction, reactive power supply, or voltage control.

The island mode is more challenging because it is more sensible to power balance and requires accurate power sharing mechanism. Voltage and frequency have to be controlled by microgrid's DERs only once the main grid does not support them anymore. The main microgrid control objective is to achieve power balance. A small inconsistency in the magnitude, phase angle or frequency of the voltage signal can lead to large circulating currents. The number of different control schemes were proposed to overcome this issue [7]-[9] One possible solution is to have one inverter to operate as a master unit, while others are slave [10]. The master unit can perform open-loop frequency control. This unit can be operated similar to a synchronous generator with a reactive power-voltage droop characteristic, while the others support active and reactive power as dictated by the secondary control [11].

Energy storage systems (ESS) are essential for microgrid reliability. DG can either be dispatchable or nondispatchable. Nondispatchable units are mainly renewable DG, typically solar and wind, producing a volatile and intermittent output power. ESS can be combined with nondispatchable DER to be used as dispatchable units. The primary application of ESS is to coordinate with DG to guarantee the microgrid generation adequacy. They can also be used for energy arbitrage, accumulating the energy during low-price hours and supply the microgrid when the market price is high. The ESS also plays a major role in microgrid islanding mode [12].

Energy storage applications in microgrid are power quality enhancement, frequency regulation, islanded operation, active distribution system, and electric vehicle technologies [13]-[14].

IV. CONTROL HIERARCHY IN MICROGRIDS

Two common control architectures for microgrids are centralized and decentralized. In centralized approach, a microgrid is fully controlled by a centralized controller. The latter communicates with controlled units and carries out all necessary calculations of control outputs. On the contrary, in decentralized control, each unit is controlled by local controller, based on local information [15]. Whereas the centralized control provides high disturbance rejection level it also requires much of communication. Decentralized control can reduce the number of communication messages between units and ease the optimization procedure by solving it locally.

In order to combine advantages of both architectures a hierarchical control scheme is used. It consists of three levels: primary, secondary and tertiary. These levels are different in their timeframe and response speed. Hierarchical control scheme is shown in Fig. 1.

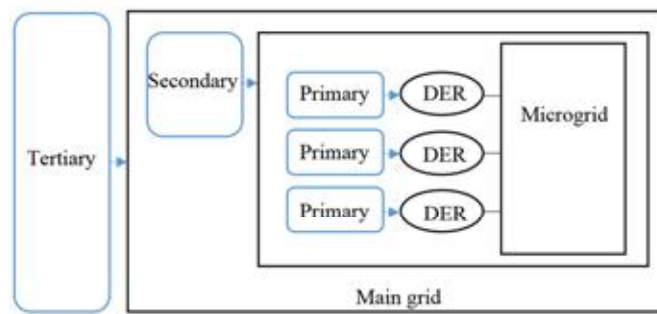


Fig. 1. Hierarchical control scheme. Primary, secondary and tertiary control.

A. Primary control

Primary control is local or internal control. It provides the first and the fastest response (millisecond time frame). It is based on the local measurements. In synchronous generators, power control and sharing are performed via governor, automatic voltage regulator and machine's inertia.

Inverter-based DG have low inertia and require special design to simulate the inertia of synchronous generators and perform frequency regulation. Inverter output controllers regulate output and currents, whereas power sharing controllers perform active and reactive power control by using active P/f and Q/V droop control [16]-[17].

The inverter output control typically consists of an outer loop for voltage regulation, and an inner loop for current control [18]. A review of inverter output control is presented in [19]. Multivariable control method improving dynamic response of microgrids was proposed in [20].

Power sharing control often relies on droop-based method [21]. Relationship between real power and frequency, and reactive power and voltage is expressed in (1) and (2). Active power is proportional to frequency deviation from nominal value, while reactive power is proportional to voltage deviation.

$$f_0 - f_1 = -K_P(P_0 - P_1) \quad (1)$$

$$V_0 - V_1 = -K_Q(Q_0 - Q_1), \quad (2)$$

where f , V , P , and Q are, respectively, frequencies, voltages, active and reactive powers, indices 0 and 1 stay for nominal and reference values, K_P and K_Q are droop coefficients.

Droop coefficients calculations are based on steady-state performance criteria [22]. Special attention should be paid to stability margins [4].

The main advantage of droop control is that it is based on local measurements and does not need communication. Nevertheless, it has some disadvantages, such as poor transient performance, poor performance in distribution networks due to low X/R ratio, inaccurate power sharing, and variable frequency depending on load conditions [23].

Reference [24] reported results of eigenvalue analysis of linearized microgrid model. The analysis showed slower oscillatory modes, associated with droop controller loops. Damping factors of these modes increases while the active power output of DG unit increasing. Modified droop control methods were proposed to overcome this disadvantage, such as frequency restoration loop [25], a virtual output resistance [22], virtual inductive output impedance [26], and adaptive droop [24].

B. Secondary control

Secondary control is responsible for reliable and economical operation of microgrids. Control task is to find optimal dispatch and provide control signals for fast-variable DG sources in order to restore voltage and frequency deviations produced by primary control. Secondary control is performed at lower time frame (second or sub second).

Secondary control architecture can also be divided to centralized and decentralized. Input parameter for secondary control are forecasted power output and load, ESS state of charge, operational limits, security constraints, forecasted energy prices. Output variables are reference values of output powers and voltage for each DER and load.

Optimal dispatch problem can be solved offline and stored in look-up table to be used in real time [27]. Some techniques use genetic algorithms [28] and ant colony optimization methods [29].

Decentralized secondary control uses multi-agent system (MAS) methods. MAS system consists of a number of intelligent agents, which communicate with each other in order to get global and local goals. Agent is computer system that is that is capable of autonomous actions. Although agents can communicate large portion of control is performed locally [30]. In this case, consumers, generators, ESS and the main grid send buying and selling bids to the central controller, which are calculated locally according to their needs, cost function, constraints and forecasts. The central controller makes decision to maximize social welfare and dispatch feasibility or verify compliment with grid standards [31]. Additional agents were proposed in [32] that allow demand side response.

C. Tertiary control

Tertiary control is the top level of microgrid control. Its goal is to obtain optimal set points for proper coordination and reactive power management, based on total losses minimization approach. Time scale of tertiary control is a few minutes [6].

V. CONCLUSIONS

The integration of renewable energy sources requires the development of reliable technics and solutions. Microgrids provide benefits of RES utilization in power system and intended to overcome the challenges associated to it. In this paper, an overview of most common microgrid control methods was performed, hierarchical approach was described, challenges for control of microgrids were discussed.

Electrical energy storage systems is essential technology for DG integration into microgrids due to intermittent nature of RES. Management of volatile power sources is the main challenge of microgrids control. Apart from generation uncertainties the other challenges are unbalanced network state, low inertia of inverter-based DG, and low X/R ratio of distribution lines at low voltage level, causing coupling of active and reactive power. Different control methods have been proposed in the literature to solve these challenges. The issue of robustness and stability of them, however, remains. Besides, it is important to demonstrate effectiveness of them in microgrid test beds before application in real power systems.

VI. REFERENCES

- [1] P. D. F. Ferreira, P. M. S. Carvalho, L. A. F. M. Ferreira and M. D. Ilic, "Distributed Energy Resources Integration Challenges in Low-Voltage Networks: Voltage Control Limitations and Risk of Cascading," in IEEE Transactions on Sustainable Energy, vol. 4, no. 1, pp. 82-88, Jan. 2013.
- [2] Department of Energy Office of Electricity Delivery and Energy Reliability. (2012). Summary Report: 2012 DOE Microgrid Workshop. [Online]. Available: <http://energy.gov/sites/profiles/2012%20Microgrid%20Workshop%20Report%2009102012.pdf>, accessed Feb. 13, 2017.
- [3] M. H. Nazari, M. Ilic, and J. P. Lopes, "Small-signal stability and decentralized control design for electric energy systems with a large penetration of distributed generators," in Control Eng. Pract., vol. 20, no. 9, pp. 823-831, 2012.
- [4] P. Vorobev, P.-H. Huang, M. Al Hosani, J. L. Kirtley, and K. Turitsyn, "A framework for development of universal rules for microgrids stability and control," submitted to CDC 2017.

- [5] N. Pogaku, M. Prodanovic and T. C. Green, "Modeling, Analysis and Testing of Autonomous Operation of an Inverter-Based Microgrid," in *IEEE Transactions on Power Electronics*, vol. 22, no. 2, pp. 613–625, March 2007.
- [6] A. Bidram and A. Davoudi, "Hierarchical structure of microgrids control system," in *IEEE Trans. Smart Grid*, vol. 3, no. 4, pp. 1963–1976, Dec. 2012.
- [7] G. Willmann, D. F. Coutinho, L. F. A. Pereira, and F. B. Libano, "Multiple-loop control design for uninterruptible power supplies," in *IEEE Trans. Ind. Electron.*, vol. 54, no. 3, pp. 1591–1602, Jun. 2007.
- [8] K.-S. Low and R. Cao, "Model predictive control of parallel-connected inverters for uninterruptible power supplies," in *IEEE Trans. Ind. Electron.*, vol. 55, no. 8, pp. 2884–2893, Aug. 2008.
- [9] A. Nasiri, "Digital control of three-phase series-parallel uninterruptible power supply systems," in *IEEE Trans. Power Electron.*, vol. 22, no. 4, pp. 1116–1127, Jul. 2007.
- [10] J. A. P. Lopes, C. L. Moreira, and A. G. Madureira, "Defining control strategies for microgrids islanded operation," in *IEEE Trans. Power Syst.*, vol. 21, no. 2, pp. 916–924, May 2006.
- [11] N. Hatzigiorgiou "Microgrids: Architectures and Control" Wiley-IEEE Press, 2014.
- [12] R. M. Kamel, A. Chaouachi, and K. Nagasaka, "RETRACTED: Wind power smoothing using fuzzy logic pitch controller and energy capacitor system for improvement micro-grid performance in islanding mode," in *Energy*, vol. 35, no. 5, pp. 2119–2129, 2010.
- [13] A. Nourai and D. Kearns, "Batteries included: Realizing smart grid goals with intelligent energy storage," *IEEE Power Energy Mag.*, vol. 8, no. 2, pp. 49–54, Mar./Apr. 2010.
- [14] H. Zhou, T. Bhattacharya, D. Tran, T. S. T. Siew, and A. M. Khambadkone, "Composite energy storage system involving battery and ultracapacitor with dynamic energy management in microgrid applications," in *IEEE Trans. Power Electron.*, vol. 26, no. 3, pp. 923–930, Mar. 2011.
- [15] R. H. Lasseter, "Smart distribution: Coupled microgrids," *Proc. IEEE*, vol. 99, no. 6, pp. 1074–1082, Jun. 2011.
- [16] P. P. Varaiya, F. F. Wu, and J. W. Bialek, "Smart operation of smart grid: Risk-limiting dispatch," *Proc. IEEE*, vol. 99, no. 1, pp. 40–57, Jan. 2011.
- [17] W. Cox and T. Considine, "Structured energy: Microgrids and autonomous transactive operation," in *Proc. IEEE PES Innovative Smart Grid Technol. Conf. (ISGT)*, Feb. 2013, pp. 1–6.
- [18] H. Qi, X. Wang, L. M. Tolbert, F. Li, F. Z. Peng, P. Nin, M. Amin, "A resilient real-time system design for a secure and reconfigurable power grid," in *IEEE Trans. Smart Grid*, vol. 2, no. 4, pp. 770–781, Dec. 2011.
- [19] Y. Ito, Y. Zhongqing, and H. Akagi, "DC microgrid based distribution power generation system," in *Proc. 4th Int. Power Electron. Motion Control Conf. (IPEMC)*, vol. 3, Aug. 2004, pp. 1740–1745.
- [20] F. Wang, J. L. Duarte, and M. A. M. Hendrix, "Grid-interfacing converter systems with enhanced voltage quality for microgrid application Concept and implementation," in *IEEE Trans. Power Electron.*, vol. 26, no. 12, pp. 3501–3513, Dec. 2011.
- [21] Lasseter, B. "Microgrids Distributed Power Generation", in *IEEE Power Engineering Society Winter Meeting Conference Proceedings*, Columbus, Ohio, vol. 1, pp. 146–149., 2001.
- [22] F. Katiraei and M. R. Iravani, "Power management strategies for a microgrid with multiple distributed generation units," in *IEEE Trans. Power Syst.*, vol. 21, no. 4, pp. 1821–1831, Nov. 2006.
- [23] J. M. Guerrero, J. C. Vasquez, J. Matas, L. G. de Vicuña, and M. Castilla, "Hierarchical control of droop-controlled AC and DC microgrids — A general approach towards standardization," in *IEEE Trans. Ind. Electron.*, vol. 58, no. 1, pp. 158–172, Jan. 2011.
- [24] Y. Mohamed and E. F. El-Saadany, "Adaptive decentralized droop controller to preserve power sharing stability of paralleled inverters in distributed generation microgrids," *IEEE Trans. Power Electron.*, vol. 23, no. 6, pp. 2806–2816, Nov. 2008.
- [25] J. M. Guerrero, J. Matas, L. G. de Vicuña, M. Castilla, and J. Miret, "Decentralized control for parallel operation of distributed generation inverters using resistive output impedance," in *IEEE Trans. Ind. Electron.*, vol. 54, no. 2, pp. 994–1004, Apr. 2007.
- [26] Y. W. Li and C.-N. Kao, "An accurate power control strategy for power-electronics-interfaced distributed generation units operating in a low-voltage multibus microgrid," in *IEEE Trans. Power Electron.*, vol. 24, no. 12, pp. 2977–2988, Dec. 2009.
- [27] C. Hernandez-Aramburo, T. Green, and N. Mugniot, "Fuel consumption minimization of a microgrid," *IEEE Trans. Ind. Appl.*, vol. 41, no. 3, pp. 673–681, May-Jun. 2005.
- [28] S. Conti, R. Nicolosi, and S. Rizzo, "Optimal dispatching of distributed generators in an MV autonomous micro-grid to minimize operating costs and emissions," in *Proc. IEEE Internat. Symp. on Industrial Electron. (ISIE)*, Jul. 2010, pp. 2542–2547.
- [29] C. Colson, M. Nehrir, and C. Wang, "Ant colony optimization for microgrid multi-objective power management," in *Proc. IEEE Power Syst. Conf. and Exposit. (PSC '09)*, Mar. 2009, pp. 1–7.
- [30] A. L. Dimeas and N. D. Hatzigiorgiou, "Operation of a multiagent system for microgrid control," in *IEEE Trans. Power Syst.*, vol. 20, no. 3, pp. 1447–1455, Aug. 2005.
- [31] T. Logenthiran, D. Srinivasan, and D. Wong, "Multi-agent coordination for DER in microgrid," in *Proc. IEEE Internat. Conf. on Sustainable Energy Technolog. (ICSET'08)*, Nov. 2008, pp. 77–82.
- [32] J. Oyarzabal, J. Jimeno, J. Ruela, A. Engler, and C. Hardt, "Agent based micro grid management system," in *Proc. IEEE Internat. Conf. on Future Power Syst.*, Nov. 2005, pp. 6–11.

Thermal Core Logging Technique for Bazhenov Formation Characterization

A.V. Gabova*, E.Y. Popov, E.M. Chekhonin, R.A. Romushkevich, Y.A. Popov

Abstract - The paper describes the results of the application of a new thermal core logging technique developed for the investigation of hydrocarbon fields located in the Bazhenov formation. Continuous non-destructive non-contact profiling of rock thermal conductivity, heterogeneity, and volumetric heat capacity with 1-2 mm spatial resolution was applied to more than 13 000 full-size core samples from 17 wells with subsequent analysis of rock thermal anisotropy. The measurement results provided a unique database of rock thermal properties for the basin, petroleum system, and hydrodynamic modeling. It is shown that approaches developed for the Bazhenov formation allow the transformation of thermal core logging results into continuous high-resolution profiles of the following parameters: total organic carbon, sonic waves velocities, Young's modulus, Poisson's ratio, sonic anisotropy coefficient, density, and natural radioactivity of rocks along the well.

Index Terms - thermal core logging, the Bazhenov formation, thermal properties

I. NOMENCLATURE

λ_{\parallel}	thermal conductivity component parallel to bedding (W/(m·K))
λ_{\perp}	thermal conductivity component perpendicular to bedding (W/(m·K))
β_{\parallel}	thermal inhomogeneity factor parallel to bedding (-)
β_{\perp}	thermal inhomogeneity factor perpendicular to bedding (-)
λ_{\max}	maximum value of thermal conductivity (W/(m·K))
λ_{\min}	minimum value of thermal conductivity (W/(m·K))
λ_{average}	average value of thermal conductivity (W/(m·K))
K	anisotropy coefficient
V_p	P-wave velocity
V_s	S-wave velocity

This work was supported in part by the Ministry of Education and Science of the Russian Federation grant RFMEFI58114X0008.

A. V. Gabova is with the Center of Hydrocarbon Recovery, Skolkovo Institute of Science and Technology, Skolkovo Innovation Center, Building 3, Moscow 143026, Russia (e-mail: a.gabova@skoltech.ru).

E. Y. Popov is with the Center of Hydrocarbon Recovery, Skolkovo Institute of Science and Technology, Skolkovo Innovation Center, Building 3, Moscow 143026, Russia (e-mail: e.popov@skoltech.ru).

E. M. Chekhonin is with the Center of Hydrocarbon Recovery, Skolkovo Institute of Science and Technology, Skolkovo Innovation Center, Building 3, Moscow 143026, Russia (e-mail: e.chekhonin@skoltech.ru).

R. A. Romushkevich is with the Center of Hydrocarbon Recovery, Skolkovo Institute of Science and Technology, Skolkovo Innovation Center, Building 3, Moscow 143026, Russia (e-mail: r.romushkevich@skoltech.ru).

Y. A. Popov is with the Center of Hydrocarbon Recovery, Skolkovo Institute of Science and Technology, Skolkovo Innovation Center, Building 3, Moscow 143026, Russia (e-mail: y.popov@skoltech.ru).

II. INTRODUCTION

The volume and quality of experimental data on rock thermal properties, such as rock thermal conductivity and volumetric heat capacity (VHC) of core samples, can be significantly increased by the development and application of the non-contact optical scanning technique [1]. The technique allows to measure principal values of thermal conductivity tensor, coefficient of thermal anisotropy and volumetric heat capacity on core plugs and full-size core samples. The equipment of scanning technique is shown on Fig.1.

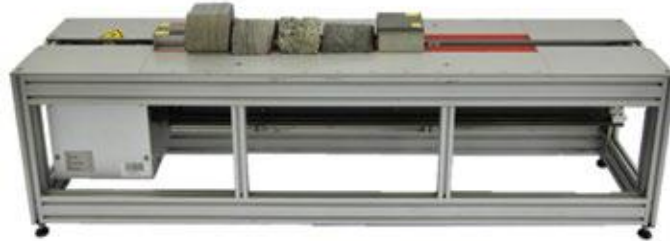


Fig.1. Optical scanning instrument Thermal Conductivity Scanner

Before the measurements one or several rock samples should be placed simultaneously on the sample holder provided with the optical scanning instrument. The optical scanning software automatically records thermal properties results for the scan line into an output file after the scanning is completed. Two reference standards should also be placed on the holder (one at the beginning and one at the end of the scan path). It gives an opportunity to establish new correlations between thermal properties and other physical properties of rocks registered by standard core logging.

The technique of optical scanning is applied for conventional and unconventional reservoirs as well [2,3]. However, in 2015-2016 we established the benefits of this technique in application to the study of the Bazhenov formation that is related to unconventional reservoirs. The Bazhenov formation is the hugest self-contained source-and-reservoir continuous petroleum system covering more than one million square kilometers (West Siberia, Russia). High lithological differentiation in Bazhenov deposits is dominated by silicic shales and carbonates accompanied by extremely high total organic carbon values (of up to 35%). Pyrite content and brittle mineralogical composition hamper standard thermal properties assessment of low permeable rocks. On Fig.2 there is an example of using thermal core logging for one of the wells of the Bazhenov formation. It gives information about distribution of thermal properties along the well and its variability. Technique of thermal core logging applied to 17 wells in 11 reservoirs of the Bazhenov formation allowed us to find the solution of the following geological and geophysical problems:

- registration of multi-scale heterogeneity of rock formations;
- registration of detailed (spatial resolution of 1-2 mm) continuous profiling of total organic carbon (TOC) along each of the studied wells with a special technique for the transformation of thermal conductivity values in TOC values;
- prediction of acoustic anisotropy of rocks in areas where interpretation of acoustic logging data is impossible or difficult from the established correlations;

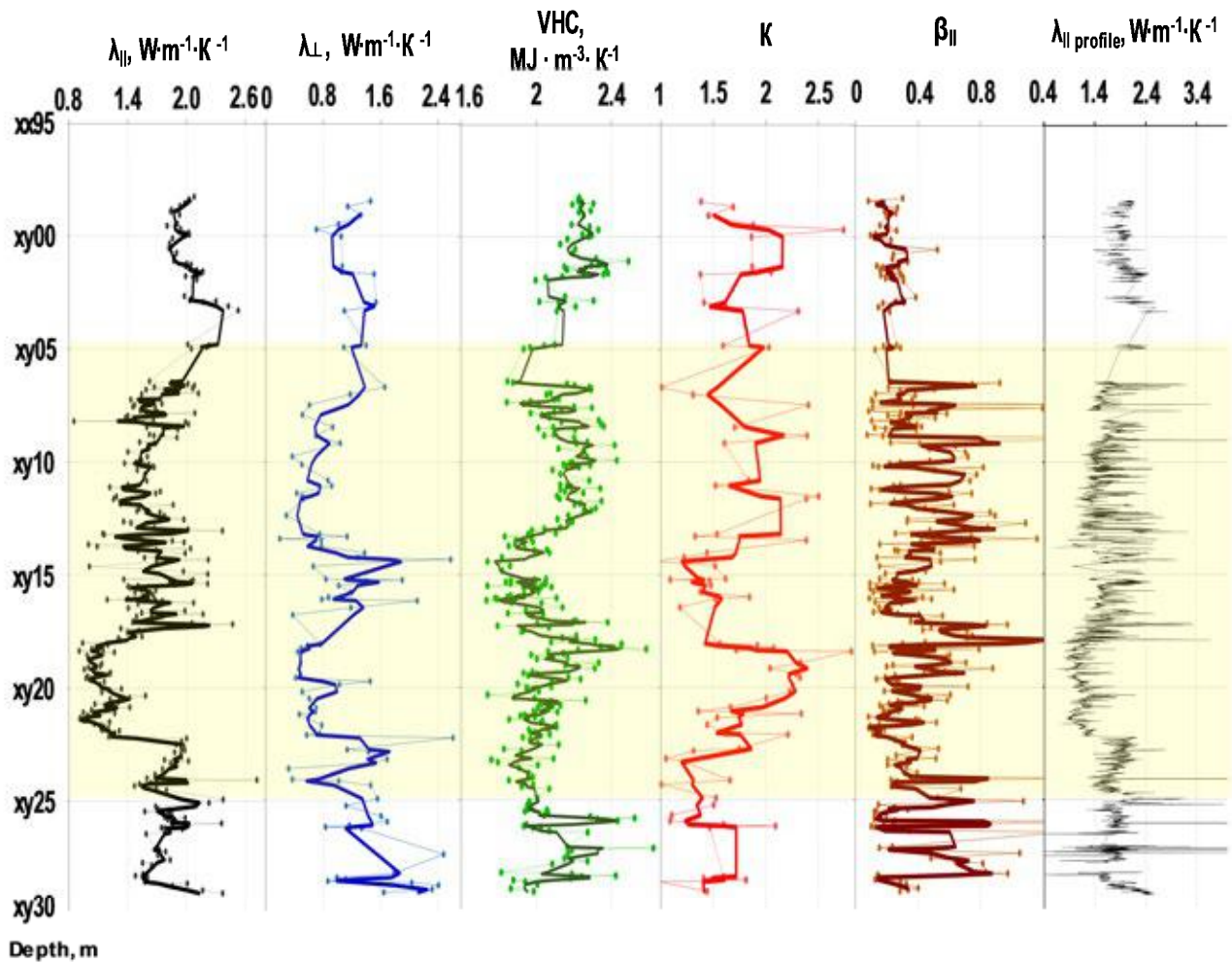


Fig. 2. The distribution of thermal properties of rocks (plots 1-5) and the continuous profile of thermal conductivity $\lambda_{|| \text{ profile}}$ (plot 6) registered along a well. Markers show results of measurements of average thermal conductivity for each core sample, lines show results of 3-points

- registration of detailed variations of elastic wave (V_p and V_s) velocities along the wells (spatial resolution of 5-10 cm) from the corresponding established correlations [2];
- definition of dynamic Young's modulus and Poisson's ratio along the wells with spatial resolution of 5-10 cm [2];
- addition (or replacement in some cases) to mechanical scratching method (that has serious limitations in study of easily breakable rocks of the Bazhenov formation) for detailed (1-2 mm) registration of rocks heterogeneity and variations of unconfined compressive strength along the wells;
- registration (spatial resolution of 1-2 mm) of natural radioactivity variations of rocks in addition to gamma ray logging and gamma spectrometry data using correlations between thermal and gamma ray logging and spectrometry data;
- identification of depth intervals where the use of gamma ray logging for total organic carbon estimation is severely restricted;
- registration (spatial resolution of 5-10 mm) of rock density variations in addition to gamma-gamma logging from correlations of rock thermal conductivity vs rock density established.

III. THERMAL CORE LOGGING TECHNIQUE

Thermal core logging technique consists of using a thermal conductivity scanner, a set of standard samples, and core samples prepared for measurements. Studied core samples and standard samples are placed on the non-moving platform. At first, the heat source switches on; then the electromechanical drive moves the heat source and temperature sensors underneath the standard and studied core samples. Both sets of samples are scanned by the heat source and infrared temperature sensors that register distribution of temperature along samples before and after heating. Thermal conductivity scanner that is applied to thermal core logging provides continuous scanning on cylindrical and flat surfaces of full-sized core samples. As a result of the metrological study, the following characteristics of rock thermal properties were obtained:

- the measurement uncertainty is not more than 3% for thermal conductivity, 5% – for thermal diffusivity, 6% – for volumetric heat capacity at confidence level of 0,95;
 - the range of thermal conductivity of rocks and minerals is 0,2÷45,0 W/(m·K);
 - the range of thermal diffusivity of rocks and minerals is (0,09÷5,0)·10⁻⁶ m²/s;
- the range of VHC of rocks and minerals is 0,8-2,8 MJ/(m³·K).

Thermal core logging is conducted on all core samples drilled out of a well and that satisfy the requirements of the equipment. The measurements are performed at room temperature and atmospheric pressure without any mechanical effect on core samples. For the estimation of thermal anisotropy of rocks, the measurements are conducted in two directions – along and perpendicular to bedding. Continuous thermal core profiling on each full-size core sample results in the following data:

- profiles of principal values of thermal conductivity tensor parallel (λ_{\parallel}) and perpendicular (λ_{\perp}) to bedding with a spatial resolution 1-2 mm for λ_{\parallel} and ~100 mm for λ_{\perp} ;
- profile of volumetric heat capacity;
- thermal inhomogeneity factors β_{\parallel} and β_{\perp} defined by minimum (λ_{\min}), maximum (λ_{\max}), and average (λ_{average}) values of thermal conductivity as $\beta = (\lambda_{\max} - \lambda_{\min})/\lambda_{\text{average}}$. These factors characterize the degree of inhomogeneity of core samples related to structural and textural characteristics of rocks [3];
- thermal anisotropy coefficient K defined as $\lambda_{\parallel}/\lambda_{\perp}$.

IV. APPLICATIONS OF THERMAL CORE LOGGING TECHNIQUE

A. Correlation between thermal and sonic anisotropy

Rock anisotropy plays an important role in petroleum geophysics. Thermal anisotropy is necessary for reconstruction of the thermal history of a basin and interpretation of temperature logging data, while acoustic anisotropy in sedimentary rocks has a significant impact on seismic data processing and reservoir characterization. However, determination of rock anisotropy is usually a complicated procedure. Common measurements on cores require sampling several plugs in different directions that leads to the problem of rock heterogeneity influence. Moreover, full-size cores will be destroyed in this case, which makes the approach time-consuming and often not reliable. Determination of anisotropy from sonic logging depends on the quality of the acoustic signal, borehole wall state and mud conditions, as well as the direction of the borehole with respect to the anisotropic axes of symmetry.

To improve the quality of rock anisotropy study, we combined the sonic logging data with fast, non-contact non-destructive measurements of principal thermal conductivity tensor components on all full-size cores. It provided a comprehensive analysis of variations in thermal and acoustic anisotropy along two wells drilled in low-permeable formations in West Siberia (Russia). A strong correlation between thermal and acoustic anisotropy was established within the Bazhenov formation [3]. It can be used to predict acoustic anisotropy via results of thermal profiling on cores in the intervals, where quantitative analysis of sonic log is impossible. If core samples are absent, thermal anisotropy can be estimated on large pieces of cuttings using a laser version of the optical scanning equipment.

B. Estimation of geomechanical parameters

Geomechanical parameters are usually estimated from sonic logging, but sometimes it is not possible technically (low quality of the acoustic signal, inappropriate borehole and mud conditions, low core quality). No wonder that there are attempts to correlate the thermal and geomechanical properties of rocks, but no one before did it with a large amount of high-quality thermal conductivity data. Coupling results of sonic logging and non-destructive non-contact thermal core logging opens wide perspectives for studying the relationship between the thermal and geomechanical properties. Analyses of the results of thermal and acoustic data variations resulted in thermal conductivity and elastic wave velocities of the Bazhenov formation rocks. Correlations for p-wave velocity $V_P = f(\lambda_{\perp}, K_{\lambda})$ and s-wave velocity $V_S = g(\lambda_{\perp}, K_{\lambda})$ were identified that allowed us to predict variations of elastic wave velocities and calculating dynamic Young's modulus and Poisson's ratio along wells.

Thus, thermal core logging can improve the quality of geomechanical parameters of the Bazhenov formation rocks by increasing the vertical spatial resolution and predicting the depth intervals where the estimation of geomechanical parameters by acoustic logging is impossible or complicated.

C. Application to basin and petroleum systems modeling

The quality of heat flow and rock thermal property data is the crucial issue in basin and petroleum system modeling. Significant deviations in thermal conductivity values were observed during our integral geothermal study of the West Siberian platform, necessitating corrections in basin models. Statistical analysis of the following parameters for the uppermost deposits was performed: variations of the thermal conductivity tensor components in the parallel and perpendicular directions to the layer stratification (assessed for 2D anisotropy model of the rock studied); volumetric heat capacity; thermal anisotropy coefficient values; and the average values of the thermal properties. The uncertainties caused by deviations of thermal conductivity data from its average values were found to be as high as 45 % leading to unexpected errors in the basin heat flow determinations.

Thus, essential spatial-temporal variations in the thermal rock properties in the study area should be taken into account in the thermo-hydrodynamic modeling of heavy oil recovery by thermal methods.

D. Total Organic Carbon estimation based on thermal core logging

A new technique providing the transformation of the thermal conductivity values into total organic carbon (TOC) values, that identifies organic-rich intervals within the low-permeable dispersive rocks was developed.

Thermal conductivity of rock matrix of the Bazhenov formation was observed to be essentially stable within the range of 2.5-2.7 W/(m·K). Stable matrix thermal conductivity along with the high thermal anisotropy coefficient is characteristic for the Bazhenov formation sediments due to the low rock porosity values. It is experimentally shown that the measured thermal parameters relate linearly to organic richness rather than to porosity coefficient deviations.

Thus, the new technique allowed us to record a continuous distribution of TOC values along wells [4].

Comparison of TOC values, estimated from the thermal conductivity values, with experimental pyrolytic TOC estimations demonstrated high efficiency of the new technique for the organic-rich intervals separation [4].

The data obtained with the new technique are essential for the hydrocarbon generation potential, for basin and petroleum system modeling application, and estimation of hydrocarbon reserves.

E. Correlation between thermal properties and natural radioactivity of rocks

It is known that the Bazhenov formation rocks are characterized by anomalously high natural radioactivity, which is related to high content of uranium [5]. A close correlation of thermal conductivity and gamma-ray logging data is observed in the Bazhenov formation [6]. Application of obtained results makes it possible to predict natural radioactivity variations along wells with much higher spatial resolution than gamma-ray logging.

Thus, the detailed distribution of natural radioactivity and uranium content, estimated from the results of thermal core logging, can be used for the express method of core correlation with depth. In addition, it becomes possible to perform a detailed estimation of the uranium content throughout the Bazhenov formation, which can be a good link with the results of geochemical studies and analysis of the elemental composition of

rocks. The detailed pattern of elements and organic matter distribution obtained by identified correlations can be applied to the analysis of the Bazhenov formation rocks, given that uranium can be typified as the indicator of deposition environment [7].

V. CONCLUSIONS

- Principal values of the thermal conductivity tensor (along and perpendicular to a bedding plane), volumetric heat capacity, thermal anisotropy coefficient, and thermal heterogeneity coefficient registered from continuous thermal core profiling are characterized by their essential variations along wells drilled in the Bazhenov formation. These thermal properties may be used for stratification and analysis of rocks anisotropy.
- Variations of total organic carbon in the Bazhenov formation rocks determine the close correlations between physical properties of rocks, including thermal conductivity, sonic wave velocities, density, and natural radioactivity.
- Established correlations between thermal and other physical parameters of rocks offer opportunities to improve the quality of studying properties of the Bazhenov formation, by the extensive use of the new thermal core profiling technique. Among important advantages of using the technique to obtain data on anisotropy, geochemical and other properties of rocks are:
 - fast non-destructive non-contact measurements on full-size core samples;
 - continuous profiling of geochemical and other properties of rocks with high spatial resolution inferred from their correlations with thermal conductivity;
 - simplicity and high performance of thermal core profiling.
- High spatial resolution of thermal core profiling offers good prospects of using this method for characterization of thin geological formations such as the Bazhenov formation.

VI. REFERENCES

- [1] Y. Popov, G. Beardmore, C. Clauser and S. Roy. (2016). ISRM Suggested methods for determining thermal properties of rocks from laboratory tests at atmospheric pressure. *Rock Mechanics and Rock Engineering*, 49(10), 4179-4207.
- [2] E. Chekhonin, E. Popov, Y. Popov, M. Spasssenykh, V. Zhukov, Y. Ovcharenko, I. Karpov, D. Zagranovskaya. (2016). Improving the data quality of geomechanical parameters of Bazhenov formation rocks by the results of thermal core logging. Presented at EAGE Conference «Geomodel-2016», 12 September, Gelendzhik, Russia, doi: 10.3997/2214-4609.201602280.
- [3] E. Popov, E. Chekhonin, S. Safonov, Y. Popov, R. Romushkevich, I. Gerasimov, S. Ursegov and I. Gurbatova. (2014). The results of examining the geological structure of the Permian-Carboniferous reservoir of the Usinsk field by continuous thermal profiling of core. Presented at EAGE Conference «Geomodel-2014», 8-11 September, Gelendzhik, Russia, doi: 10.3997/2214-4609.20142229.
- [4] Y. Popov, E. Popov, E. Chekhonin, R. Romushkevich, M. Spasssenykh, N. Bogdanovich, E. Kozlova, A. Gabova, V. Zhukov, D. Zagranovskaya, I. Karpov, I. Belenkaya, Y. Ovcharenko, A. Alekseev, G. Kalmykov, I. Gutman, E. Oksenoyd. (2016). Thermal core logging as a new method of Bazhenov formation characterization for prospecting, exploration and production of hydrocarbons. Presented at EAGE Conference «Geomodel-2016», 12 September, Gelendzhik, Russia, doi: 10.3997/2214-4609.201602175.
- [5] F. Gurary, N. Motvienko (1980). Paleogeography of Bazhenov formation by distribution of uranium content. Novosibirsk: SNIIGGMS, 81-90.
- [6] E. Popov, A. Gabova, I. Karpov, D. Zagranovskaya, R. Romushkevich, M. Spasssenykh, E. Chekhonin, Y. Popov. (2016). Correlation between thermal conductivity and natural radioactivity of Bazhenov formation rocks on the results of measurements in wells and on cores. Presented at EAGE Conference «Geomodel-2016», 12 September, Gelendzhik, Russia, doi: 10.3997/2214-4609.201602271.
- [7] I. Pluman. (1975). Distribution of uranium, thorium and potassium in formations of the West Siberian Plate. *Geochemistry*, 5, 756-767.

Novel Wearable Cardiac Rhythm Management Systems

Evgenia P. Gilshteyn*, Albert G. Nasibulin

Abstract - This paper discusses the recent results in the area of personalized Cardiac rhythm management systems using wireless Electrocardiography sensors attached to a skin or cloths. The development of such systems attracts a lot of attention nowadays as it can be used for recording and diagnosing abnormal cardiac arrhythmias. Recent achievements have allowed scientists to apply novel approaches of wearable health-monitoring systems fabrication along with integration of standard mobile phones for personalized feedback to the patient. This way of connection is much more convenient and comfortable to use compared to a conventional clinical Holter and event monitor systems. In this review paper, we present all the major components in wearable biosensor systems and discuss the progress made in this field.

Index Terms - Electrocardiography, Cardiac rhythm management, Wearable technologies, Sensors, Health monitoring, Stretchable

I. INTRODUCTION

Cardiac rhythm disorders impact millions of people each year. Some arrhythmias are difficult to diagnose as they appear sporadically in otherwise healthy adults and do not pose a threat to heart health [1]. Other arrhythmias, however, could indicate serious problems, which can cause risks to life. Field of cardiology, which deals with identifying and managing cardiac rhythm disorders, is called Cardiac Rhythm Management (CRM). It may involve the use of artificial pacemakers or implantable cardioverter-defibrillators as well as anti-arrhythmic drugs [2]. To capture frequent arrhythmias, a Holter monitor may be used. This is a portable device for continuously monitoring the electrical activity of the heart for 24 hours [3]. Such device records the electrical signals from the heart via a series of electrodes attached to the chest. The number and position of electrodes varies by model, but most recording systems employ from three to eight ones [4].

To monitor patients with cardiac symptoms that only occur sporadically (e.g. once or twice a month), a cardiac event monitor can be used. Event monitors are activated only when the arrhythmia occurs or symptoms are felt. The advantage is that these recorders may be used for a longer period. This type of device typically records cardiac events for 30-60 seconds. The recordings can then be transmitted via the telephone to Electrocardiography (ECG) technicians for further processing.

Research on the development of flexible, stretchable, conformal and wearable sensors, which can be mounted on the human skin has been gaining increasing interest [5]-[9]. These sensors are capable of providing real time information about the vital signs of an individual's health and physical condition. There have been reports on the use of these sensors in health tracking devices [10]-[13]. The various applications of wearable sensors have a range of monitoring parameters, such as body movement, body temperature, Electrocardiogram (ECG),

This work was supported by Skoltech NGP Program (Skoltech-MIT joint project).

Evgenia P. Gilshteyn: PhD student, Laboratory of Nanomaterials, Center of Photonics and Quantum Materials, Skolkovo Institute of Science and Technology, Skolkovo Innovation Center, Building 3, Moscow 143026, Russia (e-mail: evgenia.gilshteyn@skolkovotech.ru).

Albert G. Nasibulin: Professor of Laboratory of Nanomaterials, Center of Photonics and Quantum Materials, Skolkovo Institute of Science and Technology; Adjunct Professor, Aalto University School of Science, Department of Applied Physics, NanoMaterials Group (e-mail: a.nasibulin@skoltech.ru).

Electroencephalogram (EEG), and blood pressure for different uses in the biomedical, medical skin care industries [14]-[18].

This paper discusses recent achievements in the field of wearable skin-like monitors, with a focus on remote Cardiac Monitoring Systems (CMSs) and developments in wearable sensor systems, which have led to a number of exciting clinical applications.

II. WEARABLE ELECTRONICS

With the significant rise of smart devices in recent years, the powerful combination of computing technology and internet connectivity has moved from our offices and homes to our bags and pockets and finally to our clothes and body. Around 5 years ago, one could hardly predict creation of devices that can be worn on the body, or even inside the body, in combination with the idea that computing technology and the internet will be accessible anywhere as an integrated part of our environment.

Such novel devices are often linked to a smartphone that acts as the internet hub for the device and powers related apps. Other devices or technologies – such as e-textiles – can be grouped in the wearable technology category, but may not use internet connectivity.

The term wearable electronics refers to the type of electronic devices that are worn or mounted on the human body or clothing for an extended period of time [19]. Wearable devices can be divided into two classes, 1) those which are attached to clothing and 2) those which are mounted on the body.

There has been a serious need for the development of flexible and stretchable wearable electronic systems to overcome the drawbacks of ambulatory methods for monitoring the vital signs of individuals. These devices should be capable of monitoring the patient over weeks or even months. Such devices can be used in biomedical, epidermal, military and environmental monitoring applications [20]-[24]. Flexibility and stretchability can improve the functionality of these devices while they are attached on the body. During the last decade, the improvement of wearable electronic devices has led to an increasing interest in the design and fabrication of health monitoring and wearable sensors [25]-[28].

III. WEARABLE ECG SENSORS

Wearable sensors have diagnostic, as well as monitoring applications. A conceptual representation of a system for remote monitoring is shown in Fig. 1 [29]. Wearable sensors are used to gather physiological and movement data thus enabling patient's status monitoring [30]. Sensors to monitor vital signs (e.g. heart rate and respiratory rate) would be deployed, for instance, to monitor patients with congestive heart failure or patients with chronic obstructive pulmonary disease undergoing clinical intervention. Sensors for movement data capturing would be used for monitoring the effectiveness of home-based rehabilitation interventions in stroke survivors or the use of mobility assistive devices in older adults. Wireless communication is relied upon to transmit patient's data to a mobile phone or an access point and relay the information to a remote center via the Internet. Emergency situations (e.g. falls) are detected via data processing implemented throughout the system, and an alarm message is sent to an emergency service center to provide immediate assistance to patients. Family members and caregivers are alerted in case of an emergency but could also be notified in other situations when the patient requires assistance with, for instance, taking his/her medications. Clinical personnel can remotely monitor patient's status and be alerted in case a medical decision has to be made.

Despite the potential advantages of a remote monitoring system relying on wearable sensors like the one described above, there are significant challenges ahead before such a system can be utilized on a large scale. These challenges include technological barriers such as limitations of currently available battery technology as well cultural barriers such as the association of a stigma with the use of medical devices for home-based clinical monitoring.

The heart rate (HR) or pulse is the frequency of cardiac cycles, expressed as beats per minute. The HR changes according to the body's need and is susceptible to alteration in the body's normal state. Any major change to the physical or mental state of a person usually changes the pulse. Therefore, HR is used as one of the vital signs to assess the physical and mental state of a person [31].

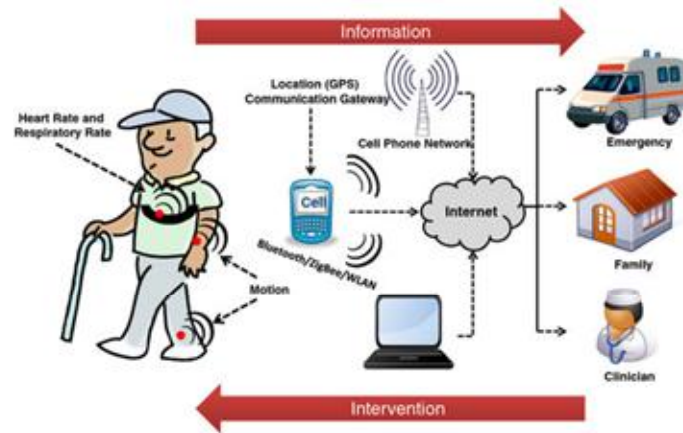


Fig. 1. Illustration of a remote health monitoring system based on wearable sensors [29].

To measure the HR more accurately, electrical, optical, and strain sensors can be used. In the case of electrical measurement, skin electrodes are used to pick up the depolarization signal from the heart muscles. This technique is known as electrocardiography (ECG).

The devices, which can be attached to the skin have moduli, thicknesses, and other Physical properties that are well matched to the epidermis, with the ability to conform to the relief on its surface. We therefore refer to this class of technology as an «epidermal electronic system» (EES). Such EES can be configured for measuring ECG, EMG (electromyography), and EEG (electroencephalography) in conformal, skin-mounted modes without conductive gels or penetrating needles provide important, system-level demonstrations. In addition to health monitoring, ECG is a useful diagnostic technique for assessing the cardiovascular system. Although ECG measurements are conventionally done using 12 leads, the signal can be picked up by using two electrodes placed on the chest [32]. However, the signal intensity drops as the spacing between the electrodes is reduced [33]. Xu et al. used two electrodes in a band-aid form, as shown in Fig. 2 [34].

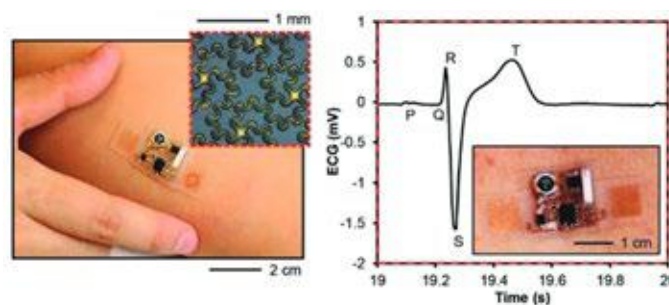


Fig. 2. Electrocardiography (ECG) using a flexible and stretchable sensor system. Left - optical images of the sensor system on the forearm, with a pair of epidermal electrodes in self-similar serpentine mesh layouts (inset optical micrograph); right - a detailed view of the ECG signal shows the expected Q, R, and S waveforms [30].

Andreoni et al. [35] designed custom T-shirt with embedded electrodes for monitoring ECG, HR, and R-R interval. The electrodes were made of silver-based conductive yarns and relied on body sweat to improve the conductivity of the skin-electrode interface and signal quality. The device also included a three-axis

accelerometer for fall detection, and it could transmit the data over low-power Bluetooth. An elastic fabric-made ECG vest was presented in [36], which consisted of three electrodes, a data acquisition module and also supported robust contact of the electrodes with the skin. The electrodes were fabricated from Ni/Cu coated polymer foam that was enclosed by an Au-coated conductive fabric. The skin-electrode impedance was low and remained stable over a longer period, due to the conductive and flexible nature of the substrate.

Jeong et al. [37] proposed an ECG monitoring system where they used similar technology as [36] to develop flexible capacitive electrodes and integrated them in a chest belt. A noise cancellation and peak detection algorithm was performed on the raw ECG data to find out the QRS complex, and HR, although a detailed description of the algorithm was not provided. The authors reported achieving high sensitivity and high accuracy in detecting QRS complexes. The electrodes used in the ECG systems presented in [35]–[37] were in direct contact with the skin.

Nemati et al. [38] embedded a small, low-power, wireless ECG monitoring system in a stretchable belt where three capacitive electrodes were integrated into a cotton T-shirt, thus enabling ECG measurements to be performed over the cloth. The signal processing and communication modules were mounted on a small two-layer printed circuit board (PCB). Power consumption was minimized by selecting low power electronic components for the system, as well as by adopting idle mode signal sampling technique. However, the rigid electrodes can be inconvenient to the users and may induce motion artifacts in the signal.

Many researchers have developed and made use of piezoelectric pressure sensors for measuring the HR by sensing the arterial pulse wave generated by the periodic contraction and relaxation of the heart. Yoon et al. [39] as well as Tajitsu et al. [40] designed a skin attachable piezoelectric pressure sensor and demonstrated its usability in HR estimation by sensing the pulse wave in human artery. The pulse wave measured from the wrist by this sensor had similar pattern as the ECG signal and showed high accuracy as well as less vulnerability to motion-induced noise.

Some researchers have exploited system-on-chip (SOC) technologies to integrate both analog and digital signal processing units for on-chip ECG signal processing. Izumi et al. [41] developed a wearable system that incorporated a near field communication (NFC) module, a three-axis accelerometer, and an ECG processor chip.

Among the novel approaches being developed is one that uses almost no power. MC10, a venture-backed company, is commercializing Professor John Rogers' previous research on stretchable inorganic electronics (Fig. 3).

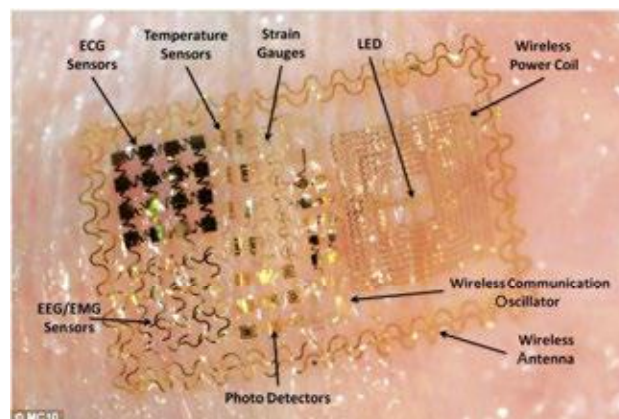


Fig. 3. Biostamp prototype - Courtesy of MC10 Company web-site [6].

The prototype of health monitoring system a seamless sensing sticker that by stretching, flexing, and moving with the body, is redefining the interface between humans and electronics [42]. MC10 is developing a number of products in multiple markets, including fitness, consumer health, and medical devices. This device uses near-field communications like an RFID tag and contains a very small, low-capacity thin-film battery that is also charged through the near-field link.

One more approach in wearable ECG devices fabrication is implementation of nanomaterials, such as carbon nanotubes. Ha-Chul Jung et.al. successfully fabricated CNT/PDMS (carbon nanotubes/polydimethylsiloxane) composite electrodes which were flexible, biocompatible, and suitable for long-term measurement of the ECG signals [43]. The proposed CNT/PDMS composite electrodes measured ECG signals robustly even in the presence of motion or sweat, and were connectable to commercial ECG machine without an adaptor. The aforementioned results indicate that the composite electrodes are suitable for long-term ECG monitoring due to biocompatibility and robust performance under conditions of motion and sweat.

IV. CONCLUSION

In conclusion, a plethora of wearable medical devices has been demonstrated with applications in vital signs monitoring, such as ECG signal sensing. In this review paper, we listed and discussed most recent wearable monitoring devices, focusing on biosignals such as heart rate, by mean of ECG.

The primary purpose of a wearable health monitoring system is to allow people to lead independent and active lives in their familiar home environment while ensuring continuous, non-invasive, non-intrusive, and seamless surveillance of their health and physical well-being. However, despite significant advances in the past decade, there are challenges that require further research and development in order to improve the performance of such systems. First, the biosignal measurement systems very often suffer from low signal-to-noise ratio (SNR) that primarily evolves from the noise induced by the movement of the user. Second, a key concern for the wearable healthcare system is associated with the privacy and security of the sensitive medical information of the user. Third, low power consumption and high energy efficiency are critical for long-term monitoring systems. Power requirement of the system can be satisfied by using low power components, more efficient batteries or by employing energy harvesting techniques. Fourth, an efficient data compression algorithm needs to be implemented in the central node in order to deal with a large volume of data and transmit them to the nearest gateway. Fifth, in order to achieve widespread acceptance among the people, the systems need to be affordable, easy-to-use, un-obtrusive, and inter-operable among various computing platforms. Authors hope that this review will provide readers with the recent progress in these novel biosensors.

V. REFERENCES

- [1] Peter Leijdekkers, Valerie Gay, and Edward Barin, "Trial Results of a Novel Cardiac Rhythm Management System Using Smart Phones and Wireless ECG Sensors", M. Mokhtari et al. (Eds.): ICOST 2009, LNCS 5597, pp. 32–39, 2009.
- [2] ACC/AHA/HRS 2008 Guidelines for Device-Based Therapy of Cardiac Rhythm Abnormalities, Heart Rhythm (May 2008).
- [3] Holter monitor – Source: Wikipedia, the free encyclopedia: https://en.wikipedia.org/wiki/Holter_monitor.
- [4] Crawford, M.H., et.al.: ACC/AHA guidelines for ambulatory electrocardiography, *J. Am. Coll. Cardiol.* 34, 912-948 (1999).
- [5] D. H. Epi, J. A. Rogers, "Stretchable Electronics: Materials Strategies and Devices", *Adv. Mater.*, vol. 20, pp. 4887-4892, 2008.
- [6] Dae-Hyeong Kim, Nanshu Lu, Rui Ma, Yun-Soung Kim, Rak-Hwan Kim, Shuodao Wang, Jian Wu, Sang Min Won, Hu Tao, John A. Rogers et.al., *Epidermal Electronics, Science*, 2011, Vol. 333.
- [7] D. H. Kim, J. H. Ahn, W. M. Choi, H. S. Kim, T. H. Kim, J. Song, Y. Y. Huang, Z. Liu, C. Lu, J. A. Rogers, "Silicon nanomembranes for fingertip electronics", *Science*, vol. 320, pp. 507-511, 2008.
- [8] W. Honda, S. Harada, T. Arie, S. Akita, K. Takei, "Wearable, Human-Interactive, HealthMonitoring, Wireless Devices Fabricated by Macroscale Printing Techniques", *Adv. Funct. Mater.*, vol. 24, pp. 3299–3304 2014.
- [9] J. Wieremczuk, G. Tarapata, R. Jachowicz, "Humidity Sensor Printed on Textile with use of Ink-jet technology" *Procedia Engineering* 47, 1366 – 1369, 2012.
- [10] S. Yao, Y. Zhu, "Wearable multifunctional sensors using printed stretchable conductors made of silver nanowires", *Nanoscale*, vol. 6, pp. 2345–2352, 2014.
- [11] S. Krishnamoorthy, "Nanostructured Sensors for Biomedical Applications — a Current Perspective" *Current Opinion in Biotechnology*, 34, pp. 118–124, 2015.
- [12] P. Kassal, J. Kim, R. Kumar, W. R. de Araujo, I. M. Steinberg, M. D. Steinberg, J. Wang, "Smart Bandage with Wireless Connectivity for Uric Acid Biosensing as an Indicator of Wound Status" *Electrochemistry Communications* 56, pp. 6–10, 2015.
- [13] C. Wong, Z. Q. Zhang, B. Lo, G. Z. Yang, "Wearable Sensing for Solid Biomechanics: A Review" *IEEE sensors journal*, Vol. 15, pp. 2747–2760, 2015.
- [14] J. R. Windmiller, J. Wang, "Wearable Electrochemical Sensors and Biosensors: A Review", *Electroanalysis*, vol. 25, pp. 29–46, 2013.
- [15] S. Patel, H. Park, P. Bonato, L. Chan, M. Rodgers, "A review of wearable sensors and systems with application in rehabilitation" *Journal of Neuro Engineering and Rehabilitation*, pp.9-21, 2012.
- [16] O.D Lara, M.A Labrador, "A Survey on Human Activity Recognition using Wearable Sensors," *Communications surveys & tutorials, IEEE*, vol.15, pp.1192-1209, 2013.

- [17] P. Bonato, "Wearable Sensors and Systems," *Engineering in medicine and biology magazine, IEEE*, vol.29, pp.25-36, 2010.
- [18] P. Shyamkumar, P. Rai, S. Oh, M. Ramasamy, R. E. Harbaugh, V. Varadan, *Electronics*, 2014, 3, 504.
- [19] H. Ueda, M. Tsukamoto, S. Nishio, "W-mail: an electronic mail system for wearable computing environments" *Proceedings of the 6th annual international conference on Mobile computing and networking*, pp.248-291.
- [20] H. C. Ko1, M. P. Stoykovich, J. Song, V. Malyarchuk, W. M. Choi, C. J. Yu, J. B. Geddes III, J. Xiao, S. Wang, Y. Huang, J. A. Rogers, "A hemispherical electronic eye camera based on compressible silicon optoelectronics, *Nature*, Vol. 454, pp. 748-753, 2008.
- [21] D. H. Kim, R. Ghaffari, N. Lu, S. Wang, S. P. Lee, H. Keum, R. D'Angelo, J. A. Rogers, et.al., "Electronic sensor and actuator webs for large-area complex geometry cardiac mapping and therapy" *PNAS*, Vol. 109, pp. 19910-19915, 2012.
- [22] C. Yu, Z. Duan, P. Yuan, Y. Li, Y. Su, X. Zhang, Y. Pan, L. L. Dai, R. G. Nuzzo, Y. Huang, H. Jiang, J. A. Rogers, "Electronically Programmable, Reversible Shape Change in Two- and Three-Dimensional Hydrogel Structures". *Adv. Mater.*, Vol. 25: pp.1540, 2013.
- [23] W. H. Yeo, Y. S. Kim, J. Lee, A. Ameen, L. Shi, M. Li, S. W. R. Ma, S. H. Jin, Z. Kang, Y. Huang, J. A. Rogers, "Multifunctional Epidermal Electronics Printed Directly Onto the Skin", *Adv. Mater.*, ol. 25, pp. 2773-2778, 2013.
- [24] Y. H. Lee, J. S. Kim, J. Noh, I. Lee, H. J. Kim, S. Choi, J. Seo, S. Jeon, T.S. Kim, J.Y. Lee, J. W. Choi, "Wearable Textile Battery Rechargeable by Solar Energy" *Nano Lett*, Vol. 13, pp. 5753-5761, 2013.
- [25] G. Suci, C. Butca, A. Ochian, S. Halunga; "Wearable sensors for health monitoring" *Proc. SPIE 9258, Advanced Topics in Optoelectronics, Microelectronics, and Nanotechnologies VII*, 2015.
- [26] R. Paradiso, G. Loriga, N. Taccini, "A wearable health care system based on knitted integrated sensors," *IEEE Transactions on Information Technology in Biomedicine*, vol.9, pp.337-344, 2005.
- [27] R. Jafari, A. Encarnacao, A. Zahoor, F. Dabiri, H. Noshadi, M. Sarrafzadeh, "Wireless sensor networks for health monitoring," *The Second Annual International Conference on Mobile and Ubiquitous Systems: Networking and Services*, pp.479-481, 2005.
- [28] A. Pantelopoulou, N. Bourbakis, "A survey on wearable biosensor systems for health monitoring," *30th Annual International Conference of the IEEE on Engineering in Medicine and Biology Society*, pp.4887-4890, 2008.
- [29] Shyamal Patel, Hyung Park, Paolo Bonato, Leighton Chan and Mary Rodgers, A review of wearable sensors and systems with application in rehabilitation, *Journal of Neuro Engineering and Rehabilitation* 2012, 9:21.
- [30] Yasser Khan, Amine E. Ostfeld, Claire M. Lochner, Adrien Pierre, and Ana C. Arias, *Monitoring of Vital Signs with Flexible and Wearable Medical Devices*, *Adv.Mater.*2016, DOI: 10.1002/adma.201504366
- [31] D. Evans, B. Hodgkinson, J. Berry, *Int. J. Nurs. Stud.*2001, 38, 643.
- [32] E. Nemat, M. J. Deen, T. Mondal, *IEEE Commun. Mag.*2012, 50, 36.
- [33] S. E. Derenzo, *Practical Interfacing in the Laboratory: Using a PC for Instrumentation, Data Analysis and Control*, Cambridge University Press, Cambridge, UK 2003.
- [34] S. Xu, Y. Zhang, L. Jia, K. E. Mathewson, K.-I. Jang, J. Kim, H. Fu, X. Huang, J. A. Rogers, et.al. *Science*, 2014, 344, 70.
- [35] Andreoni, G.; Perego, P.; Standoli, C. *Wearable monitoring of elderly in an ecologic setting: The SMARTA project* (accessed on 5 January 2017): <https://sciforum.net/conference/ecsa/paper/3192/download/pdf>
- [36] Tseng, K.C.; Lin, B.-S.; Liao, L.-D.; Wang, Y.-T.; Wang, Y.-L. *Development of a Wearable Mobile Electrocardiogram Monitoring System by Using Novel Dry Foam Electrodes*. *IEEE Syst. J.* 2014, 8, 900-906.
- [37] Lee, J.; Heo, J.; Lee, W.; Lim, Y.; Kim, Y.; Park, K. *Flexible Capacitive Electrodes for Minimizing Motion Artifacts in Ambulatory Electrocardiograms*. *Sensors* 2014, 14, 14732-14743.
- [38] Nemat, E.; Deen, M.; Mondal, T. *A wireless wearable ECG sensor for long-term applications*. *IEEE Commun. Mag.* 2012, 50, 36-43.
- [39] Yoon, S.; Cho, Y.-H. *A Skin-attachable Flexible Piezoelectric Pulse Wave Energy Harvester*. *J. Phys. Conf. Ser.* 2014, 557, 012026.
- [40] Tajitsu, Y. *Piezoelectret sensor made from an electro-spun fluoropolymer and its use in a wristband for detecting heart-beat signals*. *IEEE Trans. Dielect. Electr. Insul.* 2015, 22, 1355-1359.
- [41] Izumi, S.; Yamashita, K.; Nakano, M.; Kawaguchi, H.; Kimura, H.; Marumoto, K.; Fuchikami, T.; Fujimori, Y.; Nakajima, H.; Shiga, T.; et al. *A Wearable Healthcare System With a 13.7 μA Noise Tolerant ECG Processor*. *IEEE Trans. Biomed. Circuits Syst.* 2015, 9, 733-742.
- [42] MC10 – Official company web site <https://www.mc10inc.com/>
- [43] H.-C. Jung, J.-H. Moon, D.-H. Baek, J.-H. Lee, Y.-Y. Choi, J.-S. Hong, S.-H. Lee, *IEEE Trans. Biomed. Eng.*2012, 59, 1472.

Review of Alkaline - Surfactant - Polymer (ASP) Flooding: Past and Present

Anastasia Ivanova

Abstract - More than 50% of original oil in place is still trapped in the reservoir after primary and secondary oil recovery. Thus, there is a need in tertiary recovery or enhanced oil recovery methods. It is well known that chemical flooding is one of the most perspective and widely used technologies for enhanced oil recovery. Chemical or alkaline-surfactant-polymer flooding is a combination method in which alkali, surfactant and polymer are injected into the wellbore. However, despite its effectiveness, this method has several limits. Pilot and field experiments have been conducted to obtain optimal chemical compositions for different reservoirs. This paper focuses on the review of ASP flooding technology and its application in oil industry. In addition, several suggestions are proposed for chemical flooding in carbonate reservoirs.

Index Terms - Enhanced Oil Recovery; Surfactant/polymer/alkaline flooding; Interfacial tension; Synergy in ASP.

I. NOMENCLATURE

k_{rw}	water relative permeability (-)
k_{ro}	oil relative permeability (-)
μ_o, μ_w	viscosities of oil and water respectively (Pa*s)
v	Darcy's velocity (m/s)
μ	brine viscosity (Pa*s)
σ	oil/water interfacial tension (mN/m)
θ	contact angle ($^\circ$)
E_{D0}	microscopic displacement efficiency (-)
E_A	areal displacement efficiency (-)
E_V	vertical displacement efficiency (-)
B_0	formation volume factor of the oil (bbl/stb)
S_0	oil saturation (%)
V_p	permeability variation (%)

II. INTRODUCTION

There are three oil recovery methods for hydrocarbon recovery – primary, secondary and tertiary. Primary recovery is due to the natural energy that moves oil from formation to the producing wells by the pressure differential between the high pressure in rock formation and low pressure in the wellbore. This method is limited and may recover up to 20% of original oil in place. In secondary recovery, water or gas are injected for natural pressure maintenance. This is a widely used method for decreasing residual oil saturation by oil displacement. Waterflooding is applied in water-wet reservoirs. After waterflooding, as much as 50% of original oil in place is still trapped in the reservoir due to high capillary forces of water. Therefore, there is a need in tertiary recovery or enhanced oil recovery (EOR). Tertiary methods include chemical flooding, gas methods, thermal recovery (steam injection) or a combination of two or more of those methods. Injected fluids react with reservoir rocks and alter their properties, which helps to gain additional oil from the reservoir. Tertiary methods aid in recovery of about 80% of original oil in place in oil-wet reservoirs [1] - [7]. This paper focuses on

Ivanova A.A. is from the Hydrocarbon Recovery Center, Skolkovo Institute of Science and Technology, Skolkovo Innovation Center, Building 3, Moscow 143026, Russia [e-mail: Anastasia.ivanova@skoltech.ru].

advantages and disadvantages of one of the tertiary methods named chemical flooding. Chemical flooding includes alkaline, polymer, surfactant flooding either together or separately. In the last years, this technology have become very popular to research, because of growing demand from the industry.

III. RESEARCH PAPER PREPARATION

A. Polymer flooding

The main object of polymer solution injection is increasing viscosity of water, so sweep efficiency is improved by reducing viscous fingering (Fig.1).

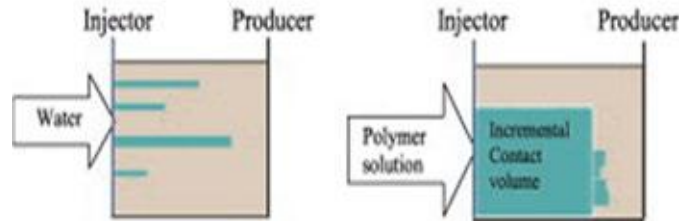


Fig.1 Reduction of viscous fingering by adding polymer to water [1]

An important parameter for the indication of a displacement process is mobility ratio between water (displacing fluid) and oil (displaced fluid). By definition, mobility ratio is a ratio of water mobility to oil mobility (Eq. 1):

$$M = \frac{\lambda_w}{\lambda_o} = \frac{k_{rw}/\mu_w}{k_{ro}/\mu_o} = \frac{k_{rw}\mu_o}{k_{ro}\mu_w} \quad (1)$$

It is well known, that volumetric sweep efficiency will increase if M decreases. Polymer addition to water causes viscosity increase, which results in water mobility reduction. Thus, water will move slowly. This effect is called a permeability reduction effect [5].

Polymer solution viscosity depends on the concentration of added polymer. The more concentration of polymer in solution, the higher the viscosity. There are several types of polymers which are used in oil recovery, but generally, Hydrolyzed Polyacrylamide (HPAM) is used, because it is cheap, easy to produce and stable under typical reservoir conditions. HPAM is an anionic polymer with strong intra-chain molecular repulsion. If salt is added to polymer solution, repulsion between molecules will reduce, and polymer precipitation may occur. Thus, polymer solution viscosity will reduce. Polymer solution viscosity depends on salinity and can be estimated by the Flory-Huggins equation [8]. When the value of salinity in reservoir is high, polymer will disintegrate, and solution viscosity will be low. This means that the amount of polymer needed for viscosity maintenance is huge.

It is experimentally shown that polymer with high molecular weight (up to 10^6 g/mol) imparts higher viscosity to solution than the low molecular weight polymer at the same concentration [9], [10]. Therefore, it is preferable to use the high molecular weight polymer.

Indeed, polymer addition to water will decrease residual oil saturation. This is a significant factor for oil recovery.

B. Surfactant flooding

The main object of surfactant solution injection is low interfacial tension (IFT) effect between oil and brine solution. It is known that to reduce residual oil saturation, the capillary number must be up to 10^{-4} [5]. Capillary number is defined as a ratio of viscous forces to capillary forces (Eq. 2).

$$N_c = \frac{v*\mu}{\sigma*cos\theta} \quad (2)$$

A typical capillary number of waterflooding is 10^{-7} . Thus, as can be seen from Eq.2, there are three ways to increase N_c : 1) increasing brine viscosity; 2) increasing injection fluid velocity and 3) decreasing IFT between brine and oil. Injection fluid velocity is limited due to pump capacity. Moreover, if velocity of fluid is high enough, then injection pressure can be higher than formation pressure. Brine viscosity can be increased by polymer

addition. However, sometimes polymer injection is limited too; for instance, large polymer molecules cannot penetrate through small formation pores. The only option left is to reduce IFT.

One promising way to minimize capillary pressure (or IFT) of water is by adding surfactants to brine solution. Because of amphiphilic properties (Fig.2), surfactant molecules may orient on dimeric interface between oil and water and reduce interfacial tension. Thus, low oil-water interfacial tension reduces the capillary pressure and allows water to displace additional oil. To recover additional oil from formation, the IFT between a surfactant solution and oil should be reduced from 20 – 40 to 10^{-2} – 10^{-3} mN/m [3], [5]. It is known that not every surfactant solution may cause such great reduction. There are only a few solutions and they are expensive. However, such surfactants are used since due to the lowest IFT, oil droplets can flow free through pore throats because of reduced capillary pressure of water. Then, the oil droplets move forward and merge with oil down the stream to form a huge oil bank, which can be more easily recovered.

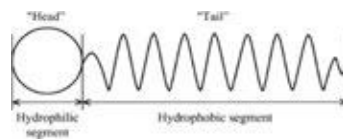


Fig.2 Amphiphilic surfactant molecule [2]

Due to amphiphilic properties, surfactants are added to change wettability of rock surface, for instance, in oil-wet carbonate reservoirs [11], [12].

The main problem with using surfactants is their high adsorption on rock surfaces. Surfactants adsorption depends on many factors, such as pH of solution, hydrophilic or hydrophobic types of rock surfaces and surface charge. If the adsorption is too high, then large quantities of surfactants will be required to produce a small amount of oil, which is not economic. There is one way to minimize the adsorbed amount of surfactant - to add alkaline [13] - [16].

C. Alkaline flooding

Generally, NaOH and Na_2CO_3 or mixture thereof are used in alkaline flooding.

In comparison with surfactants, alkalis are less expensive and environmental friendly, so alkalis adsorption on the grain surface instead of surfactants makes flooding economically preferable.

Due to electrostatic attraction between opposite charges, surfactant molecules will adsorb on rock surface. Thus, a huge amount of surfactant will be wasted. However, if alkali is added, it can also adsorb on surface, thereby preventing surfactant adsorption. The mechanism of competitive adsorption between anionic surfactant and alkali on carbonate rock surface is presented on Fig.3.

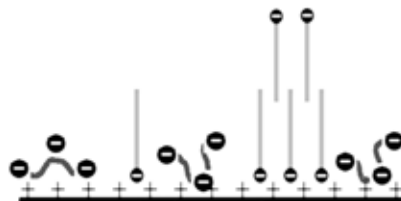


Fig.3. The mechanism of competitive adsorption between anionic surfactant and alkali on carbonate rock surface [17]

It should be noted that decreasing surfactants adsorption by adding alkalis is preferable in case surfactant molecules and rock surface have opposite charge, for instance, cationic surfactant and negative charged surface or anionic surfactant and positive charged surface.

Another important fact about alkalis injection is capability to generate in situ surfactants (Fig.4). Alkalis may react with the acid component in a crude oil.

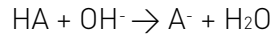


Fig.4. Reaction of surfactant generation [5]

Due to this, less surfactants are needed. However, it is experimentally shown that generated surfactants cannot decrease IFT to 10^{-2} , their amount is not enough. Therefore injecting only alkaline solution without surfactant solution into wellbore will not lead to increasing oil recovery.

In addition, alkaline solutions may cause precipitation of several inorganic scales. In fact, when alkaline solutions are injected into wellbore, concentration of OH^- ions is increased. In high salinity brines, when divalents Ca^{2+} and Mg^{2+} exist in high concentration, OH^- ions react with them and cause several scales precipitation. Especially, it happens in carbonate rock formations, where amount of Ca^{2+} and Mg^{2+} is too high. Due to this, formation rocks lose their flow properties. Moreover, polymer solution may lose its viscosity at such conditions.

D. Synergy of alkaline – surfactant – polymer (ASP) flooding

The key of using three components together is their synergy effect. For improving displacement efficiency, alkaline - surfactant - polymer slug is injected into wellbore [18] - [21]. Thus, more residual oil can be recovered from one well. As can be seen from Eq.3 [1], overall oil recovery is defined as:

$$E_{or} = \frac{S_o * E_{DO} * E_A * E_V * V_p}{B_o} \quad (3)$$

Therefore, to achieve maximum of oil recovery (Eq.3), all chemical compounds should be injected. Synergy effect makes ASP flooding an economically and efficiently profitable technology.

The example of ASP flooding is shown on Fig.5. Typical ASP formulations involve 0.2 PV (pore volume) of 1% surfactant and 0.5% alkali, chased by 0.3 PV or more of a solution containing 1000 ppm polymer [1].

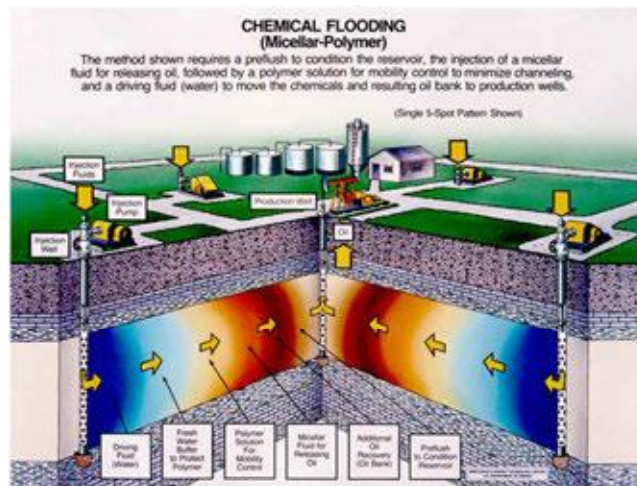


Fig.5. ASP flooding

E. Status of ASP technology

In comparison with other methods, ASP is the most complicated and expensive. Nevertheless, ASP flooding may improve oil recovery from geologically challenging reservoirs and unconventional reservoirs.

The one serious ASP flooding challenge is surfactant molecules adsorption on rock surfaces. Addition of alkalis is not suitable for every reservoir conditions. It is known that around 60% of rocks are carbonates, however in carbonates rock formations alkalis injection will not work. In addition, anionic surfactants such as petroleum sulphonates or α -olefin sulphonates are more often used, due to ultra-low IFT reduction. In comparison with cationic surfactants, anionic ones are less expensive and more environmentally friendly. Those facts make their use preferable in all rocks types. However, in carbonates high adsorption may occur, so anionic surfactant flooding has economic barriers.

Therefore, the technology open questions are:

- 1) Can we use ASP flooding in carbonates?
- 2) Are there more advantages of alkaline solution injection than disadvantages?
- 3) Is there an alternative method to decrease surfactants molecules adsorption on rocks?

Another problem involves polymer not-reversible destruction under reservoir conditions with high temperature and/or high salinity. Until nowadays there is no polymer, which will be stable under such conditions. Therefore another question to work out is:

- 4) Can we synthesize a more stable polymer?

To overcome listed below questions, researchers from over the world start to investigate nanoparticles properties for using in ASP flooding. As a result, in the last few years, nanotechnology has been applied in enhanced oil recovery [22] – [28]. There are several works dedicated to surfactant and polymer flooding. It was experimentally proven that addition of silica nanoparticles to surfactant solution reduces adsorption not only on sandstone, but also on carbonates rock formations and alters wettability from oil-wet to water-wet type. As a result, that will lead to the reduction of residual oil saturation. To explain these results, it is expected that surfactant adsorption reduction on carbonate rocks is more due to particles adsorption than surfactants molecules. Silica nanoparticles have negative surface charge and can attract to positive charge surfaces. Moreover, silica nanoparticles are not expensive and cost the same as alkali. Thus, flooding cost will not increase, that is a very important to economics.

Moreover, there are also several works focused on polymer mixture with different nanoparticles. It was found that addition of Al_2O_3 nanoparticles makes polymer more stable, thus, viscosity of solution can be maintained high enough [24]. In addition, it was found that Fe_3O_4 , TiO_2 , ZnO_2 nanoparticles have the same influence of polymer solutions [24], [26].

As a result, nanotechnology is a new and very perspective approach in using for enhancing oil recovery. However, there have been no field tests with nanoparticles in brine solutions, all experiments are only provided in the laboratories.

Consequently, the summary of all above mentioned about ASP technology and synergy of its components is:

- 1) Alkalis decrease surfactant adsorption and react with crude oil to generate in situ soaps, thus less surfactant is needed;
- 2) Nanoparticles with surfactant decrease IFT between oil and brine solution, and also surfactant molecules adsorption, thus less surfactant is needed;
- 3) The microscopic displacement efficiency is increased by surfactant and alkali injection;
- 4) The areal displacement efficiency and the vertical displacement efficiency are increased by polymer;
- 5) Polymer improves sweep efficiency.

Therefore, it is still needed to perform many laboratory experiments to find the best chemical composition for each reservoirs. It seems very interesting to apply nanoparticles instead of alkalis, because they influence on solutions properties in the same way.

As for me, applying nanotechnology in oil recovery seems to be prospective. However, experimental data were provided only in research laboratories, not in the real field cases. Thus, to implement this new technology in industry, it is needed to perform more experiments, which include measurements of nanoparticles adsorption on surface, their distribution throw porous media etc.

IV. REFERENCES

- [1] Olajire, A.A. "Review of ASP EOR (alkaline surfactant polymer enhanced oil recovery) technology in the petroleum industry: prospects and challenges", *Energy*, 2014, pp. 1-20.
- [2] Szymański A. "Determination of Sulfonamide Residues in Food by Micellar Liquid Chromatography", *Toxicol. Mech. Methods*, 2008.
- [3] Lake L.W. "Enhanced oil recovery". Presented at Prentice-Hall, 1989.
- [4] Stegemeier G.L. "Mechanisms of entrapment and mobilization of oil in porous media, In *Improved Oil Recovery by Surfactant and Polymer Flooding*", Academic Press, 1977, pp. 55-91.
- [5] James J., Sheng A. "A comprehensive review of alkaline-surfactant-polymer (ASP) flooding", *Asia-Pac. J. Chem. Eng.*, 2014, pp. 471-489.
- [6] Charest M. "Alkaline-Surfactant-Polymer (ASP) Flooding in Alberta" *Canadian discovery digest*, 2013, pp. 52.
- [7] Dreiss C.A. "Wormlike micelles: where do we stand? Recent developments, linear rheology and scattering techniques", *Soft matter*, 2007, pp. 956-970.
- [8] Flory P.J. "Principles of Polymer Chemistry» New York: Cornell University Press, 1953.
- [9] Holmberg K., Jonsson B., Kronberg B., Lindman B. "Surfactants and polymers in aqueous solution", 2nd Ed. New York: John Wiley & Sons, 2003, pp. 562.
- [10] Liu S., Zhang D.L., Yan W., Puerto M., Hirasaki G.J., Miller C.A. "Favorable attributes of alkaline surfactant polymer flooding", *SPE Journal*, 2008, pp. 5-16.
- [11] Manrique E.J., Muci V.E., Gurfinkel M.E. "EOR field experiences in carbonate". Presented at the SPE Asia Pacific Oil and Gas Conference and reservoirs in the United States SPE Reserv. Eval. Eng., 2007, pp. 667 - 686.
- [12] Sheng J.J. "Surfactant enhanced oil recovery in carbonate reservoirs" Chapter 12. In *EOR Field Case Studies*, Elsevier, 2013.
- [13] Abhijit S., Ojha K., Mandal A." Interactions between Acidic Crude Oil and Alkali and Their Effects on Enhanced Oil Recovery", *Energy Fuels*, 2011, pp.1642-1649.
- [14] Wyatt K., Pitts M., Surkalo H. "Mature waterfloods renew oil production by alkali-surfactant-polymer flooding". Presented at SPE Eastern Regional Meeting, Lexington, 2002.
- [15] Ehrlich R., Hasiba H. H., Raimondi P. "Alkaline waterflooding for wettability alteration - evaluating a potential field application". *J. Pet. Technol.*, 1974, pp.1335-1343.
- [16] Li D., Shi M., Wang D., Li Z. "Chromatographic separation of chemicals in alkaline surfactant polymer flooding in reservoir rocks in the Daqing oil field". In: *Proceedings of SPE International Symposium on Oilfield Chemistry, USA, 2009*.
- [17] Wang D., Cheng J., Li Q., Li L., Zhao C., Hong J. "An alkaline bio-surfactant polymer flooding pilots in Daqing Oil Field", *Paper SPE 57304*, Malaysia, 1999.
- [18] Hirasaki G.J., Miller C.A., Puerto M. "Recent advances in surfactant EOR", *SPE Journal*, 2011, pp. 889-907.
- [19] Ibrahim Z.B., Manap A.A., Hamid P.A., Hon V.Y., Lim P.H., Wyatt K. "Laboratory aspect of chemical EOR processes evaluation for Malaysian oilfields", *SPE Exhibition, Australia, 2006*.
- [20] Sorbie K.S. "Polymer improved oil recovery", London: Blackie and Son Ltd, 1991.
- [21] Alvarado V., Manrique E. "Enhanced Oil Recovery: An Update Review", *Energies*, 2010.
- [22] Suleimanov, B.A., Ismailov, F.S., Veliyev, E.F. "Nanofluid for enhanced oil recovery", *J. Pet. Sci. Eng.*, 2011, pp. 431-437.
- [23] Khiabani A., Darabad J.S., Azin R., Arya S. "Wettability Alteration in Carbonates using Zirconium Oxide Nanofluids: EOR Implications", *Energy Fuels*, 2012, pp. 1028-1036.
- [24] Hendraningrat L., Torsæter O. "Metal oxide-based nanoparticles: revealing their possibility to enhance the oil recovery at different wettability systems", *Appl. Nano Sci.* Springer, 2014.
- [25] Mohajeri M., Hemmati M., Sadatshkarabi A. "An experimental study on using a nanosurfactant in an EOR process of heavy oil in a fractured micromodel", *J. Petrol. Sci. Eng.*, 2015, pp.162-173.
- [26] Roustaei A., Saffarzadeh S., Mohammadi M. "An evaluation of modified silica nanoparticles' efficiency in enhancing oil recovery of light and intermediate oil reservoirs", *Egyptian Journal of Petroleum*, 2013, pp. 427-433.
- [27] Esmailzadeh1a P., Fakhroueian Z., Bahramian A., Arya S. "Influence of ZrO2 Nanoparticles including SDS and CTAB Surfactants Assembly on the Interfacial Properties of Liquid-Liquid, Liquid-Air and Liquid-Solid Surface Layers", *Journal of Nano Research*, 2013, pp. 15-21.
- [28] Cheraghian G., Hendraningrat L. "A review on applications of nanotechnology in the enhanced oil recovery part A: effects of nanoparticles on interfacial tension", *Int. Nano Lett.*, 2016.

Review of Kerogen Thermal Destruction Kinetics and Deconvolution Technique Application

Nikolai Mitiurev

Abstract - Within all unconventional resources, unmaturred kerogen seems to be the most promising one due to its enormous quantity. Kerogen is a solid-state insoluble polymeric organic matter with biogenic origin. There are several directions in kerogen research devoted to stages and details of its field development. In this paper, kerogen thermal destruction kinetics and use of deconvolution technique are discussed. It was found out that the accuracy of single reaction description is insufficient. While the multiple independent reactions with different activation energies approach cannot be used for mechanism investigations, its results can be applied in basin modeling [1].

Index Terms - Kerogen, Pyrolysis, Kinetics, Deconvolution technique.

I. NOMENCLATURE

	reaction rate (%w/s)
	reaction constant (-)
	concentration (mol/l)
	frequency factor (-)
E_A	activation energy(kJ/mol)
T	temperature ($^{\circ}\text{C}$)
t	time (s)
R	ideal gas constant ($\approx 8,31 \frac{\text{J}}{^{\circ}\text{K} \times \text{mol}}$)
α	conversion (%)
Δ	big amount of heat

II. INTRODUCTION

Nowadays, rapid depletion of conventional hydrocarbon resources on the one hand, and the absence of worthy alternatives on the other, have stimulated a lot of scientific investigations in search of new energy source. One of them could be unconventional oil and gas. Those resources have been known for quite a while, however their development was and still is inefficient in most cases [2].

Kerogen is one of the unconventional hydrocarbon resources. To obtain hydrocarbons from it, pyrolysis can be used. Pyrolysis is the reaction of thermochemical decomposition of organic substances at high temperature in the absence of oxygen. Due to the complexity of the process, deconvolution technique can be applied [3].

Mitiurev N.A. is from the Hydrocarbon Recovery Center, Skolkovo Institute of Science and Technology, Skolkovo Innovation Center, Building 3, Moscow 143026, Russia (e-mail: N.Mitiurev@skoltech.ru).

III. RESEARCH PAPER PREPARATION

A. Kerogen structure, types and maturation level

There are two main theories about kerogen complicated structure containing related aromatic and aliphatic fragments. The first one tells that there are polyaromatic "islands" with aliphatic chains between them, and the second one states that there is single huge polyaromatic structure with aliphatic chains growing from it. There is no leading theory of kerogen structure for this day and age. Anyhow, despite structural argument, there is a general consensus that kerogen has three types of origin and three stages of maturation, as illustrated in Figure 1:

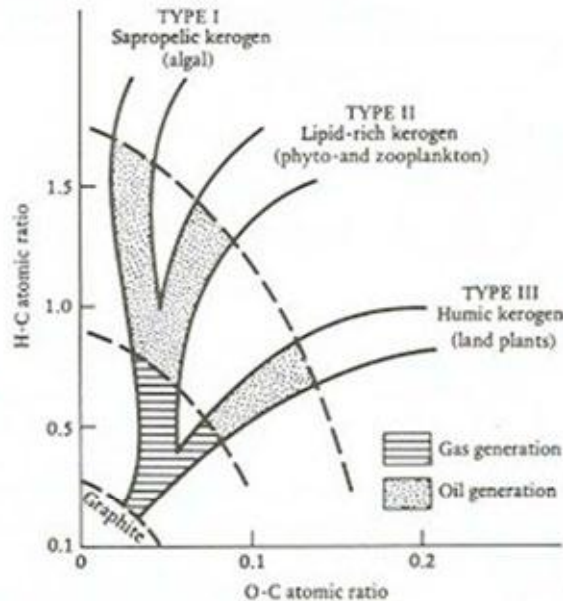


Fig.1. Van Krevelen diagram of kerogen maturation [4]

The types of origin are: sapropelic or first type kerogen (algal from lakes); lipid-rich or second type kerogen (phyto-and zooplankton of seas); and humic or third type kerogen from land plants [5].

Aside from that, there are also three main stages of kerogen maturation. Diagenesis represents the sum of all processes, chiefly chemical, by which changes occur in organic matter after its deposition but before its final lithification (conversion to rock). Example of unmaturred kerogen structure is given in Figure 2.



Fig.2. Unmaturred kerogen [4]

The second stage is called catagenesis, which continues sedimentation processes. This is the phase of kerogen thermal destruction and hydrocarbons formation. At this stage, over time, aliphatic components split off and form oil and gas, while the remaining molecule becomes more and more aromatic. Kerogen structure during catagenesis is illustrated in Figure 3.

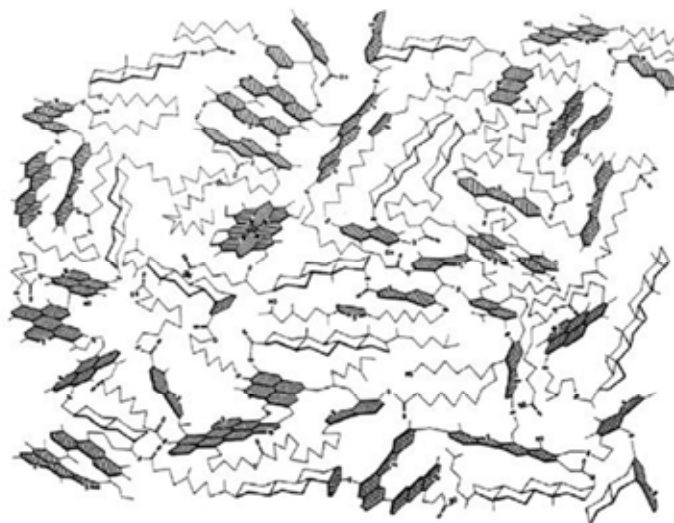


Fig. 3. Kerogen, going through decomposition processes [4]

The last one, preceding the final conversion to graphite is metagenesis stage. This is the phase of secondary metamorphic processes and mainly methane generation from kerogen. Kerogen structure (in Figure 4) is almost aromatic at this stage and in the end reaches graphite state.

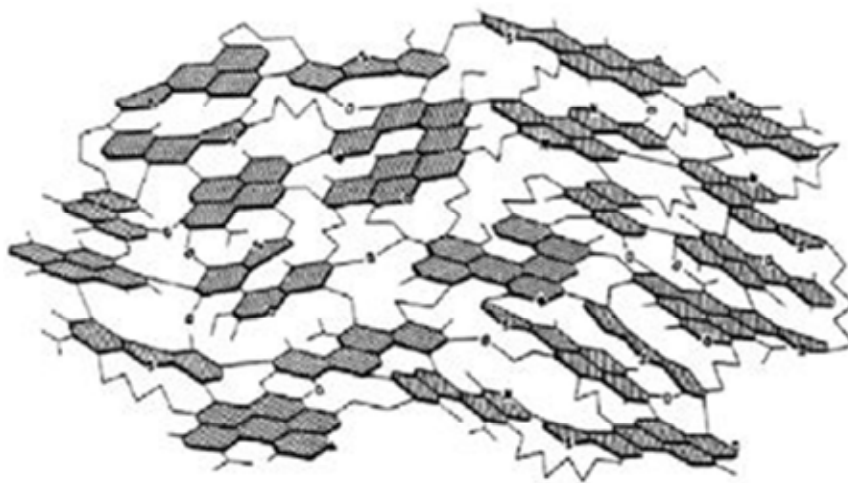


Fig. 4. Remaining structure with increased aromaticity [4]

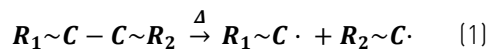
All three stages can be divided into subgroups according temperature level, depth of formation, carbon weight percentage, etc. The ones relevant for the current study relate to catagenesis. They are organized in three big stages: protocatagenesis (PC), mesocatagenesis (MC) and apocatagenesis (AC). We are particularly interested in PC 1-3 and MC 1-3 subgroups. They are devoted to unmaturred kerogen or one that has started to produce hydrocarbons kerogen within the so-called oil window [6]. All subgroups are presented in Table I.

Table I. Classification of kerogens.

Protocatagenesis	PC 1
	PC 2
	PC 3
Mesocatagenesis	MC 1
	MC 2
	MC 3
	MC 4
	MC 5
Apocatagenesis	AC 1
	AC 2
	AC 3
	AC 4

B. Kerogen pyrolysis reaction mechanism

First of all, mechanism of the reaction should be discussed. Assuming that there is no oxygen access to the place of kerogen sedimentation and that reaction goes because of energy transfer via heat, it was stated that the process of kerogen thermal destruction has radical mechanism [7]. Summing this with the knowledge about kerogen structure leads to the assumption that the first stage of the reaction is decomposition of C-C bond in aliphatic chain.



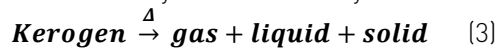
After that, there is a big row of different types of the following reactions: cyclization, condensation, hydrogenation, etc. They are difficult to analyze due to the complexity of the process, and thus reaction behavior cannot be predicted. However, because the first step is the rate-limiting one due to the radical type of the reaction, with good approximation, it is the only one that needs to be described. So, in theory, kerogen thermal destruction should be described with single chemical reaction. But, as experimental data shows, error, in this case, can be quite significant [8].

C. Kinetics theory

The main kinetics equation can be written as follows for a homogeneous liquid system:

$$r = \frac{dc}{dt} \quad (2)$$

In our case, kerogen is a solid substance, from which products of all states (gaseous, liquid and solid) are obtained. These products present a whole variety of oil-related hydrocarbons.



For such system reaction rate will be written with conversion level instead of concentration.

$$\frac{d[\mathbf{Kerogen}]}{dt} = \frac{d\alpha}{dt} = -kt = -Ae^{-\frac{E_a}{RT}} \quad (4)$$

Here, change of kerogen amount within time is also equaled to reaction constant k , which can be expressed via the Arrhenius equation:

$$k = Ae^{-\frac{E_a}{RT}} \quad (5)$$

A is frequency factor, which in our case means possibility of bond braking, and E_a is an activation energy, which means the energy required to start the reaction.

So, there are two unknowns (E_a and A) and because of that at least three experimental curves with different heating rates need to be obtained for stable solution of the Arrhenius equation. If the calculated curve does not match with the experimental one, two approaches can be used [9]. The first one is based on the use of several stages reaction. This approach can be realized in NETSCH program for instance. The second approach is to use deconvolution technique, which is discussed below.

D. Deconvolution technique

Deconvolution technique is an algorithm that divides initial spectrum to a row of smaller parts, the sum of which needs to match with the initial line. In the case of kerogen thermal destruction, this technique can be used as follows. Let us suppose that there is a number of "reactions" with certain activation energies. All of them are just single unrelated independent first order reactions, and for each of them reaction rate equation can be written. Thus, they all can be considered individually with their own level of conversion, but with the following requirement: the sum of their conversions must equal conversion of experimental graphs for any temperature. Comparison of experimental and calculated curves is shown on Figure 5.

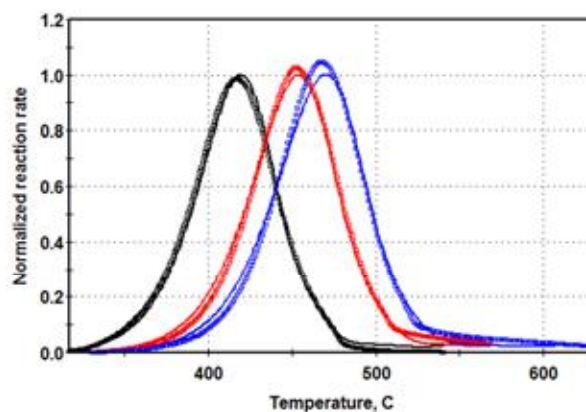


Fig. 5. Experimental (bold) and calculated (squares) curves

Since the number of variables after such operation increases significantly (instead of one activation energy there is a row of them), multiple solutions become possible. Therefore, there is a need for calculation control. Also it should be mentioned that these "reactions" do not have chemical or physical meaning. So, this is just a mathematical operation, which is the main drawback of this method. Yet, it can be used in prediction of probable conversion level under certain conditions (temperature and time of heating substance) [10].

Number of first-order independent reactions with discrete distribution was applied for the first time by Tissot and Espitalie, 1975 [11]. Distribution of activation energies looks like on the Figure 6.

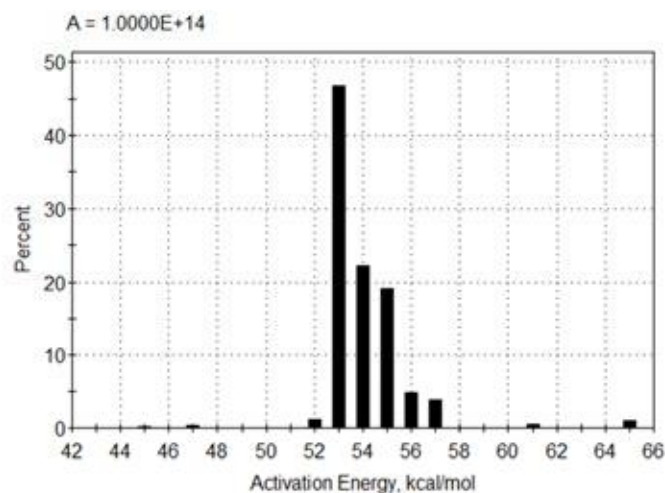


Fig. 6. Activation energy distribution

There is another approach with assumes that there is Gaussian or normal distribution of activation energies about concrete mean, firstly suggested by Pitt, 1961 [12]. In the case of normal distribution, it is defined by mean and standard deviation.

E. Conclusions

- 1) Kerogen thermal destruction is a complicated radical process with lots of uncertainties.
- 2) Since a simple first order reaction equation does not perfectly match experimental data, the error can be significant.
- 3) For a better match of theoretical curve with the experimental one, deconvolution technique can be used.
- 4) There is a need for calculation control due to evaluation volatility, since there is a possibility of multiple equation solutions.
- 5) Although data obtained by deconvolution of kinetic curves is not suitable for mechanism investigations, it can be used for kerogen pyrolysis conversion prediction, which is required for basin modeling.

IV. REFERENCES

- [1] Aboulkas A., Harfi K. "Study of the kinetics and mechanisms of thermal decomposition of Moroccan Tarfaya oil shale and its kerogen", *Oil Shale*, 2008, 25, pp 426-443
- [2] Rezace R. "Petroleum geology", Alavi Publications, 2002, p. 479
- [3] Sert M., Ballice L., Yuksel M., Saglam M. "The effects of acid treatment on the pyrolysis of Goynyk oil shale (Turkey) by thermogravimetric analysis", *Oil Shale*, 2012, 29, pp 51-62
- [4] Vandenvroucke M., Largeau C. "Kerogen origin, evaluation and structure", *Organic Geochemistry*, 2007, 38, pp 719-833
- [5] Nady M., Ramadan F.S., Hammad M.M., Lofty N.M. "Evaluation of organic matters, hydrocarbon potential and thermal maturity of source rocks based on geochemical and statistical methods: Case study of source rocks in Ras Gharib oilfield, central Gilf of Suez, Egypt", *Egyptian Journal of Petroleum*, 2015, 24, pp. 203-211
- [6] Vandenvroucke M. "Kerogen: from types to models of chemical structure", *Oil & Gas Science and Technology*, 2003, 58, pp 243-269
- [7] Pepper A.S., Corvi P.J. "Simple kinetic models of petroleum formation. Part I: oil and gas generation from kerogen", *Marine and Petroleum Geology*, 1995, 12, pp 291-319
- [8] Espitalie J., Ungerer P., Irwin I., Marquis F. "Primary cracking of kerogens. Experimenting and modeling C₁, C₂-C₅, C₆-C₁₅, and C₁₅+ classes of hydrocarbons formed", *Advances in Organic Geochemistry*, 1987, 13, pp 893-899
- [9] Pepper A.S., Dodd T.A. "Simple kinetic models of petroleum formation. Part II: oil-gas cracking", *Marine and Petroleum Geology*, 1995, 12, 321-340
- [10] Vyazovkin S., Burnham A.K., Criado .M., Perez-Maqueda L.A., Popescu C., Sbirrazzuoli N. "ICTAC Kinetics committee recommendations for performing kinetic computations on thermal analysis data", *Thermochimica Acta*, 2011, 520, pp 1-19
- [11] Tissot B.P., Espitalie J. "L'évolution de la matière organique des sédiments: application d'une simulation mathématique", *Rev. Inst. Fr. Petrol*, 1975, 30, 743-777
- [12] Pitt G.T. "on the depth, time and mechanism of petroleum generation", *Geochim. Cosmochim. Acta*, 1965, 29, 1021-1049

Prevention of Folding Processes in Conjugated Polymer Chains: Techniques and Structures

A. Naumov

Abstract - Folding of polymer chains in conjugated polymer-based materials is often considered as undesirable process because it can cause crystal structure defects, leading to decrease in charge carrier mobility of the material. The present review covers techniques used for prevention of folding and possible strategies for orientation control of unfolded chains.

Index Terms - Conjugated polymers; folding; organic electronics

I. INTRODUCTION

From industrial point of view, control of the morphology of conjugated polymer systems is important for altering device properties and increasing its performance. It has been observed experimentally and in calculations, that long polymer chains tend to self-folding [1]. In case of a crystallite, it can lead to the so-called lamellar structure (Fig. 1), while inside amorphous regions and in solution, polymer chains may form highly disordered randomly folded chunks. Moreover, folding process seems to provoke lesser level of crystallinity of polymer bulk samples [2], which is usually undesirable.

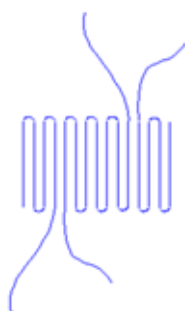


Fig. 1. Scheme of a lamellar layer, adopted from [1]

The question of polymer folding is closely related to self-assembly processes in polymer films, and polymer structure engineering. In the following short review we will summarize some existing approaches to polymer folding control and will speculate on their industrial applications.

A. Naumov is with the Center of Electrochemical Energy Storage, Skolkovo Institute of Science and Technology, Skolkovo Innovation Center, Building 3, Moscow 143026, Russia [e-mail: artem.naumov@skolkovotech.ru].

II. APPROACHES TO FOLDING MITIGATION

A. Folding control parameters

The parameters controlling chain folding are the following:

1. Molecular weight, or chain length
2. π - conjugation
3. Weak forces, non-bonded interactions.

It is known for well-studied polymer systems, that every particular polymer has its own conjugation length, related to delocalization of π - orbitals along the backbone. For example, for regioregular poly (3-hexylthiophene) (P3HT) conjugation length is equal to 8 monomers [3]. So, on some length of the backbone, this mechanism is sufficient to maintain backbone planarity and prevent it from folding. However, with the increasing number of monomers, van-der-Waals forces start to prevail, making folded structure energetically more favorable. In the case of P3HT, this equals to over 20 monomers in the backbone [4].

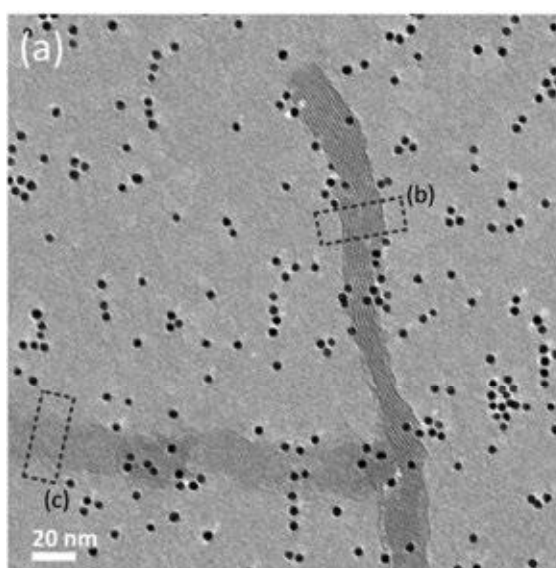


Fig. 2. Cryo-TEM image of two P3HT nanowires with different orientations, adopted from [1].

These considerations are only true if one chain is being considered. In a crystal form, π -stacking intermolecular interaction mechanism increases rigidity of the backbone, leading to highly ordered structures called "nanowires" (Fig. 2).

B. Side chain functionalization

One solution to the folding problem is self-assembling layers of polymer chains. In this scheme, side chains of a polymer are functionalized in a way that ends of these chains, belonging to different molecules, interact with each other [2]. These leads to a specific self-assembling structure resistable to folding (see Fig. 3). Selected functional groups enable face-on or edge-on orientation correspondingly.

C. Polymer chain isolation

Another interesting approach is isolation of separate polymer chains with small molecules in solution.

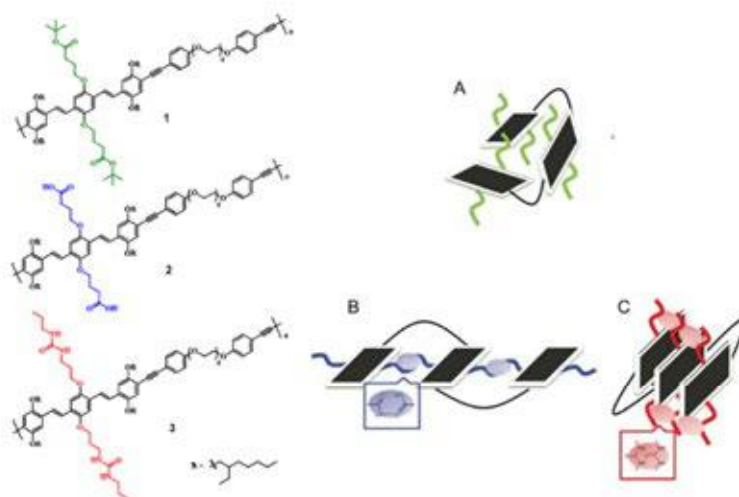


Fig. 3. Polymers with no H-bonding(1)and H-bonding capable polymers containing carboxylic acids(2)and urea(3) groups. Corresponding packing structures are marked with letters A-C on the right. Adopted from [2].

This not only prevents a polymer from aggregation, but also allows studying single rod-like molecules with experimental techniques [5]. In one of the examples cationic polythiophene is used in a composite solution with various kinds of bile acid to achieve polymer backbone isolation effect (Fig. 4).

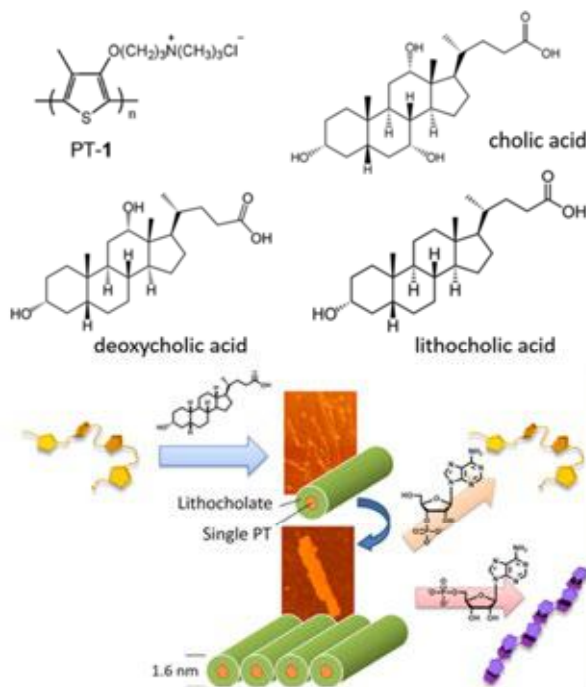


Fig. 4. Cationic polythiophene and bile acid small molecules used in experiment, adopted from [5].

D. Top-down approaches

While the two ways of structure control described above employ the so-called bottom-up approach, assuming use of intra-molecular assembling, there are approaches using prefabricated templates or lithography (top-down approach) [6]. Perforated hard templates, such as anodic aluminum oxide, can be used for controlled polymerization of high-ordered structures from monomer solution of P3HT. Graphitic surfaces demonstrate an ability to attach conjugated polymers via strong $\pi - \pi$ interaction [6]. Another way to decrease folding while

increasing conjugation length along the backbone is to use nano-grooved substrates. As an example, a polymer drop-casted onto Si grooved substrate shows increased structural ordering and increased charge carrier mobility [7].

III. CONCLUSIONS

We have reviewed five possible approaches to polymer chain folding prevention, in semi-crystalline form and in solution. In case of polymer #3 (Fig. 3), we must definitely get a stable structure preventing chain folding, due to two effects: vdW interaction between side chains, and strong π -stacking between the backbones. Our idea is that the proposed functional side chains can be in principle combined with another polymer backbone, so that we get hundreds of polymers structure of which can be verified computationally. In addition, this approach can potentially lead to a discovery of even better functional groups for side-chain-induced self-assembly. The industrial applications of the considered approaches are numerous. To name some, graphitic surfaces and template approach can lead to a better (or close to ideal) ordering of donor-acceptor domains in organic solar cells, which in turn will get increased electronic properties. The nano-grooved substrates, graphitic surfaces, and templates have shown great potential for organic field effect transistor design. Isolation approach for cationic polythiophene has shown the strongest shift in absorbance spectra of P3HT in solution (unique red P3HT); this can find applications in optoelectronic devices. Complex approach, combining described options, can lead to even better device performance and improved production techniques.

IV. ACKNOWLEDGMENT

I would like to thank my scientific adviser prof. A. Zhugayevych for his constant attention to my work, his patience in helping me with various issues that so very often hamper my way to high peaks of science. I also wish to thank prof. Pavel Troshin, our Organic Electronic course instructor, for providing me with an idea for the above review.

V. REFERENCES

- [1] Maarten J. M. Wirix, Paul H. H. Bomans, Heiner Friedrich, Nico A. J. M. Sommerdijk, and Gijsbertus de With. Three-Dimensional Structure of P3HT Assemblies in Organic Solvents Revealed by Cryo-TEM. *Nano Letters*, 14(4):2033–2038, apr 2014.
- [2] Beiyue Shao, Xinju Zhu, Kyle N. Plunkett, and David A. Vanden Bout. Controlling the folding of conjugated polymers at the single molecule level via hydrogen bonding. *Polym. Chem.*, 8(7):1188–1195, 2017.
- [3] Ram S. Bhatta, Yeneneh Yimer, David S. Perry, and Mesfin Tsige. Improved Force Field for Molecular Modeling of Poly(3-hexylthiophene). *The Journal of Physical Chemistry B*, 117(34):10035–10045, aug 2013.
- [4] Orestis Alexiadis and Vlasios G. Mavrantzas. All-Atom Molecular Dynamics Simulation of Temperature Effects on the Structural, Thermodynamic, and Packing Properties of the Pure Amorphous and Pure Crystalline Phases of Regioregular P3HT. *Macromolecules*, 46(6):2450–2467, 2013.
- [5] Youichi Tsuchiya, Takao Noguchi, Daisuke Yoshihara, Bappaditya Roy, Tatsuhiro Yamamoto, and Seiji Shinkai. Conformation Control of a Conjugated Polymer through Complexation with Bile Acids Generates Its Novel Spectral and Morphological Properties. *Langmuir*, 32(47):12403–12412, 2016.
- [6] Lei Zhai, Saiful I. Khondaker, Jayan Thomas, Chen Shen, and Matthew McInnis. Ordered conjugated polymer nano- and microstructures: Structure control for improved performance of organic electronics. *Nano Today*, 9(6):705–721, 2014.
- [7] Hsin-Rong Tseng, Hung Phan, Chan Luo, Ming Wang, Louis Perez, Shrayesh Patel, Lei Ying, Edward Kramer, Thuc-Quyen Nguyen, Guillermo Bazan, and Alan Heeger. High-Mobility Field-Effect Transistors Fabricated with Macroscopic Aligned Semiconducting Polymers. *Advanced Materials*, 24:2993–2998.

Status of Nanoindentation Testing in Shales

Evgeny Shilov

Abstract - Nanoindentation Testing (NIT) technique is a method that has found its application in petroleum industry as a method for determining geomechanical properties at very small scales. It was developed in the last decades, but before shales revolution there was a lack of interest of its usage in the industry. Just recently the situation has been changed, and this paper provides an update of the status of nanoindentation testing method in shale rocks. The following topics are covered: principles, existing results, problems, future plans.

Index Terms - Nanoindentation testing; shale; kerogen; mechanical properties

I. NOMENCLATURE

NIT	Nanoindentation Testing
TOC	Total Organic Carbon
XRD	X-ray diffraction
AFM	Atomic Force Microscope
<i>E</i>	Young's Modulus (MPa)
<i>v</i>	Poisson's Ratio (-)
<i>P</i>	The indenter load
<i>h</i>	The elastic displacement of the indenter
<i>α</i>	Constant value related to the geometry of the indenter
<i>m</i>	Constant value related to the geometry of the indenter
<i>S</i>	The stiffness
<i>A</i>	The projected area of elastic contact
<i>E_r</i>	The reduced modulus
<i>E_{NI}</i>	The indentation modulus
<i>H</i>	The hardness
<i>P_{max}</i>	The maximum load

II. INTRODUCTION

Today petroleum industry has a great interest in developing unconventional resources that are mainly presented by heterogeneous rocks that are basically called shales. Geomechanical properties play a big role in the development of shales. They can be used in drilling, fracturing or seismic interpretation operations [1]; or in simulations where it is necessary to know these properties and only in these case simulation's results will be matched with reality. The common methods for determining geomechanical properties were developed long

E. Shilov is with the Center of Hydrocarbon Recovery, Skolkovo Institute of Science and Technology, Skolkovo Innovation Center, Nobel 3, Moscow 143026, Russia (e-mail: evgeny.shilov@skolkovotech.ru).

ago, they are usually presented by conventional techniques like unconfined compression test, semi- or true-triaxial test, Brazilian or tension test, etc. Unfortunately, it is very difficult to use these experimental methods due to the mechanical instability of shales; conventional techniques for determining geomechanical properties lead to unreliable results for shales. It is also very unlikely to retrieve large core samples from highly heterogeneous and unconsolidated shales. To develop methods for determining mechanical properties of shales, researchers are constantly trying to employ newly developed techniques from other fields in petroleum geomechanics or to develop their own techniques for determining geomechanical properties. Because of the rock heterogeneity of shales, researchers mainly require methods that work on much smaller scales than conventional techniques.

From the early 70s, different researchers revealed their interest in sensing indentation testing for elastic modulus measuring. In [2], the authors describe nanoindentation testing (NIT) technique that allows geomechanical properties detection on the submicron scale on different materials. This method uses a high-resolution electronic instrument to measure applied loads and value of displacement of an indenter [3] and a schematic diagram of the nanoindenter is presented on the Figure 1. It allows us to calculate Young's modulus and hardness of the sample from load-displacement recording. A small size of the sample and very small load are used in this type of the test, and therefore the indentation area is about a few nanometers.

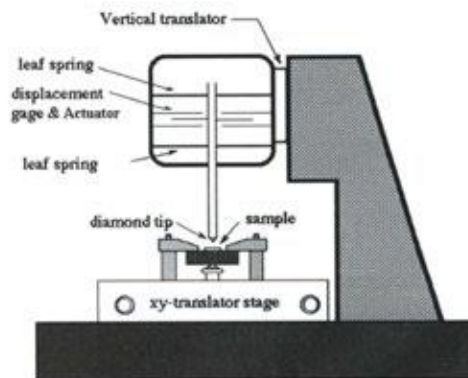


Fig. 1. A schematic diagram of the nanoindenter [4].

Additional attention should be applied to the term "shales". This term in that review means petroleum plays that are rich with organic matter. Therefore, shales consist of mineral matrix and organic matter that is kerogen. The kerogen is the most valuable component in the rock because it is the hydrocarbon generation. As it was mentioned above shales are very heterogeneous rocks; and geomechanical properties of separate rock components cannot be measured conventionally at big scales. But using NIT it is possible to work at nanoscales and measure geomechanical properties of either mineral matrix or kerogen, or even the rock composition as it is.

III. PRINCIPLES

Special indentation instruments can continuously measure force and displacement of the indenter. The indentation load-displacement data of the test can be used to determine geomechanical properties (Figure 2). It is possible to retrieve two mechanical properties from indentation testing: the elastic modulus, E , and the hardness, H . Commonly the data are obtained from one complete cycle of loading and unloading [2]. General relationships were derived from the load, displacement, and contact area for any punch (indentation, print) that can be described as a solid of revolution of smooth function [2]. The load-displacement relationships for many simple punch geometries can be conveniently written in the following form:

$$P = \alpha h^m \quad (1)$$

where P is the indenter load, h is the elastic displacement of the indenter, and α and m are constants. Values of the exponent m for some common punch geometries are $m=1$ for flat cylinders, $m=2$ for cones, $m=1.5$ for spheres in the limit of small displacements, and $m=1.5$ for paraboloids of revolution.

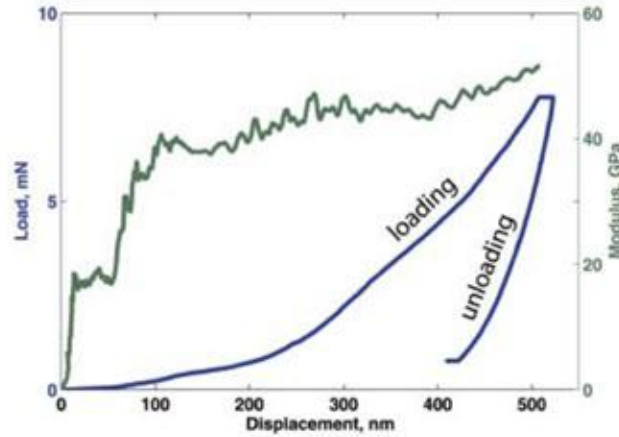


Fig. 2. Load versus displacement data for one indentation (in blue). Reduced modulus versus displacement data for the same indentation (in green) [5].

Tabor and Stillwell [6] conducted the earliest experiments of load and displacement sensing indentation for measuring mechanical properties. They proved that the shape of the entire unloading curve and the total amount of recovered displacement can be related to the elastic modulus and the size of the contact impression. Another important observation resulting from these studies is about effect of non-rigid indenter on the load-displacement behavior is accounted for by the use of a reduced modulus, E_r , through the equation

$$\frac{1}{E_r} = \frac{1 - \nu^2}{E} + \frac{1 - \nu_i^2}{E_i} \quad (2)$$

where E and ν are Young's modulus and Poisson's ratio for the specimen and E_i and ν_i are the same parameters for the indenter.

According to [2], physical properties determination from nanoindentation experiments involves analysis of the generated load-displacement curves. The upper portion of the unloading data is fit to a power of law. The slope of the initial portion of this fit determines the stiffness, S ($= \frac{dP}{dh}$, where P is the load and h - the displacement). The experimentally measured stiffness, S , and the projected area of elastic contact, A , are used to determine the reduced modulus, E_r , according to the equation

$$E_r = \frac{S \sqrt{\pi}}{2 \sqrt{A}} \quad (3)$$

Unfortunately, there is no data in the literature for Poisson's ratio of kerogen. Therefore, all elastic modulus can be presented in a form of indentation modulus:

$$E_{NI} = \frac{E}{1 - \nu^2} \quad (4)$$

Values of indentation modulus can be used to calculate a Young's modulus for kerogen if the knowledge of the Poisson's ratio becomes available.

The hardness, H , is defined as the mean pressure the material will support under load, and is computed from

$$H = \frac{P_{max}}{A} \quad (5)$$

where P_{max} is the maximum load.

General experimental layout of any NIT has loading and unloading stage. Figure 3 presents the example plot of applied load via nanoindenter with time.

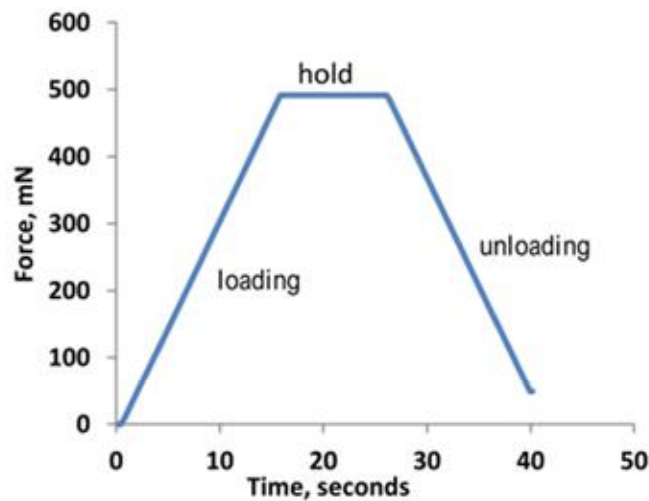


Fig. 3. Plot of variation of applied load with time. Increase in load represents loading part while decrease represents unloading part; a constant force segment is used to study creep on material [7].

IV. EXISTING RESULTS

In [8], nanoindentation was a technique used to measure mechanical properties of kerogen. Elastic properties were measured both parallel and perpendicular to the bedding plane. No detectable anisotropy in kerogen mechanical properties was found.

In [9], NIT was used on 10 Woodford outcrop shale samples to calculate elastic properties. More than 3000 indentation tests were conducted. Figure 4 gives an example of the load-displacement curve which allows the extraction of the indentation moduli [2]. X-ray diffraction (XRD) mineralogy data of these samples showed quartz content varying from 27 to 53 % of volume, clay content ranging from 18 to 43 % of volume, kerogen content varying from 11 to 18 % of total weight, and porosity ranging from 0.16 to 0.19 fraction volume. Indentations were done both parallel and perpendicular to the bedding plane. They exhibited low range of Young's moduli because the sample might have been weakened due to chemical weathering at shallow depth.

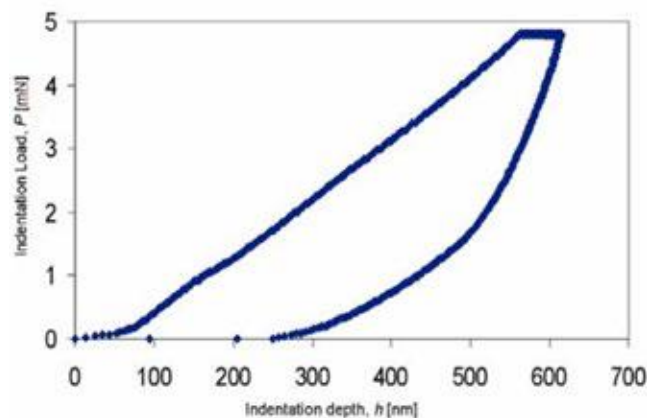


Fig. 4. Load displacement curve when indenting in direction to bedding plane [9].

Samples used in [2], [9] studies showed total organic carbon (TOC) content of 22% of total weight and maximum temperature of 421°C. They indicated that Young's modulus of shale has an inverse relationship with TOC content. Researchers measured hardness and indentation modulus on three orthogonal faces of shale sample cube and reported no evidence of anisotropy in the mechanical properties of kerogen.

Other researchers performed nanoindentation measurements on a sample from organic-rich Bazhenov formation from 3800 m depth showing kerogen content in the range of 7–21% of volume [5]. All imaging and

measurements were done orthogonal to the horizontal bedding plane. They calculated Young's modulus of organics in the range of 10–15 GPa.

In [10], authors conducted nanoindentation measurements on a total number of 144 organic-rich shale samples. Measurements were performed on different types of shales. It was concluded that:

- Woodford samples have a Young's modulus of 23–80 GPa. Samples with lower E values (23–30 GPa) show either high concentration of TOC or high clay content; whereas samples with higher E values (60–80 GPa) show relatively low TOC, porosity, and clay content. Hardness of this formation vary from 0.54 to 7.2 GPa and show higher hardness values (6–7 GPa) due to high quartz content and low TOC and porosity values.
- Barnett samples have a Young's modulus of 39–78 GPa, while higher E values are found to be either relatively low in TOC and porosity, or high in carbonate content.
- Haynesville samples have a Young's modulus of 31–79 GPa where samples with higher E is found to be either high in carbonate or low in TOC. Hardness for Haynesville samples with average value of 1.1 ± 0.6 GPa is attributed to the high carbonate content of samples.
- Eagle Ford samples have a Young's modulus of 31–57.5 GPa. Samples with higher carbonate content exhibit higher Young's moduli. Hardness of these samples obtained is between 0.45 and 1.5 GPa.
- Ordovician shale samples with high average carbonate content of 73 ± 4 % of total weight show Young's modulus of 49–57 GPa. They show a hardness range from 1 to 1.3 GPa.

Kumar et al. [10] indicate that for all shale plays, samples with high TOC and high porosity exhibit low Young's modulus, whereas samples with low TOC, low porosity, and high carbonate content show high Young's modulus values. Hardness on the other hand shows negative correlation with porosity and clay content as well as poor correlation with TOC.

V. PROBLEMS

There is no reliable value for Poisson's ratio, ν , in the literature for the shales. Thus, researchers in their calculations need to use ν obtained from large scale measurements. Fortunately, an uncertainty of ± 0.1 in the Poisson's ratio leads only to 5% difference in the calculated Young's modulus for the predefined indentation modulus [11].

The relationship between indentation and Young's modulus is valid only if Poisson's ratio is obtained from the same scale; in the case of nanoindentation technique there is no independent values for Poisson's ratio obtained at the nanoscale. Because of that researchers should think about techniques and methods that will be able to get more reliable values for Poisson's ratio at nanoscale in order to calculate much more representative Young's modulus with the help of nanoindentation data.

It is also should be mentioned that nobody measured geomechanical properties of shales under non-contact regime with AFM in the examined papers. This regime can probably help to avoid the time consuming point measuring by traditional NIT technique.

VI. CONCLUSIONS AND FUTURE PLANS

Despite significant research into the physical behavior of shales, fundamental questions remain regarding how the intrinsic rock properties of the organic fraction affect the macroscopic shales properties overall. We still do not have a clear picture of the elastic properties of either the organic matter or the individual clay minerals that are presented in shales [5].

According to [9], [11], nanoindentation tests can help in building a special model that will be able to determine mechanical shale properties based on just a few intrinsic rock properties like porosity, packing density and mineralogy. Probably, NIT will replace a very costly core sample operation by nanoindentation measurement on very tiny drill cuttings obtained during drilling operations [10], [12]–[14].

It is very important to understand the relationship of nanometer-scale properties of shales to their macroscopic properties and this is one of the current challenges in petroleum geomechanics that should be solved [9].

Future studies should examine different sets of samples from different organic-rich rocks, as well as elastic properties of all other minerals that rock is composed with. In our future research, we consider using AFM equipment in order to check the viability of measuring geomechanical properties with non-contact mode and create a map of geomechanical properties for different compounds of the shale samples. And we should think about the possibilities to measure and obtain Poisson's ratio at nanoscales for correct Young's Modulus calculation.

VII. REFERENCES

- [1] R. S. oglu Ahmadov, "MICROTEXTURAL, ELASTIC AND TRANSPORT PROPERTIES OF SOURCE ROCKS," 2011.
- [2] W. C. Oliver and G. M. Pharr, "An improved technique for determining hardness and elastic modulus using load and displacement sensing indentation experiments," *J. Mater. Res.*, vol. 7, no. 6, pp. 1564–1583, 1992.
- [3] J. Hay and G. Pharr, "ASM-handbook-nanoindentation.pdf," in *Instrumented Indentation Testing*. ASM Handbook., ASM International., 2000, pp. 232–243.
- [4] C. P. Bobko, "Assessing the Mechanical Microstructure of Shale by Nanoindentation: The Link Between Mineral Composition and Mechanical Properties," 2009.
- [5] R. Ahmadov, T. Vanorio, and G. Mavko, "Confocal laser scanning and atomic-force microscopy in estimation of elastic properties of the organic-rich bazhenov formation," *Lead. Edge*, vol. 28, no. 1, pp. 18–23, 2009.
- [6] N. A. Stilwell and D. Tabor, "Elastic Recovery of Conical Indentations," *Proc. Phys. Soc.*, vol. 78, no. 2, pp. 169–179, 1961.
- [7] V. Kumar, C. H. Sondergeld, and C. S. Rai, "Nano to Macro Mechanical Characterization of Shale," in *SPE Annual Technical Conference and Exhibition*, 2012, no. October, pp. 8–10.
- [8] J. C. Zeszotarski, R. R. Cromik, R. P. Vinci, M. C. Messmer, R. Michels, and J. W. Larsen, "Imaging and mechanical property measurements of kerogen via nanoindentation," vol. 68, no. 20, pp. 4113–4119, 2004.
- [9] Y. Abousleiman, M. Tran, and S. Hoang, "Geomechanics Field and Laboratory Characterization of Woodford Shale: The Next Gas Play," in *SPE Annual Technical Conference and Exhibition*, 2007.
- [10] V. Kumar, M. E. Curtis, N. Gupta, C. H. Sondergeld, and C. S. Rai, "Estimation of Elastic Properties of Organic Matter and Woodford Shale Through Nano-indentation Measurements," in *SPE Canadian Unconventional Resources Conference*, 2012.
- [11] W. Li and A. Sakhaee-Pour, "Macroscale Young's Moduli of Shale Based on Nanoindentations," vol. 57, no. 6, pp. 597–603, 2016.
- [12] M. De Block, A. Hofmann, C. Rigollet, J. Ravestein, and S. G. S. Horizon, "A New Solution for the Characterization of Unconventional Shale," 2015.
- [13] K. Glover, A. Cui, J. Tucker, T. Bozarth, and S. Pyper, "The Use of Measurements Made on Drill Cuttings to Construct and Apply Geomechanical Well Profiles," in *50th US Rock Mechanics / Geomechanics Symposium*, 2016.
- [14] P. Shukla, V. Kumar, M. Curtis, C. H. Sondergeld, and C. S. Rai, "Nanoindentation Studies on Shales," *47th US Rock Mech. Symp.*, no. January 2013, pp. 1194–1203, 2013.

Towards Quantum Simulation of High-Temperature Superconductivity with Ultracold Atoms in Optical Lattices

Andrei E. Tarkhov

Abstract - In the present review, the problem of quantum simulation of high-temperature superconductivity with ultracold atoms in optical lattices is addressed. A brief introduction to the challenges of quantum many-particle strongly interacting systems, such as high-temperature cuprate superconductors, and of their simulation is presented. A few state-of-the-art quantum simulators on ultracold atoms in optical lattices for the physical problems related to high-temperature superconductivity are considered. These prospective quantum simulators are designed for the following quantum problems: a quantum transition from the Mott insulator phase to the superfluid phase, a quantum transition from antiferromagnetic to paramagnetic ordering with an external magnetic field applied and investigation of fermion transport properties for non-interacting and interacting atomic clouds.

Index Terms - high-temperature superconductivity; quantum simulation; ultracold atoms in optical lattices.

I. NOMENCLATURE

The following quantities and operators will be frequently used in this review.

T_c	critical temperature for superconductivity (K)
\hat{a}_j	annihilation operator
\hat{a}_j^+	creation operator
\hat{n}_i	number of particles operator ϵ_i
ϵ_i	on-site potential
J	hopping parameter
U	on-site interaction parameter
S_z^i	z -component of spin i
h_z^i	z -component of magnetic field at site i
S_x^i	x -component of spin i
h_x^i	x -component of magnetic field at site i

II. INTRODUCTION

High-temperature superconductivity was originally discovered in 1986 by Bednorz and Müller in Ba-La-Cu-O [1] at a critical temperature $T_c = 30\text{K}$. Extensive research has been done since then to find new compounds with even higher T_c in this class of materials called cuprates. Quite a few new classes of high-temperature

This work was supported in part by Skolkovo Institute of Science and Technology.

Corresponding author.

A. E. Tarkhov is with the Center of Photonics and Quantum Materials, Skolkovo Institute of Science and Technology, Skolkovo Innovation Center, Building 3, Moscow 143026, Russia (e-mail: andrey.tarkhov@skoltech.ru).

superconductors (HTSC) have been also found. The highest temperature achieved to date in cuprate superconductors is **133K** in $\text{HgBa}_2\text{Ca}_2\text{Cu}_3\text{O}_x$ (HBCCO) [2], whereas the current record is **203K** in H_2S at **150 GPa** pressure [3]. The discovery of room-temperature superconductivity would revolutionize the whole electric power industry, science and technology, since it would make transmission losses almost negligible, allow the production of electromagnetic sensors of vastly increased sensitivity and give an opportunity to create magnetic fields of utmost intensity inexpensively for practical applications in magnetic resonance imaging (MRI), high-energy physics and nuclear fusion [4].

Despite the anticipated benefits of room-temperature superconductors and scientific endeavors to find them, the general theory and practical recipes for searching new HTSC are yet to be proposed. One of the main limitations is that most of the HTSC are unconventional superconductors, i.e. they cannot be well-described by the conventional Bardeen-Cooper-Schrieffer (BCS) theory of superconductivity [5], which predicts the highest possible critical temperature to be approximately **30K**. Due to the complex multilayered structure of cuprate superconductors and strongly interacting behavior of electrons within them, any reasonable theory would have to describe these strong interactions, thus making it very difficult to apply in practice. Since such theories are almost never analytically solvable, one would have to employ numerical methods. However, there is a practical obstacle for direct numerical simulation of such quantum interacting systems.

For such quantum many-particle strongly interacting systems as unconventional superconductors, the required memory and time to simulate their behavior on a classical computer would scale exponentially with the system size and number of particles involved. Classical computing has been successfully applied as a method to solve many a problem in physics since its invention, but for quantum problems with a few tens of interacting particles, the resources would be quickly exhausted.

Quantum computing was proposed as a remedy for this incredible complexity [6]–[8]. However, rapid decoherence of large groups of quantum bits — building blocks of a quantum computer — due to interactions with the environment is a limiting factor for quantum computing performance for the time being.

Quantum simulation is a compromise between universal quantum and classical computing. Quantum simulators, due to their quantum nature, exploit exponential gain in performance in comparison to classical computers, yet they lack universality [9]–[11]. Therefore, quantum simulators are problem specific and for each quantum calculation, a new quantum simulator should be designed. The main idea behind quantum simulation is to create a controllable quantum system, which would effectively model the Hamiltonian of a desired quantum system, which is for some reason unachievable or uncontrollable experimentally.

One of the most common and well-studied physical systems currently used for quantum simulation is ultracold gases in optical lattices, due to its high experimental controllability and a broad range of experimental detection possibilities [12]–[16]. Since ultracold gases in such setting are usually neutral, there is no rigid limit for the scaling of their size. Thus, such a quantum simulator can easily outperform any contemporary classical computer if the number of particles involved is higher than roughly 50.

This review is focused on the state-of-the-art applications of quantum simulators on ultracold atoms in optical lattices to the physical problems and models related to high-temperature superconductivity. The structure of this review is the following. In Section III a brief introduction into ultracold atoms in optical lattices is provided. Three quantum simulators are considered in the subsequent sections for: a quantum transition from the Mott insulator phase to the superfluid phase in Section IV; a quantum transition from antiferromagnetic to paramagnetic ordering with an external magnetic field applied in Section V; investigation of fermion transport properties for non-interacting and interacting atomic clouds in Section VI.

III. ULTRACOLD ATOMS IN OPTICAL LATTICES

Ultracold atoms in optical lattices have been thoroughly studied recently [12]–[16], which led to their practical applications for solving many a problem in physics.

To prepare such a system, one has to trap a cloud of neutral atoms and cool it down to temperatures of the order of several mK via laser cooling. And then lower the temperature to μK via an evaporating cooling

technique, i.e. slow lowering of the trap potential depth. An optical lattice formed by a standing wave of a laser light creates a periodic potential for trapped atoms similar to the one in condensed-matter physics for electrons. Thus, it can be considered as a way to create well-controllable artificial crystals with almost any desired properties.

Ultracold atoms in optical lattices allow modelling many a Hamiltonian, which is widely used in the modern condensed-matter physics.

The applications of ultracold atoms to the problems related to high-temperature superconductivity are considered below.

IV. TRANSITION FROM MOTT INSULATOR TO SUPERFLUID

The parent compound for cuprate superconductors is a Mott insulator. Mott insulators should have been conductive according to the conventional band theory (their conduction band is half-filled), but in practice they are insulators because of strong electron-electron repulsion. Superconductivity emerges only after the destruction of the Mott insulator with doping [17]. The Mott insulator phase and particularly the transition to the superconductive phase have attracted lots of attention.

For example, quantum phase transition from the Mott insulator phase to the superfluid phase at zero temperature in a system of bosonic particles with repulsive on-site interaction was studied with the help of ultracold atoms in optical lattices [18]. Classical phase transitions are forbidden at zero temperatures because all thermal fluctuations are frozen out, but for quantum systems quantum fluctuations are always present and phase transitions can occur even at zero temperature.

For the quantum simulation of such a transition the Bose-Hubbard model Hamiltonian was chosen:

$$H = -J \sum_{\langle ij \rangle} \hat{a}_i^\dagger \hat{a}_j + \sum_i \epsilon_i \hat{n}_i + \frac{1}{2} U \sum_i \hat{n}_i (\hat{n}_i - 1).$$

This equation consists of three terms: hopping between nearest-neighbor sites, on-site potential and on-site interaction term respectively. The effective hopping coefficient J was varied via changing the optical lattice potential depth V_0 . There was a critical value of the hopping parameter, where the quantum transition took place. If the hopping coefficient was higher than the critical one, the system was in the superfluid state, otherwise in the Mott insulator phase.

When the optical lattice has been released, and atoms have started to expand freely, time-of-flight experiments (TOF) allow measuring the momentum distribution of an atomic cloud. After a certain time of flight the density of atomic cloud will represent the momentum distribution of atoms at the moment of release [15]. In Fig. 1 the TOF measurement results for the quantum transition from the superfluid phase to the Mott insulator phase are presented. The images from b to d have intense interferometric maxima, showing the presence of long-range order in the system as well as coherence between neighboring lattice sites. From e to g the transition occurs and in g and h there is no long-range order anymore, i.e. the system is in the Mott insulator regime.

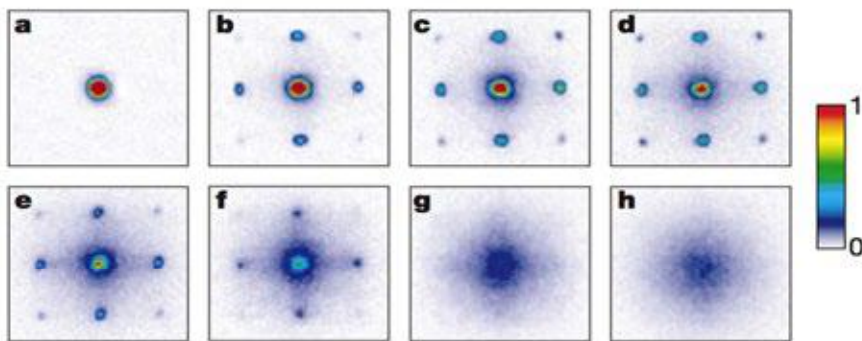


Fig. 1. Absorption images of multiple matter wave interference patterns. These were obtained after suddenly releasing the atoms from an optical lattice potential with different potential depths V_0 after a time of flight of 15 ms. Values of V_0 were: a, $0E_r$; b, $3E_r$; c, $7E_r$; d, $10E_r$; e, $13E_r$; f, $14E_r$; g, $16E_r$; and h, $20E_r$ [18].

Even though this quantum simulator is based on bosons, and fermions and their interactions are important for high-temperature superconductivity, this experiment still gives an opportunity to simulate the transition from Mott insulator to superfluid, which is one of significant aspects of the HTSC physics.

V. ANTIFERROMAGNETIC SPIN CHAINS

As previously mentioned, the parent compound for cuprate superconductors is in the Mott insulator phase, but in addition to that, this phase is also antiferromagnetically ordered [17]. This means that spins of electrons on neighboring sites tend to be pointing in opposite directions. Doping of a cuprate parent compound destroys the Mott insulator phase and antiferromagnetic ordering (AF) and gives rise to superconductivity [17].

Understanding of exotic magnetic phases is crucially important because the fundamental role of magnetism in high-temperature superconductors is already well-known. However, particular mechanisms of magnetic interactions leading to or preventing from the formation of the superconducting state are yet to be discovered. As with all other quantum many-particle problems, the simplest models of magnetism — spin chains, are rarely exactly solvable analytically. They also demand high amounts of memory and computing time to be dealt with. However, many of them could be easily modelled with a quantum simulator on ultracold atoms in optical lattices.

For example, one of the simplest model exhibiting a quantum phase transition is an antiferromagnetic Ising chain in one dimension in an applied magnetic field with the corresponding model Hamiltonian:

$$H = J \sum_i \mathbf{S}_z^i \mathbf{S}_z^{i+1} - h_z^i \mathbf{S}_z^i - h_x^i \mathbf{S}_x^i.$$

The first term in this Hamiltonian describes $\mathbf{z} - \mathbf{z}$ interactions between \mathbf{z} -components of neighboring spins \mathbf{S}_z^i and \mathbf{S}_z^{i+1} in the chain, whereas the second and the third terms introduce interaction with the \mathbf{z} and \mathbf{x} components of the external magnetic field \mathbf{h}^i .

This model was implemented in a quantum simulator on ultracold bosonic atoms (^{87}Rb) in a tilted optical lattice [19]. The authors of [19] managed to study a quantum phase transition from paramagnetic to antiferromagnetic phase and verify a formation of spin domains.

In Fig. 2 the zero-temperature phase diagram of this Hamiltonian is presented, where two phases: paramagnetic and antiferromagnetic, are separated by a second-order phase transition. In the regime of a dominant interaction term the ground state of the system is AF-ordered, whereas for relatively small interaction and high magnetic field intensities the ground state is paramagnetic. The transition becomes a classical first-order transition nearby the multicritical point $(h_z, h_x) = (1, 0)$.

To map the tilted bosonic Hubbard model to the spin model, the authors of [19] used the following scheme. The tilt of potential at each site leads to the possibility to realize two-dimensional optical lattice, which would mimic antiferromagnetic couplings in spin chains.

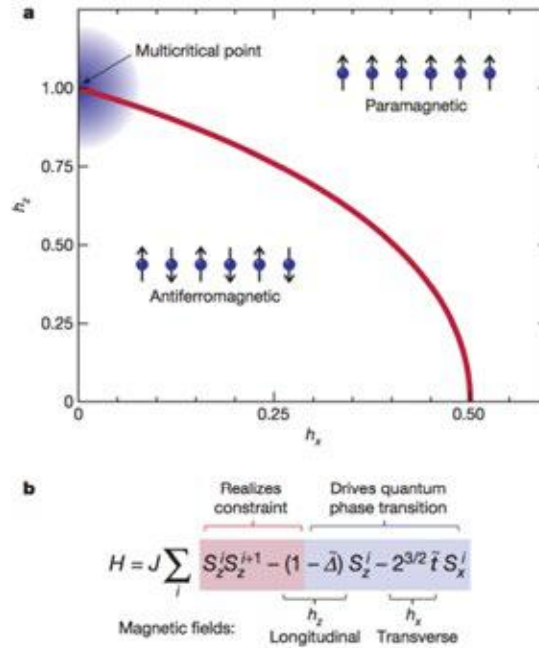


Fig. 2. Spin model and its phase diagram. a, An antiferromagnetic one-dimensional Ising chain in longitudinal (h_z) and transverse (h_x) magnetic fields exhibits two phases at zero temperature [20], [21]: an antiferromagnetic phase in weak fields, and a paramagnetic phase in strong fields. These phases are separated by a second-order phase transition (red line), except at the multicritical point $(h_z, h_x) = (1, 0)$, where the absence of quantum fluctuations produces a classical first-order transition. The region accessible in the experiment is highlighted in blue. b, Here the Hamiltonian may be decomposed into a constraint term (shaded red) that prevents adjacent 'down'-spins, and field terms (shaded blue) that drive the phase transition [19].

As shown in Fig. 3 the tilt value change allows to switch from paramagnetic phase (a) to antiferromagnetic (c), whereas the exact spin mapping to bosonic atoms in a tilted potential well is presented in (d).

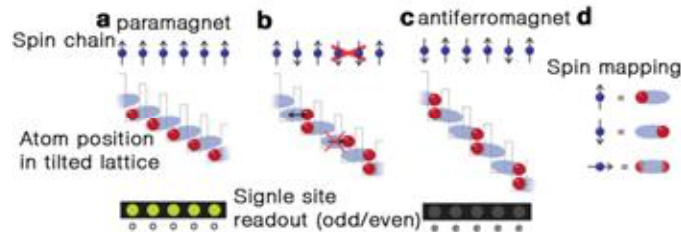


Fig. 3. Tilted Hubbard model and mapping to spin model. Consider first the middle row. a, When a Mott insulator is tilted by \mathbf{E} per lattice site, it maintains unity occupancy until \mathbf{E} reaches the on-site interaction energy \mathbf{U} . b, As the energy cost to tunnel, $\Delta = \mathbf{E} - \mathbf{U}$, vanishes, an atom can tunnel to the neighbouring site if the atom on that site has not itself tunneled. Otherwise, the tilt \mathbf{E} inhibits tunnelling, producing a strong constraint. c, Tilting further, the system undergoes a transition into a doubly degenerate staggered phase. d, Here we show how this system maps onto interacting spin-1/2 particles, whose two spin states correspond to the two possible locations of each atom. The tunnelling constraint forbids adjacent down spins, realizing a spin-spin interaction. Top row: the initial Mott insulator corresponds to a paramagnet (a), the state at resonant tilt to an entangled (critical) spin configuration (b), and staggered ordering at large tilt to an antiferromagnet (c). Bottom row: parity-sensitive site-resolved imaging results in bright paramagnetic (a; o, odd), and dark antiferromagnetic (c; e, even) domains [19].

VI. FERMIONIC TRANSPORT

In addition to the above-described properties of the phase transition from the Mott insulator phase with antiferromagnetic ordering to the superconducting phase, it is very important to study the transport properties in high-temperature superconductors. Since one of the main features of superconducting materials is their unusual electronic transport properties, i.e. the ability to have zero resistivity and conduct an electronic current with no voltage applied and no significant losses, the quantum simulation of the electronic transport is also relevant.

To study the influence of interactions on fermionic cloud expansion in a square lattice [22], Schneider et al. focused on fermionic transport and out-of-equilibrium dynamics of a homogeneous Hubbard model. For this purpose, the authors of [22] employed ultracold fermionic potassium atoms loaded into a blue-detuned optical lattice with an additionally imposed red-detuned dipole-trap. Different hold times in a deep lattice allowed to block tunneling between adjacent sites and control dephasing, where the dipole-trap potential allowed to prepare an initial confined density profile of a fermionic cloud for the following expansion.

In a non-interacting case, the expansion dynamics profile is shown in Fig. 4 for three expansion times. The initial rotationally symmetry (1 ms) gets broken (10 ms) and the cloud takes the square form (20 ms). In the non-interacting regime, the dynamics is governed by the hopping term in the Hubbard model only, i.e. by a ballistic expansion, that finally leads to the square-like symmetry of the cloud similar to the first Brillouin zone symmetry.

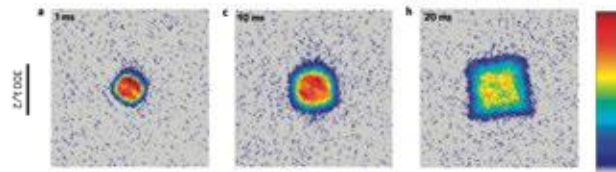


Fig. 4. Expansion of non-interacting fermions. Expansion times: a – 1 ms, b – 10 ms, c – 20 ms. In situ absorption images (column density in a.u.) of an expanding non-interacting cloud in a horizontally homogeneous square lattice with lattice depth $8E_F$ ($1 \text{ ms} \approx 1.8\hbar/J$). The expansion changes the symmetry of the cloud from the rotational symmetry of the harmonic trap to the square symmetry of the lattice Brillouin zone [22].

Within the preparation process, the effective interaction term was controlled using a Feshbach resonance [23], [24]. Since the effective spins of fermionic potassium atoms in the lattice were simulated with the two lowest hyperfine states, Feshbach resonances allowed changing effective scattering length for the atoms in the lattice via tuning of a magnetic field, thus letting the control of their interaction. The Feshbach resonance allowed to study the effect of interaction on the expanding fermionic cloud as well, as shown in Fig. 5.

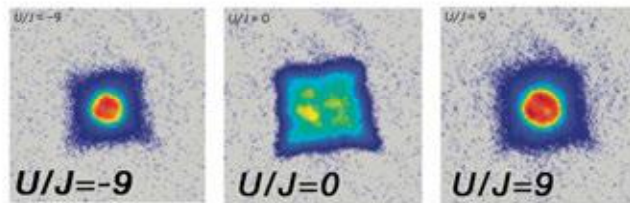


Fig. 5. Expansion of interacting fermions. Experimental in situ absorption images for different interactions after 25 ms expansion in a horizontally homogeneous lattice. The images show a symmetric crossover from $U/J = 0$, a ballistic expansion for non-interacting clouds, to an interaction-dominated expansion for both attractive ($U/J = -9$) and repulsive ($U/J = +9$) interactions. Images are averaged over at least five shots and all scales are identical to those in Fig. 3 [22].

The fermionic cloud separates into two fractions: ballistic background and diffusive core. Surprisingly, the density profiles and expansion rates are similar for attractive ($U/J = -9$) and repulsive ($U/J = 9$) interactions, where U controls interaction between atoms. This symmetry is a direct consequence of internal time-reversal symmetry of the Hubbard model.

The method developed in the study [22] for quantum simulation of fermionic transport with ultracold potassium atoms in an optical lattice is simple, but prospective for future studies. Transport properties are always hard to predict and calculate even in rather simple systems. Moreover, in the presence of strong correlations in a system, as, for example, in high-temperature superconductors, there is no way to study transport directly. Hence, new advanced quantum simulators of transport like this one would substantially reduce complexity of prediction of new high-temperature superconductors.

VII. CONCLUSIONS

Quantum simulation seems to be a promising technique to cope with the physical problems related to high-temperature superconductivity. In the present review one of the most developed quantum simulator types, ultracold atoms in optical lattices, and its application to the solving of condensed-matter physics problems were considered. Some examples of quantum many-particle strongly interacting systems were presented in reasonable detail. Three recently developed quantum simulators on ultracold atoms in optical lattices for the physical problems related to high-temperature superconductivity were considered. Their applications comprise the following quantum problems: a quantum transition from the Mott insulator phase to the superfluid phase, a quantum transition from antiferromagnetic to paramagnetic ordering with an external magnetic field applied, and investigation of fermion transport properties for non-interacting and interacting atomic clouds. Further development of the experimental techniques would lead to the creation of new quantum simulators, which would allow to get a deeper insight into the problem of high-temperature superconductivity and the theoretical concepts behind it.

VIII. ACKNOWLEDGMENT

The author is grateful to Boris Fine for many a fruitful discussion on possible origins and modern theories of high-temperature superconductivity.

IX. REFERENCES

- [1] J. G. Bednorz and K. A. Müller, "Possible high T_c superconductivity in the Ba—La—Cu—O system," in *Ten Years of Superconductivity: 1980--1990*, Springer, 1986, pp. 267–271.
- [2] A. Schilling, M. Cantoni, J. D. Guo, and H. R. Ott, "Superconductivity above 130 K in the Hg-Ba-Ca-Cu-O system," *Nature*, vol. 363, no. 6424, pp. 56–58, 1993.
- [3] A. P. Drozdov, M. I. Erements, I. A. Troyan, V. Ksenofontov, and S. I. Shylin, "Conventional superconductivity at 203 kelvin at high pressures in the sulfur hydride system," *Nature*, vol. 525, no. 7567, pp. 73–76, 2015.
- [4] S. Nishijima, S. Eckroad, A. Marian, K. Choi, W. S. Kim, M. Terai, Z. Deng, J. Zheng, J. Wang, K. Umemoto, and others, "Superconductivity and the environment: A roadmap," *Supercond. Sci. Technol.*, vol. 26, no. 11, p. 113001, 2013.
- [5] J. Bardeen, L. N. Cooper, and J. R. Schrieffer, "Theory of superconductivity," *Phys. Rev.*, vol. 108, no. 5, p. 1175, 1957.
- [6] I. Manin, *Vychislimoe i nevychislimoe*.
- [7] R. P. Feynman, "Simulating physics with computers," *Int. J. Theor. Phys.*, vol. 21, no. 6, pp. 467–488, 1982.
- [8] D. Deutsch, "Quantum theory, the Church-Turing principle and the universal quantum computer," in *Proceedings of the Royal Society of London A: Mathematical, Physical and Engineering Sciences*, 1985, vol. 400, no. 1818, pp. 97–117.
- [9] I. Buluta, F. Nori, and D. Q. Simulators, "REVIEW Quantum Simulators," *Science* [80-.], no. 1.
- [10] J. I. Cirac and P. Zoller, "Goals and opportunities in quantum simulation," *Nat. Phys.*, vol. 8, no. 4, pp. 264–266, 2012.
- [11] I. M. Georgescu, S. Ashhab, and F. Nori, "Quantum simulation," *Rev. Mod. Phys.*, vol. 86, no. 1, pp. 153–185, 2014.
- [12] A. J. Leggett, "Bose-Einstein condensation in the alkali gases: Some fundamental concepts," *Rev. Mod. Phys.*, vol. 73, no. 2, p. 307, 2001.
- [13] I. Bloch, "Ultracold quantum gases in optical lattices," *Nat. Phys.*, vol. 1, no. 1, pp. 23–30, 2005.
- [14] O. Morsch and M. Oberthaler, "Dynamics of Bose-Einstein condensates in optical lattices," *Rev. Mod. Phys.*, vol. 78, no. 1, p. 179, 2006.
- [15] I. Bloch, J. Dalibard, and W. Zwerger, "Many-body physics with ultracold gases," *Rev. Mod. Phys.*, vol. 80, no. 3, p. 885, 2008.
- [16] I. Bloch, J. Dalibard, and S. Nascimbène, "Quantum simulations with ultracold quantum gases," *Nat. Phys.*, vol. 8, no. 4, pp. 267–276, 2012.
- [17] P. A. Lee, N. Nagaosa, and X. G. Wen, "Doping a Mott insulator: Physics of high-temperature superconductivity," *Rev. Mod. Phys.*, vol. 78, no. 1, 2006.
- [18] M. Greiner, O. Mandel, T. Esslinger, T. W. Hänsch, and I. Bloch, "Quantum phase transition from a superfluid to a Mott insulator in a gas of ultracold atoms," *Nature*, vol. 415, no. 6867, pp. 39–44, 2002.
- [19] J. Simon, W. S. Bakr, R. Ma, M. E. Tai, P. M. Preiss, and M. Greiner, "Quantum simulation of antiferromagnetic spin chains in an optical lattice," *Nature*, vol. 472, no. 7343, pp. 307–12, 2011.
- [20] M. A. Novotny and D. P. Landau, "Zero temperature phase diagram for the $d=1$ quantum Ising antiferromagnet," *J. Magn. Magn. Mater.*, vol. 54, pp. 685–686, 1986.
- [21] A. A. Ovchinnikov, D. V. Dmitriev, V. Y. Krivnov, and V. O. Chervanovskii, "Antiferromagnetic Ising chain in a mixed transverse and longitudinal magnetic field," *Phys. Rev. B*, vol. 68, no. 21, p. 214406, 2003.
- [22] U. Schneider, L. Hackermüller, J. P. Ronzheimer, S. Will, S. Braun, T. Best, I. Bloch, E. Demler, S. Mandt, D. Rasch, and A. Rosch, "Fermionic transport and out-of-equilibrium dynamics in a homogeneous Hubbard model with ultracold atoms," *Nat. Phys.*, vol. 8, no. 3, pp. 213–218, 2012.
- [23] H. Feshbach, "Unified theory of nuclear reactions," *Ann. Phys. (N. Y.)*, vol. 5, no. 4, pp. 357–390, 1958.
- [24] C. Chin, R. Grimm, P. Julienne, and E. Tiesinga, "Feshbach resonances in ultracold gases," *Rev. Mod. Phys.*, vol. 82, no. 2, pp. 1225–1286, 2010.

FOCUS

$\frac{2(n-m)^2}{m^2n^2} \cdot \frac{2(n-m)^2}{m^2n^2} \cdot \frac{m^2n^2}{mn} = mn \cdot 4 = \frac{4mn}{m^2n^2}$

$16(x-2)^2 - 9(y-3)^2 = 144 \Rightarrow \frac{(x-2)^2}{9} - \frac{(y-3)^2}{16} = 1 \quad e = \frac{c}{a}$

5) $\frac{2(n-m)^2}{m^2n^2} \cdot \frac{(m-n)^2}{2mn} \cdot \frac{54}{-18} = \frac{2(n-m)^2}{m^2n^2} \cdot \frac{(m-n)(m+n)}{2mn} \quad \begin{matrix} c=3 \\ a=2 \end{matrix}$

$\begin{cases} 5 = -k \cdot 5 + b \\ 1 = k \cdot 3 + b \end{cases} \Leftrightarrow \begin{cases} 5 = -5k + b \\ 1 = 3k + b \end{cases}$

$\begin{cases} -5k + b = 5 \\ 3k + b = 1 \end{cases}$

$\bar{n} = \{-4, 11, -3\}$

$B(3, 1) \quad \frac{3}{2} = 1,5; \quad \begin{cases} c=2 \\ a=2 \end{cases}$

$A(-5, 5)$

$D(2, 5)$

$AD \perp CB$

$d = \sqrt{(x_2 - x_1)^2 + (y_2 - y_1)^2}$

$e > 1$

$x - 54y - 161 = 0$

$\frac{(m-n)^2}{2mn}; \quad 2/2 = 1$

$161 = 0$

$e = \frac{c}{a}$

$e = \frac{6}{3} = 2$

$\frac{m^2n^2}{m^2n^2} = 1 \cdot 2(n^2 + m^2) = \frac{2(n^2 + m^2)}{m^2n^2}$

$16x^2 - 64x - 161 = 0; \quad c = \frac{b^2}{4a} - 9y^2 - 54y - 161 = 0;$

$x^2 - 9y^2 - 64x - 54y - 161 = 0$

$\frac{x-x_1}{m} = \frac{y-y_1}{n} = \frac{z-z_1}{p}$

$16(x + \frac{64}{32})^2 = 16(x-2)^2$

$\frac{(m-n)(m+n)}{2mn}$

$(\bar{F} = (m, n, p)) \quad \frac{4}{1} \cdot \frac{1}{mn} = \frac{4}{mn}; \quad \frac{2(n-m)^2}{m^2n^2}$

Analysis of Interdependencies between Gas and Electric Power Systems for Optimal Dispatching and Reliability Assessment

A. Churkin*

Abstract - This paper analyzes existing studies of gas and electricity systems interconnections. The number of such studies has significantly increased over the last decade due to expansion of both electric power and gas systems and widespread use of gas-fired power plants. However, examination of gas/electricity correlations appears to be a rather complex task with various possible solutions. Some studies examine typical schemes with a moderate number of nodes and analyze optimal dispatching and gas pressure control. Others perform global optimization on a scale of a certain country or even interstate power exchange. Although each study has its own particular goal, the basic principles of the systems interconnections remain the same. The main techniques and approaches to modeling of gas/electricity interdependencies are reviewed in this paper. Proposals for future research are also made.

Index Terms - gas network, electric network, optimal power flow, optimal dispatching, interconnection of systems.

I. INTRODUCTION

Continuous increase of power demand leads to expansion of both electric power and gas systems. Simultaneously, economic and environmental factors encourage usage of gas-fired power plants. Hence, interdependencies between gas and power systems become more obvious. Numerous studies performed in the last decade have shown complexity and multifacetedness of modeling interdependencies.

Most of the existing studies have been performed in the developed countries with wide and complex gas and power systems (UK, Switzerland, US). Such studies [1–3] are focused on problems of global dispatching and optimization on a country scale. Main results of the studies show possible reduction in systems operation cost and possible benefits for social welfare.

Another important problem that appears when the two systems are considered together is reliability assessment. In [4] contingency analysis is performed in order to estimate an impact on electric power system and ensure global security. Considering gas system security constraints and gas pressure maintenance, several coordination scenarios among gas and power systems are suggested in [5].

The coupling of gas/electricity concept called “energy hub” is presented in [6–8]. Different power flows are considered interconnected in “hubs” in order to get operational and economic benefits. The concept decomposes optimal power flow problem into subproblems that could be effectively solved for each “hub”.

Gas and electricity interdependencies have also been studied on the interstate scale. Model suggested in [9]

A. I. Churkin is with the Center for Energy Systems, Skolkovo Institute of Science and Technology, Skolkovo Innovation Center, Building 3, Moscow 143026, Russia (e-mail: andrey.churkin@skolkovotech.ru).

performs cross-border energy trade optimization for the European Union countries.

Rather innovative methodology described in [10] estimates operational impact of Power-to-Gas (P2G) technology on electrical and gas transmission networks. This technology enables to convert excessive electric energy into synthetic gas that could be stored in gas transmission network. P2G technology can be considered as inverse coupling of the two systems that extend dispatching and optimization horizons.

Finally, the possibility of demand-side response in combined gas and electricity networks is studied in [11]. It can enhance power system flexibility and reduce investments in further systems development.

Although each study is focused on a particular problem that exists at the confluence of the two systems, the basic principles of the systems interconnections remain the same. This article analyzes basic principles of modeling gas/electricity interdependencies and suggests direction for further research. In section II, the main concept of gas and electricity systems interconnection is presented as well as possible ways of global optimization. Section III provides methodology for gas and electricity systems modeling. Section IV summarizes the main points of the paper.

II. BASIC CONCEPT

Despite different goals of modeling mentioned above the basic principle of modeling gas/electricity interdependencies can be inferred: gas-fired power plants are considered as the main linkage between the two systems (fig. 1). For example, in order to produce a certain amount of electric energy, a generator must consume a certain volume of gas. Gas compressor can also be considered as an interconnection point since it consumes electric energy in order to maintain gas pressure. Together with P2G technology, gas compressors form inverse coupling of the two systems. However, such inverse coupling can be neglected in comparison to the power produced by gas-fired generators.

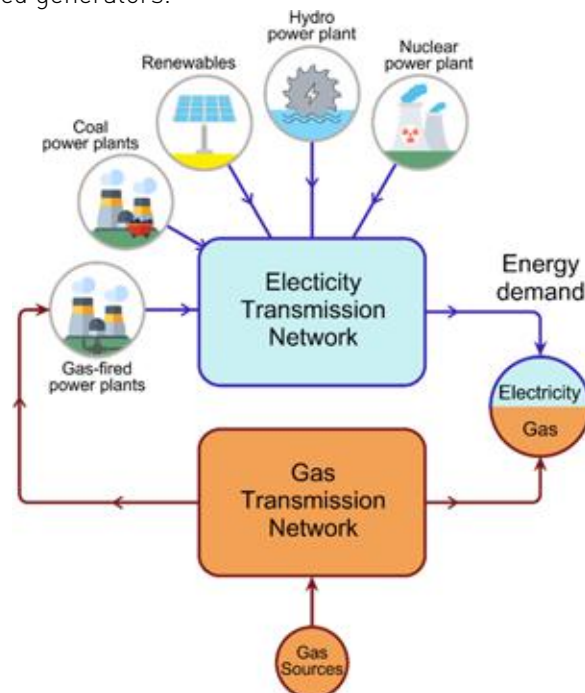


Fig. 1. Gas-fired power plants as main interconnection points between gas and electric power networks

Thus, power can be transmitted to users in two ways: through electricity transmission network or mostly by gas transmission network (in form of gas) with further conversion into electricity. Both gas and power networks have been well studied individually. It is well known how to perform optimal power flow optimization for power

systems as well as gas flow optimization and compressors scheduling [5]. The question arises, what economic benefits can be obtained in case of global optimization and dispatching (gas + power optimal flow). Solution to this problem becomes a sophisticated mathematical and engineering task since we complicate an objective function, add more restrictions and variables (generators output capacity and power of gas compressors).

Before approaching this task, the main modeling methodologies for gas and power systems modeling should be analyzed. The review of existing methodologies is presented in the next section.

III. MODELING METHODOLOGY

A. Power network modeling

There limited options regarding modeling methodology for power network. Most of the listed studies [2, 3, 5, 9] successfully use direct current (DC) approximation for electric power system states modeling. DC power flow formulation enables the calculation of power flows in each particular transmission line in case when there is a lack of precise data about existing power networks.

Modeling formulations are rather obvious and require Kirchoff's laws implementation, and constraints satisfaction.

Total system power constraint:

$$\sum_{\nu} (p_i(t) - h_i(t)) = 0 \quad (1)$$

where $p_i(t)$ is production profile of generator i ; $h_i(t)$ is consumption profile of load i ; ν – total number of nodes. Generator production limit:

$$p_i^{\min} \leq p_i(t) \leq p_i^{\max} \quad (2)$$

Power flow limits:

$$-f_{ij}^{\max} \leq M_{ij}(p(t) - h(t)) \leq f_{ij}^{\max} \quad (3)$$

where f_{ij}^{\max} is power flow limit of a certain transmission line; matrix M represents correspondence between line power flows and power injections at nodes.

Thus, power network modeling is usually performed for steady-state conditions within a single time-step (taken as 1 hour). In order to model system behavior for the period of one day, $T = 24$ power states have to be calculated. If gas system modeling is performed dynamically, values for power system must be converted to continuous values also. This can be done as following integration:

$$\min J_p = \sum_{i \in \nu} \int_0^T [c_i \cdot p_i(t) + c_k \cdot \Delta p_k(t)] dt \quad (4)$$

where J_p is an objective function that minimizes total cost of generation and cost of power losses; c_i represents cost functions of production; c_k represents cost of power losses $\Delta p_k(t)$ in transmission lines.

B. Gas network modeling

Gas network modeling is not as clear as power network modeling. The main challenge is physics of gas flow. Gas flows much slower than electricity. This means that gas dynamics cannot be easily neglected. There are some approaches of steady-state gas network modeling, but they are rather rough and inaccurate. Hence, existing studies are divided into gas steady-state modeling approaches and dynamic modeling approaches. Moreover, each study suggests its own gas flow equations and objective function representations. Such variety of methods makes it

extremely hard to find the best optimization solution for the gas and power systems coupling.

Another difficulty of gas network modeling is presentation of such gas equipment as compressors and gas storages. These two essential components of gas network can also be modeled in different ways. Gas compressors can be presented as a function that changes pressure at a node where it is installed. Gas storages can be presented as gas injections into network.

Thus, there are different approaches and equations for modeling gas flows in gas pipelines, gas compressors and storages. We will focus only on the meaning of the equations, not describing numerous physical formulas. More detailed information about the modeling can be found in [1, 2, 3, 5].

Each gas flow (φ_{ij}) can be represented as function dependent on pressure difference ($\rho_i - \rho_j$) between ends of a pipeline or as a system of differential equations that involves gas pressure (ρ), friction factor (λ) and many other parameters.

$$\varphi_{ij} = f((\rho_i - \rho_j), \lambda, \dots) \quad (5)$$

Gas modeling constraints include nodal balance condition (6), gas pressure values constraints (7), power of compressor (CP_i) constraint (8), compressor ratio (θ_i) constraint (9), withdrawal from gas storage constraint (10) and gas pipeline limits (11).

$$\sum_{i \in N} \varphi_{ij} + \sum_{i \in N} I_i - \sum_{i \in N} d_i = 0 \quad (6)$$

where I_i is gas injection to a certain node i ; d_i stands for gas demand at a node; N – total number of nodes in gas network.

$$\rho_i^{\min} \leq \rho_i(t) \leq \rho_i^{\max} \quad (7)$$

$$CP_i \leq CP_i^{\max} \quad (8)$$

$$\theta_i^{\min} \leq \theta_i \leq \theta_i^{\max} \quad (9)$$

$$I_i \leq I_i^{\max} \quad (10)$$

$$\varphi_{ij}^{\min} \leq \varphi_{ij}(t) \leq \varphi_{ij}^{\max} \quad (11)$$

C. Gas and electricity optimal power flow

Global optimization involves objective functions and restrictions of both gas and electric power systems. One of the possible optimization problems can be stated as total operation cost minimization. This means reduction of power losses along with low cost power generation and optimal scheduling of compressors. An objective function for this case will be:

$$J_{pg} = \int_0^T \left[\sum_{i \in V} \{c_i \cdot p_i(t) + c_k \cdot \Delta p_k(t)\} + \sum_{i \in N} c_e \cdot CP_i(t) \right] dt \quad (12)$$

where c_e represents cost of compressors operation.

Thus, the minimization problem is:

$$\begin{aligned} & \min_{p_i(t), \theta_i} J_{pg} \\ \text{subject to:} & \text{ power system constraints (1-3)} \\ & \text{ gas system constraints (6-11)} \end{aligned} \quad (13)$$

Result of the optimization will show the new optimal regimes of gas and power systems that will be the most beneficial for society. Applying of gas flow differential equations will also enable gas pressure control over time [5].

IV. CONCLUSION

Analysis of interdependencies between gas and electric power systems extends boundaries of optimal operation and dispatching and poses new complex problems that can be treated in several ways. On the one hand, objective function can be aimed at security maintenance or reduction of operation cost, while on the other hand, there is a variety of modeling methodologies that can be implemented.

However, in spite of scientific novelty, practical application of the research in the direction of gas and power systems coupling is rather obscure. The main obstacle is that application of global dispatching and optimization needs significant technical and regulatory development. Therefore, in order to attract attention of government and transmission system operator, a real case should be studied and optimized. It will show what benefits could be obtained. Furthermore, it is not clear yet how these benefits should be shared among all participants of the optimization (system operator, power grid company, generating companies and gas companies). Each participant has to be motivated to contribute to the optimization.

Global reliability assessment can also be performed for the coupled systems. Since each particular gas-fired power plant has an emergency fuel reserve (oil), only serious long-term incidents should be considered in contingency analysis. The mentioned pressure maintenance methodologies should be also verified for real systems.

In summary, existing approaches of the coupled modeling and optimization have to be verified for real cases. First of all, values of total benefits should be calculated and announced in order to attract industry partners and attention of the government. Then, distribution of total benefits should be suggested.

Further work will be focused on a real case examination.

V. REFERENCES

- [1] S. An, Q. Li, T.W. Gedra, "Natural gas and electricity optimal power flow," Transmission and Distribution Conference and Exposition, 2003 IEEE Power Engineering Society, vol. 1, 7-12 pp. 138-143, 2003.
- [2] C. Unisihuyay, J.W. M. Lima, and A.C.Z. de Souza, "Modeling the Integrated Natural Gas and Electricity Optimal Power Flow," IEEE Power Engineering Society General Meeting, Tampa, Florida, June 24-28, 2007.
- [3] M. Chaudry, N. Jenkins, G. Strbac "Multi-time period combined gas and electricity network optimization," Elec. Power Syst. Research, Vol. 78, No.7, pp. 1265-1279, 2008.
- [4] Shahidehpour, M., Fu, Y., Wiedman, T., "Impact of natural gas infrastructure on electric power systems," Proceeding of the IEEE 93 (5): 1042-1056, 2005.
- [5] A. Zlotnik, L. Roald, S. Backhaus, M. Chertkov, G. Andersson, "Coordinated Scheduling for Interdependent Electric Power and Natural Gas Infrastructures," IEEE Transactions on Power Systems, vol. 32, no. 1, pp. 600-610, Jan. 2017.
- [6] M. Arnold, G. Andersson, "Decomposed electricity and natural gas optimal power flow, " presented at the 16th Power Systems Computation Conference (PSCC 08), Glasgow, Scotland, 2008.
- [7] M. Geild, G. Andersson, "Optimal power flow of multiple energy carriers," IEEE Transactions on power systems 22 (1), pp. 145-155, 2007.
- [8] A. Hajimiragha, C. Canizares, M. Fowler, M. Geidl, G. Andersson "Optimal energy flow of integrated energy systems with hydrogen economy considerations," Proceedings of Bulk Power System Dynamics and Control - VII, Charleston, SC, USA, Aug. 2007.
- [9] C. Spataru, J. W. Bialek, "Energy Networks: a Modelling Framework for European Optimal Cross-Border Trades," PES General Meeting | Conference & Exposition, 2014 IEEE, Oct. 2014.
- [10] S. Clegg and P. Mancarella, "Integrated Modeling and Assessment of the Operational Impact of Power-to-Gas (P2G) on Electrical and Gas Transmission Networks," IEEE transactions on sustainable energy, vol. 6, no. 4, pp. 1234-1244, October 2015.
- [11] M. Qadrdan, M. Cheng, J. Wu, N. Jenkins, "Benefits of demand-side response in combined gas and electricity networks," Applied Energy 192 , pp. 360-369, 2016.

Modern Trends in European District Heating

Maksim D. Glagolev

Abstract - This paper overviews the modern trends of District Heating (DH) development in European countries. Energy systems are facing the challenge of being more efficient and carbon free. Some countries have accepted the challenge, however some countries are still idling. European Union is one of the most active players in the development of DH systems thus their experience and competences are very valuable. Countries like Russia, where DH plays a life-sustaining role, can utilize this great experience and motivation to boost the efficiency and sustainability of the energy systems.

Index Terms - Combined heat and power, district heating, energy efficiency, heat pump, integrated energy infrastructures, low temperature district heating, renewable energy sources, thermal energy storage.

I. INTRODUCTION

District Heating (DH) is a very important part of energy systems all over the world. Power systems are traditionally associated with the most significant life-sustaining technology, however the understanding of role, which DH plays in energy systems operation and development is increasing year in, year out. Present energy systems are facing the challenges to be as efficient, sustainable and carbon free as possible [12]. District heating systems, in turn, are able to increase the efficiency of energy sector and thus play a significant role in meeting the challenges [13].

The DH of the future must be designed for the new energy systems but not for the present ones. Existing DH will probably have to be redesigned or renovated to be able to operate as a part of integrated energy infrastructure where electricity sector will be joined with DH sector, gas sector as well as transport [14].

DH systems have been developing in different ways from country to country and this diversity opens the door to experience exchange and multinational collaboration, which will help to meet the challenges of the future. Not all countries have accepted the challenge yet. European countries are very active in DH development. European research groups supported by European Commission are working jointly with industries and governments to develop the Smart District Heating systems in cities and neighborhoods. The modern trends and directions of research are valuable to analyze and study since their experience and findings could be implemented in other countries.

Russia, where DH systems play a life-sustaining role, still did not accept the challenge. European experience can be extremely motivating and helpful to build a new generation of the Russian DH systems..

II. EUROPEAN POLICIES AND DISTRICT HEATING PROJECTS

The present EU policies regarding the District Heating have the goal to push the R&D activities toward development of Smart District Heating and Cooling (DHC) systems. There are nine documents issued between 2003 and 2013, which cover DH research area and stimulate the increase of energy efficiency, use of Renewable

M. D. Glagolev is with the Center of Energy Systems, Skolkovo Institute of Science and Technology, Skolkovo Innovation Center, Building 3, Moscow 143026, Russia (e-mail maksim.glagolev@skolkovotech.ru).

Energy Sources (RES), smart utilization of primary fuel, smart management and control of the systems as well as demand side management [15].

EU supports the number of research groups and projects from all over Europe. The funding is provided by the entire country or by the country and the EU. More than 40 DH projects are now running in Europe with total funding more than 270 million Euros [4]. The exact funds ranking is shown in Fig. 1.

The most significant projects are: CELSIUS, ECO-LIFE, PIME'S, and 4th Generation DH, where CELSIUS and 4DH are strategic platforms for smart DHC development; ECO-LIFE is the project for clean, carbon free energy generation and usage; and PIME'S is the smart grids project for both electrical and heat networks [16]-[19].

Although, these 40+ projects have different and multidisciplinary activities, they cover all research topics and sub-topics related to DH systems.

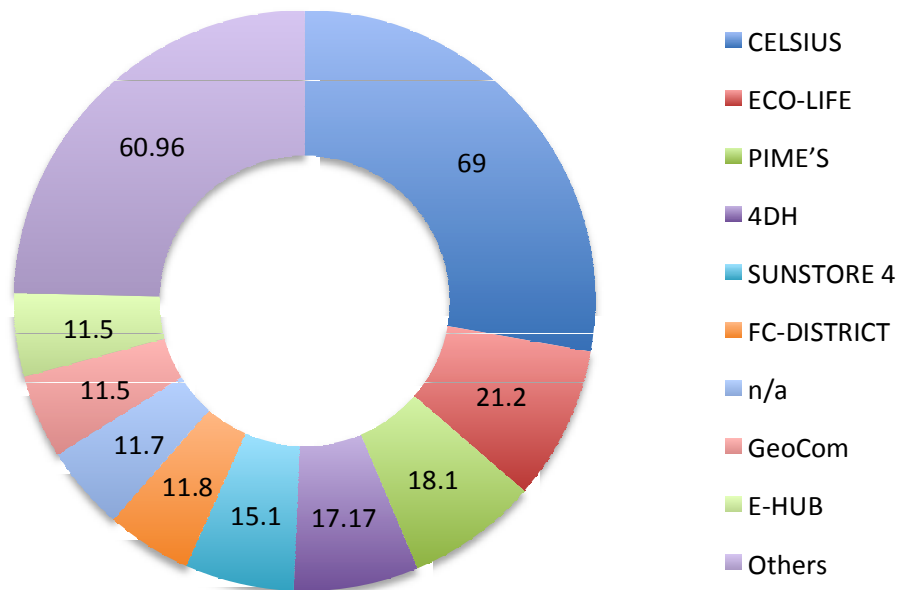


Fig. 1. EU DH projects funding, millions of euro

III. MODERN TRENDS IN DISTRICT HEATING DEVELOPMENT

District Heating research topic has a wide range of sub-topics and trends. The basic goal is to create the new generation DH systems, which will be a part of Smart energy systems. According to professor H. Lund, 'Smart energy system is an energy system in which smart electricity, thermal and gas grids are combined and coordinated to identify synergies between them in order to achieve an optimal solution for each individual sector as well as for the overall energy system' (Lund, 2014) [20]. Thus, DH needs to be smart itself. There are four main principles and technologies, which characterize the smart DH systems.

A. Low Temperature District Heating

District Heating systems are now on the threshold of new era - the 4th generation of district heating. Previous 3 generations used steam (1st generation) and hot water with supply temperature around 100°C (2nd and 3rd generation). The 4th generation DH will reduce supply temperature of hot water to the level of 50-60°C and thus reduce the heat losses in supply and return pipelines. This trend was named as Low Temperature District Heating (LTDH) [21]. Four generations of DH and its characteristics are shown in Fig. 2.

However, the reduction of heat losses is not the only advantage of LTDH. Low-temperature supply increases the opportunity to integrate RES into the systems as well as to utilize low-temperature waste heat [22]. Denmark and Sweden are the main countries, which are conducting research in this field.

B. Renewable Energy Sources, Surplus and Waste Heat

The other sub-topic of DH research area is the RES integration and usage of waste and surplus heat.

The main RES applicable to DH systems are: solar thermal energy, geothermal energy, and biomass.

Solar thermal energy plants are based on large-scale solar collectors usually coupled with Thermal Energy Storages (TES). The main zone of implementation is residential sector where the heat request is lower than in cities. Germany, Italy and Spain are the leading countries in this topic.

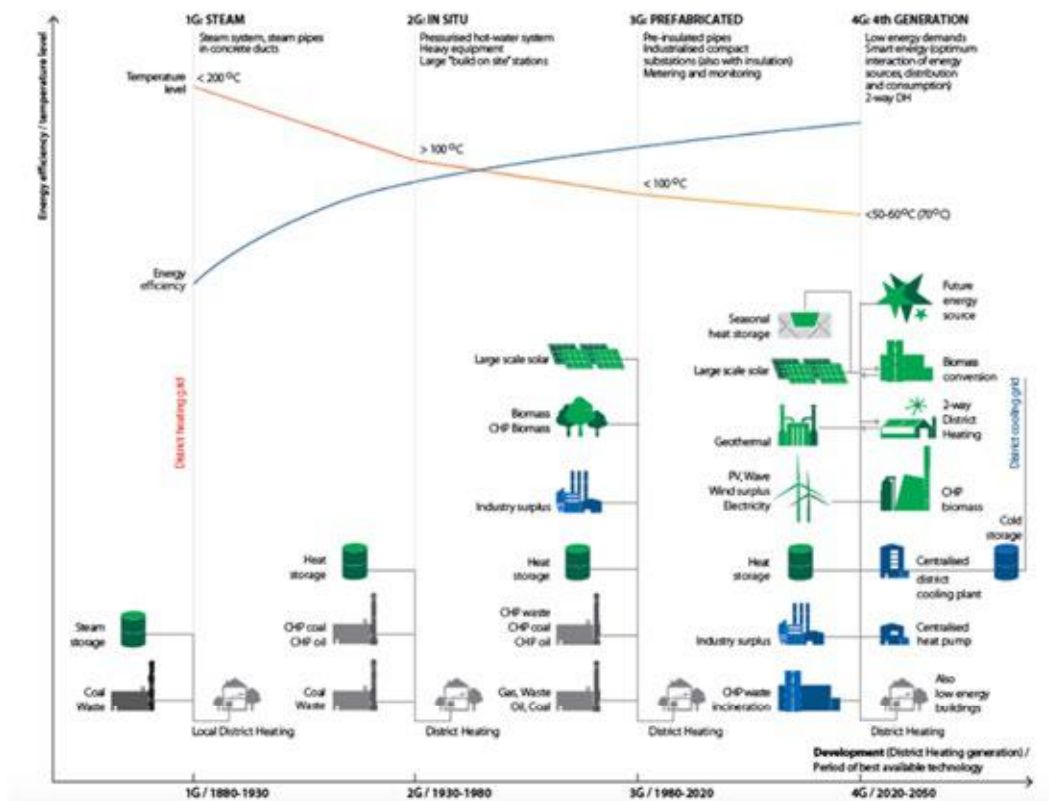


Fig. 2. Four generations of District Heating [21]

Geothermal energy is usually associated with ground source heat pumps. The technology is relatively expensive, however performance of the technology significantly increases when it is combined with RES, which produce cheap electricity, or as a part of integrated energy system.

Biomass is the most developed and widely spread RES technology in DH systems. It includes biogas used for a big number of Combined Heat and Power (CHP) plants at the residential and city levels. Austria, Germany and Denmark are the leaders in biomass development [23].

Surplus heat from CHP is the main and the most widely spread source of heat in modern DH systems, thus optimization and energy efficiency increase are the main goals for this heat source. However, the complexity of the task increases if CHP is considered as a part of integrated energy infrastructure [15].

Waste heat has a great potential to be utilized, especially in case of industrial surplus heat. A huge number of plants produce waste heat, and the goal is to take this heat and distribute it to the demand. The other objective is to utilize low-temperature waste heat, which is produced in the residential sector, office buildings, shopping

molls, etc. Thus, the use of waste heat leads to utilizing free heat energy and has a great technical and economical potential. Research in this area is in the early stage due to its complexity.

C. DH as a Part of Integrated Energy Infrastructure

Integrated Energy Infrastructure is a relatively new concept, which includes DH sector, electricity sector, as well as gas infrastructure. The idea behind is to gain synergy out of this integration, fulfill the environmental goals and increase energy efficiency, sustainability, and economical performance. The inherent components and principles such as smart meters, smart control devices, demand and supply side management must be present in each system.

The combination of these energy sectors creates energy hubs where energy is produced and distributed in the most effective way [24].

DH system as a part of Integrated Energy Infrastructure must become more flexible, smart and responsive. That is why almost all DH systems will have to include thermal energy storages (usually filled with hot water), which will balance the electrical and heat load at the CHP plants and cover the RES instability. Different scale ground-source heat pumps will be able to meet the heating request when electricity from RES is cheap. Booster heat pumps will help to fulfill the LTDH principle. And finally, demand side management will help to stabilize heat production and electricity consumption by using air in the buildings as the TES [25].

D. Renovation and Optimization of Existing DH Systems

Future energy systems will need DH systems of new generation. As the big part of DH infrastructure in Europe was built more than 20 years ago, it needs to be revitalized. Moreover, the new principles such as LTDH have very strict requirements to the DH infrastructure. The old insulation materials, pipelines, and substation technologies (e.g. heat-exchangers) have to be changed or at least optimized. The new smart meters and control devices are also needed to make systems more efficient. These tasks are difficult to solve without R&D and collaboration with industry. That is why several research groups are working close with energy companies to solve these tasks [26].

IV. CONCLUSIONS

This paper presents the modern trends in DH development based on the European case. Next generation of DH systems has to be developed and implemented. Renewable Energy Sources, which are already playing a great role in energy systems, will be an important part of integrated energy infrastructure concept, boosting the development and usage of different technologies such as heat pumps, thermal energy storages, and smart meters. New operation and control algorithms and devices will be also created to optimize the usage of primary fuel. New approaches to network design and topology have to be implemented as well.

These changes will help to gain the new level of energy efficiency and economical performance of energy systems, but what is most important - will reduce the consumption of primary fossil fuels, increase the flexibility and sustainability of the systems, and finally make energy systems carbon free.

These trends are applicable in other countries. Russia has to accept the challenge of DH development and utilize this experience in the most efficient way. Differentness of climate conditions and systems scale will not allow the use of these findings and results in Russian energy systems, but some of them can be implemented to boost the efficiency of the systems and make them operate better.

V. REFERENCES

- [12] Østergaard PA, Sperling K. (2014). "Towards sustainable energy planning and management". *Int J Sustainable Energy Plan Manage.* [online]. Available: <http://dx.doi.org/10.5278/ijsepm.2014.1.1>
- [13] Gebremedhin A. Optimal utilisation of heat demand in district heating systemda case study. *Renew Sustain Energy Rev.* 2014.
- [14] Jiang XS, Jing ZX, Li YZ, Wu QH, Tang WH. Modelling and operation optimization of an integrated energy based direct district water-heating system. *Energy.* 2014
- [15] J. Skok and K. Ute (2014, Sept). Thematic research summary: Smart district heating and cooling. European Institute for Energy Research (EIFER), EU. [Online]. Available <https://setis.ec.europa.eu/energy-research/publications/smart-district-heating-and-cooling>
- [16] I. J. Leren. (2012, Mar.). Summary published 2nd year PIMES. PIMES ltd. Rogaland, Norway. [Online]. Available: <http://www.pimes.eu/index.php/Deliverables>
- [17] R. M. Hummelshøj. (2016, Oct.). ECO-Life - sustainable zero carbon eco-town developments improving quality of life across EU. COWI A/S. Kongens Lyngby, Denmark. [Online]. Available: http://www.ecolife-project.eu/PDF/Final_Rep/Final_Publishable_Summary_Report.pdf
- [18] I. J. Leren. (2012, Mar.). Summary published 2nd year PIMES. PIMES ltd. Rogaland, Norway. [Online]. Available: <http://www.pimes.eu/index.php/Deliverables>
- [19] European Commission, Joint Research Centre, Institute for Energy and Transport. (2009, Apr). R&D Investment into the Priority Technologies of the European Strategic Energy Technology Plan (SET-Plan). JRC-IPTS, Seville. [online]. Available: ipts.jrc.ec.europa.eu/publications/pub.cfm?id=2659
- [20] Lund H. "Renewable energy systems: a smart energy systems approach to the choice and modeling of 100% renewable solutions". 2nd ed. Burlington, USA: Academic Press. 2014. ISBN: 978-0-12-410423-5.
- [21] Lund H, Werner S, Wiltshire R, Svendsen S, Thorsen JE, Hvelplund F, et al. "4th generation district heating (4GDH): integrating smart thermal grids into future sustainable energy systems". *Energy.* 2014.
- [22] Schmidt R.R., Pol O., Basciott, D. and Page J., "Smart thermal networks for smart cities – Introduction of concepts and measures", *EDP Sciences.* 2012.
- [23] Mathiesen BV, Lund H, Karlsson K. "100% Renewable energy systems, climate mitigation and economic growth". *Appl Energy.* 2011.
- [24] Connolly D, Mathiesen BV, Østergaard PA, Müller B, Nielsen S, Lund H, et al. (2013). Heat roadmap Europe: second pre-study. [online]. Available: http://vbn.aau.dk/files/77244240/Heat_Roadmap_Europe_Pre_Study_1.pdf
- [25] Østergaard PA, Andersen AN. Booster heat pumps and central heat pumps in district heating. *Appl Energy.* 2016.
- [26] Frederiksen S. Lund H. "District Heating and Cooling". 2013.